

Clemson University

TigerPrints

All Dissertations


Dissertations

8-2022

Understanding Dynamics of Polymers Under Confinement: A Molecular Dynamics and Neutron Scattering Study

Supun Samindra Kamkanam Mohottalalage
Clemson University, ksupuns@g.clemson.edu

Follow this and additional works at: https://tigerprints.clemson.edu/all_dissertations

 Part of the [Computational Chemistry Commons](#), [Materials Chemistry Commons](#), and the [Physical Chemistry Commons](#)

Recommended Citation

Kamkanam Mohottalalage, Supun Samindra, "Understanding Dynamics of Polymers Under Confinement: A Molecular Dynamics and Neutron Scattering Study" (2022). *All Dissertations*. 3121.
https://tigerprints.clemson.edu/all_dissertations/3121

This Dissertation is brought to you for free and open access by the Dissertations at TigerPrints. It has been accepted for inclusion in All Dissertations by an authorized administrator of TigerPrints. For more information, please contact kokeefe@clemson.edu.

UNDERSTANDING DYNAMICS OF POLYMERS UNDER
CONFINEMENT: A MOLECULAR DYNAMICS AND
NEUTRON SCATTERING STUDY

A Dissertation
Presented to
the Graduate School of
Clemson University

In Partial Fulfillment
of the Requirements for the Degree
Doctor of Philosophy
Chemistry

by
Supun Samindra Kamkanam Mohottalalage
August 2022

Accepted by:

Dr. Dvora Perahia, Committee Chair
Dr. Gary S. Grest
Dr. Rhett C. Smith
Dr. Steven J. Stuart
Dr. Leah B. Casabianca

ABSTRACT

The current study probes the structure, dynamics, and rheological behavior of associating polymers including ionomers in melts and solutions as well as conjugated polymers confined into nanoparticles, using molecular dynamics (MD) simulations and neutron scattering techniques. The study focuses on two families of associative polymers, ion containing macromolecules and conjugated polymers.

Polymers that consist of ionizable groups along their backbone found uses in a broad range of applications. Examples include light weight energy storage and generation systems, and biomedical applications, where the polymers act as ion exchange membranes, and actuators. The ionic groups tend to form clusters that are in the core of many of the applications. Understanding the relationship of cluster properties and the structure and dynamics of ionizable polymers is crucial to optimize current applications and develop new materials with controlled transport, mechanical stability, and desired response to external stimuli.

The first part of the study focuses on understanding the structure and dynamics of polystyrene sulfonate melts as the distribution of the ionizable groups varies with random, precise (number of carbons between ionizable groups is exact), and blocky distributions along the backbone, using atomistic MD simulations. We find that the shape and size distribution of clusters as well as the number of unique chains associated with each cluster are affected by the distribution of the ionic groups. The dynamics of the polymer and the mobility of the counterions are affected by both the number and size of the clusters as well as the number of polymer chains associated with each cluster.

Following the understanding of the effects of the clusters on polymer melts, the study proceeds to probe the effects of nonlinear elongational flow on associating polymer melts, which are processed into viable materials under elongational flows. This effort contains two components a coarse grain, and an atomistic MD studies. We find that the response of the melts to elongational flows results from the evolution of both the ionic clusters and Van der Waals domains. The coarse grain study shows that clusters break and reform continuously as the chain stretches heterogeneously in the presence of elongational flow. The atomistic study provides details regarding the effect of chain and cluster rearrangements on the response to the flow.

Following melts studies, the work probed the segmental motion of slightly sulfonated polystyrene in cyclohexane solutions using the quasi-elastic neutron scattering technique. We find constraint dynamics at larger length scales however the polymer remains mobile on smaller length scales. Adding a small amount of alcohol is enough to release the constraints within the ionic clusters and results in an increase in segmental polymer motion on all length scales.

The last part of the study focused on understanding the effects of the number of rigid luminescent polymer molecules, their chemistries and initial orientation, on the structure and dynamics of soft nanoparticles (referred to as “polydots”). We find that increasing the number of chains confined affects the internal conformation of the polymer chains where side chains substituting the polymer backbone affect the polydots’ shape and stability. Similar to a single macromolecule polydots, these NPs exhibit a glass-like dynamics with relaxation times in a range of microseconds.

DEDICATION

This work is dedicated to my loving mother, Shakila Ranasinghe, for raising me to be the person I am today and for being there for me through my ups and downs, and to my sister Dilsha Nawanjanie for the tremendous support. To my wonderful wife, Sachindra Kiridena, for the unconditional love, understanding, and encouragement given to me all these years. This work would have not been possible without all of your support.

ACKNOWLEDGMENTS

I offer my sincere and deepest gratitude to Dr. Dvora Perahia and Dr. Gary S. Grest for the immense and valuable guidance and encouragement given to me during my graduate studies. I would also like to extend my gratitude to my committee members; Dr. Leah B Casabianca, Dr. Steven J. Stuart, and Dr. Rhett Smith for their valuable suggestions and time.

I would like to acknowledge Dr. Thomas O'Connor from Carnegie Mellon University, Dr. Naresh Osti and Dr. Lilin He from Oak Ridge National Laboratory for their invaluable support and technical help.

I am thankful to all my former and present group members Dr. Umesh M. Shrestha, Dr. Sabina Maskey, Dr. Dipak Aryal, Dr. Sidath Wijesinghe, Dr. Manjula Senanayake, Anuradhi Wickramshinghe, Chathurika Kosgallana, Shalika Meedin, Rosita Sivaraj, John Bracewell, Jailyn Johnson and Amod Madurapperumage for their tremendous support, encouragement, and scientific discussions.

Finally, I would like to acknowledge Department of Energy, National Science Foundation and Chemistry Department, Clemson University for financial support, Palmetto Cluster, Clemson University, National Energy Research Scientific Computing Center, Summit, at Oak Ridge National Laboratory for computational time. DOE Center for Integrated Nanotechnologies (CINT) at Sandia National Laboratories is acknowledged for training opportunities.

TABLE OF CONTENTS

ABSTRACT.....	i
DEDICATION.....	iv
ACKNOWLEDGMENTS	v
TABLE OF CONTENTS.....	vi
LIST OF TABLES.....	xv
I. INTRODUCTION	1
1.1 Ionizable Polymers.....	1
1.2 Association of Ionomers	3
1.3 Impact of Ionic Clusters.....	4
1.4 Polymers in Solutions	5
1.5 References.....	8
II. METHODOLOGY	15
2.1 Molecular Dynamics Simulations.....	15
2.2 Coarse Grained Model and Methodology.....	20
2.3 Fundamentals of Scattering.....	21
2.4 References.....	30
III. EFFECTS OF IONIC GROUP DISTRIBUTION ON THE STRUCTURE AND DYNAMICS OF AMORPHOUS POLYMERS MELTS.....	34
3.1 Abstract.....	34
3.2 Introduction.....	35
3.3 Model and Simulation Methods.....	38
3.4 Results.....	40
3.5 Conclusions.....	49
3.6 Acknowledgements.....	51
3.7 References.....	51
IV. NONLINEAR ELONGATION FLOWS IN ASSOCIATING POLYMER MELTS: FROM HOMOGENEOUS TO HETEROGENEOUS FLOW ..	57
4.1 Abstract.....	57
4.2 Introduction.....	58
4.3 Model and Simulation Methods.....	62
4.4 Results.....	65
4.5 Conclusions.....	71
4.6 Acknowledgements.....	72
4.7 References.....	72

v. RESPONSE OF SULFONATED POLYSTYRENE MELTS TO NONLINEAR ELONGATION FLOWS.....	79
5.1 Abstract.....	79
5.2 Introduction.....	79
5.3 Model and simulation methods.....	82
5.4 Results.....	84
5.5 Conclusions.....	90
5.6 Acknowledgments.....	91
5.7 References.....	91
vi. MOLECULAR INSIGHT INTO DYNAMICS OF SPARSE IONOMER NETWORKS	98
6.1 Abstract.....	98
6.2 Introduction.....	98
6.3 Materials and Methods.....	100
6.4 Results and discussion	103
6.5 Conclusions.....	111
6.6 Acknowledgments.....	111
6.7 References.....	112
vii. MULTI-CHAIN POLYMER NANOPARTICLES: MOLECULAR DYNAMICS SIMULATION STUDIES.....	119
7.1 Abstract.....	119
7.2 Introduction.....	120
7.3 Model and Simulation Methods.....	122
7.4 Results.....	124
7.5 Conclusions.....	134
7.6 References.....	135
viii. SUMMARY.....	141

LIST OF FIGURES

Figure 1.1: Chemical structure of sulfonated polystyrene sodium salt.....	2
Figure 1.2: Visualization of a cluster of SO_3^- groups [S (yellow), O (red), and Na (blue)] for PSS melts with a sulfonation fraction $f = 0.10$ and associated polymers chains. ³⁰	3
Figure 1.3: Schematics of a flexible polymer chain in good, theta and poor solvents. green: good solvent molecules, orange: theta solvent molecules, blue: poor solvent molecules, black: monomers in polymer chain.....	5
Figure 1.4: Flory-Huggins lattice model for a polymer (black) in a solvent (blue).	6
Figure 2.1: A basic MD simulation flow chart used in this work.....	17
Figure 2.2: Types of bonded interactions.	18
Figure 2.3: Schematics of Lennard-Jones potential.....	19
Figure 2.4: Vector diagram of elastic neutron scattering.....	23
Figure 2.5: Schematic representation for neutron interaction with a given sample. Ω is the solid angle and θ is the scattering angle. ^{20, 24}	24
Figure 2.6: Schematic diagram for elastic, quasi-elastic, and inelastic peaks in QENS spectrum.....	28
Figure 2.7: The Fourier transform relationship between $S(q, \omega)$, $S(q, t)$ and $g(r, t)$. ^{23, 24}	29
Figure 3.1: Visualization of SO_3^- groups in melts of random (R), precise (P), and block (B) PSS for $f = 0.10$ at 600 K after 1000 ns. Clusters in each system are colored based on number of SO_3^- groups associated (red< orange< yellow<green<teal <blue). For clarity,	

1/8 of the systems are shown. Black circled cluster represent the average cluster of SO_3^- groups for each system..... 40

Figure 3.2: Number of clusters N_{nc} , normalized to total number of chains N , as a function of cluster size N_c (number of sulfur atoms), for random (●), precise (■), and block (▲) PSS melts. Inset shows the snapshots of cluster of SO_3^- groups (enlarged yellow and red spheres are sulfur and oxygen respectively) and associated polymers chains for each system. For clarity, half the length of chains is shown. Different colors in the inset represent distinct chains. 41

Figure 3.3: Averaged number of unique chains N_{uc} , normalized to cluster size N_c for random, precise, and block PSS melts..... 42

Figure 3.4: (a) $S(q)$ as a function of q , and (b) Sulfur-sulfur radial distribution function for random, precise, and block PSS melts. 44

Figure 3.5: Mean square displacement as a function of time for (a) center of mass of chains (b) phenyl rings without sulfonated groups (open symbols) and sulfonated phenyl rings (closed symbols) (c) Na^+ ions (closed symbol) and sulfur (black dash line and symbol) in the ionic group for the random (●), precise (■), and block (▲) PSS melts. .. 46

Figure 3.6: (a) $S(q,t)/S(q,0)$ vs time t , for the indicated q values (symbols) and double exponential fit (black solid line), (b) Effective diffusion coefficient Γ_i , as a function of q for the random (○), precise (□), and block (△) PSS melts. Slow (Γ_1) components are represented by solid symbols and lines and fast (Γ_2) components by open symbols and dashed lines. 47

Figure 4.1: Snapshots illustrating chain stretching for associating group strength $\alpha = 1, 3$ and 6 for $Wi = 0.5, 4$ and 32 at strain $\varepsilon = 10$. For clarity, 1/4 of systems are shown. Chains are colored according to their end-to-end distance R 61

Figure 4.2: (a) Transient extensional viscosity $\eta_E^+(\varepsilon)$ as a function of Hencky strain ε for association strengths $\alpha = 1, 3, 4, 6, 8,$ and 10 at a $Wi = 4$. A cross indicates the strain at which cavities are observed for $\alpha = 8$ and 10. (b) Terminal viscosities computed by averaging η_E over the strain interval from 5 to 10 versus Wi for $\alpha = 1, 3, 4$ and 6..... 64

Figure 4.3: Snapshots of systems with interaction ratio $\alpha = 10$ with cavities for $Wi = 4$ at strain $\varepsilon = 0, 2.4$ (maximum stress) and $\varepsilon = 3$. Non-associating beads, stickers and cavities are visualized by red, yellow, and blue colors, respectively..... 65

Figure 4.4: (a) Extensional stress σ_{ex} for interaction ratio $\alpha = 1$ (dash lines) and 6 (solid lines) and (b) average cluster size $\langle N_c \rangle$ as a function of strain ε for $\alpha = 6$ and $Wi = 0.5, 4, 16,$ and 32..... 67

Figure 4.5: Probability $P(N_c)$ as a function of cluster size N_c for interaction ratio $\alpha = 2 - 6$, (a) at equilibrium (b) for $Wi = 1$ and (c) $Wi = 8$. Inset shows the average cluster size $\langle N_c \rangle$ as a function of Wi for corresponding systems..... 68

Figure 4.6: Distribution function $P(R)$ of the end-to-end distance R for $\alpha = 1, 3$ and 6 for $Wi = 0.5, 4$ and 32 for strain $\varepsilon = 1, 2$ and 5. Black and blue dot-dashed lines corresponding to $P(R)$ for equilibrium and average over strain interval 5-10, respectively. 69

Figure 5.1: (a) Visualization of an isolated cluster of SO_3^- groups (yellow and red spheres are sulfur and oxygen respectively) at the indicated strain ε for $f = 0.20$ and $\varepsilon = 10^9$

s^{-1} , plotted with representative associated polymers chains. The different colors represent distinct chains. Black arrow corresponds to the flow direction. (b) Snapshots of the polymer backbone for strain $\varepsilon = 10$ for the indicated sulfonation levels for $\varepsilon=10^8 s^{-1}$.

Chains are colored according to their end-to-end distance R 84

Figure 5.2: Transient extensional stress $\sigma_E^+(\varepsilon)$ as a function of strain ε at the indicated sulfonation fraction f for (a) low strain ε and (b) for the entire range of strains ε up to 10 for $\varepsilon=10^{8.5} s^{-1}$. (c) Average rms end-to-end $\langle R^2 \rangle^{1/2}$ of the chains for $\varepsilon=10^{8.5} s^{-1}$ and (d) average size of the ionic cluster $\langle N_c \rangle$ for $f = 0.20$ for shear rates $\varepsilon=10^{7.5} s^{-1}$, $10^{8.0} s^{-1}$, $10^{8.5} s^{-1}$, and $10^{9.0} s^{-1}$, from top to bottom..... 85

Figure 5.3: (a) Elastic modulus E , and (b) hardening modulus H , as a function of sulfonation fraction f 86

Figure 5.4: Terminal viscosities η_E versus extensional strain rate ε for the indicated sulfonation fractions..... 87

Figure 5.5: (a) Distribution $P(R)$ of the end-to-end distance R for $f= 0$ and 0.35 in equilibrium and at 2 extension rates. Curves are shifted by 0.045 for clarity. (b) $P(R)$ at $\varepsilon = 10^{7.5} s^{-1}$ for 5 values of f . Curves are shifted by 0.01 vertically for clarity. $P(R)$ after secession of flow at a rate of $\varepsilon = 10^{7.5} s^{-1}$ and strain $\varepsilon = 10$ for (c) $f = 0$ and (d) for $f = 0.2$ 88

Figure 6.1: a) $S(Q,E)$ as a function of energy E for a 10wt% solution of SPS with 3 mol% random sulfonation in cyclohexane at $T=300$ K at the indicated Q values. The insert presents a representative resolution function superimposed with the data at 300 K at $Q=0.3 \text{ \AA}^{-1}$. b) the same data as in (a), normalized by $I_{max}(Q)$. The solid black lines

correspond to KWW fits. (c) $\langle\tau(Q)\rangle$ extracted from KWW fits as function of Q . The solid line is a guide to the eye. The insert captures a representative ionic cluster tethered to representative SPS chains obtained by molecular dynamics simulation.³⁸ 103

Figure 6.2: $S(Q,E)$ as a function of energy E for SPS in cyclohexane at the indicated three Q values and temperatures. The solid lines correspond to KWW fits. 105

Figure 6.3: Average relaxation times $\langle\tau(Q)\rangle$ as a function of (a) temperature and (b) Q at the indicated temperatures. 106

Figure 6.4: $S(Q,E)$ as a function of energy E for SPS in $f_{cyh} = 1.0$ (open symbols) solutions, and $f_{cyh} = 0.95$ solutions (bold symbols) at (a) 300 K and (b) 360 K at indicated Q values. The solid line corresponds to KWW fits. (c) Average relaxation times, $\langle\tau(Q)\rangle$ as a function of T for the three Q values presented in a following the same color code as for a. (d) Zooming into the low $\langle\tau(Q)\rangle$ region of Figure 6.4c, with y axis ranging from 0 to 0.085 ns. 107

Figure 6.5: D_{eff} as a function of temperature for cyclohexane-ethanol fractions..... 108

Figure 6.6: Snapshots of a cluster for SPS in (a) $f_{cyh} = 1.00$ and 0.95 at 2 ns intervals. Sulfur is yellow, oxygen is red, sodium is black, and the backbone is blue. (b) Sulfur–sulfur radial distribution function for corresponding system. 110

Figure 7.1: (a) the chemical structure of PPE where R corresponds for an alkyl side chain. Preparation of a polydot from (b) random and (c) parallel-chain orientation. Purple corresponding to carbon atoms on the side chains, black to all atoms on the backbone and green to hydrogen atoms. 123

Figure 7.2: Visualization of backbones for dinonyl PPE polydots at the (a) 300K and (b) 600K with $N = 2, 4$ and 6-chains after 120 ns for initial parallel (P) and random (R) orientation. (c) at 300K, 400K, 500K and 600K for random $N = 6$ -chains. Confined 1st (red), 2nd (black), 3rd (green), 4th (blue), 5th (orange) and 6th (purple) chains are colored distinctly. The chain ends are represented by an enlarged sphere and colored accordingly..... 125

Figure 7.3: Sphericity parameter $A(a_1, a_2, a_3)$, of polydots as a function of temperature T (a) for polydots containing 2 (circles), 4 (triangles), and 6 (squares) chains for parallel (full) and random (open) initial state and (b) for 2-chain polydots with varying side chain length $l = 6, 9, 12$ and 18..... 127

Figure 7.4: Visualization of backbones and side chains of 2-chain PPE polydots at 300 K, and 600 K for $l = 9$ and 18. (b) plots the corresponding zoomed images. For clarity, the polymer backbone and side chains are colored in black and blue, respectively. 128

Figure 7.5: Root mean squared average radius of gyration $\langle Rg^2 \rangle^{1/2}$ of dinonyl PPE polydots as a function of temperature T (a) for polydots containing 1 (purple pentagons), 2 (black circles), 4 (red triangles), and 6 (blue squares) chains for parallel (filled) and random (open) initial state. Yellow triangle symbols represent the cooling curve of polydots containing 4 chains after jump temperature. (b) $\langle Rg^2 \rangle^{1/2}$ for 2-chain polydots with side chain length $l = 6, 9, 12$ and 18..... 130

Figure 7.6: Radial mass density $\rho(r)$ as a function of distance d , from the center of mass of the polydot for (a) 2 (open symbols), and 6 (close symbols) chains for random starting

orientation at 300 K (red), 400 K (yellow), 500 K (blue), 600 K (purple) and (b) $\rho(r)$ at 300K for 4 side chain lengths l 132

Figure 7.7: Autocorrelation function $\langle N(t) \cdot N(0) \rangle$, for aromatic rings in PPE backbone for internal aromatic rings (upper curves) and for aromatic rings at the interface (lower curves) for (a) $T = 300$ K (full) and 500 K (open) for random 2 (circles) and 6 (squares) chain polydots. Lower 2 curves with green and red symbols corresponding to an average over all aromatic rings at 600K. (b) for $l = 6$ (full), and 9 (open) at 300 K. Two curves with blue and yellow symbols corresponding to an average over all aromatic rings for $l = 12$, and 18 respectively. The lines correspond to KWW fits. (b) Relaxation time τ as a function of temperature for internal aromatic rings (open) and for interfacial aromatic rings (full). The data at 600K and $l = 12$, and 18 are average over all rings. 133

LIST OF TABLES

Table 2.1: Range of temperature, energy and wavelength for hot, thermal and cold neutrons. ²²	22
Table 2.2: Coherent and incoherent scattering cross sections of common elements. ²	26
Table 3.1: Neutron scattering lengths of elements. ³⁵	43
Table 3.2: Slow (Γ_1) and fast (Γ_2) time constants and corresponding pre-exponential factors extracted from double exponential fits for random (R), precise (P) and block. ...	48
Table 7.1: Moment of inertia tensor eigenvalues ($\lambda_1, \lambda_2, \lambda_3$) and sphericity $A(a_1, a_2, a_3)$ for polydots with 2-, 4-, and 6-chains at indicated temperatures for parallel (P) and random (R) starting chain orientations.	126
Table 7.2: Moment of inertia tensor eigenvalues ($\lambda_1, \lambda_2, \lambda_3$) and sphericity $A(a_1, a_2, a_3)$ for 2-chain polydots with $l = 6, 9, 12$ and 18 at indicated temperatures.	129

CHAPTER ONE

INTRODUCTION

This research focuses on attaining molecular level understanding of structure, and dynamics, of confined polymers. The research centers on two families of associative polymers, ion containing macromolecules and conjugated polymers. These polymers have immense technological importance ranging from clean energy to the water economy where their conformations and dynamics are critical to their function and stability. Ionizable polymers differ in their behavior from van-der-Waals macromolecules. The current state of the art in ionizable polymers is reviewed in this chapter.

1.1 Ionizable Polymers

Ionizable polymers are polymers that contains ionizable groups tethered covalently to the backbone.¹⁻⁵ Even though these materials are the core of many existing applications such as clean energy,⁶⁻⁸ and bio technology,⁹⁻¹¹ gaining control over their structure and response will open the way to enhance the performance of current applications and designing new technologies such as lightweight material and responsive media. The properties of ionizable polymers including their structure, dynamics, and rheological behavior are affected by the ionizable groups. At a low ionizable group fraction (ionomer regime) the properties are governed by both backbone conformations and electrostatic interactions between ionic groups in contrast to ionic polymers with a high ionizable group fraction (polyelectrolyte regime) whose properties are determined predominantly by electrostatic interactions between ionic groups.¹²⁻¹⁴

Among the most common ionomers is Nafion® (DuPont™).¹⁵⁻¹⁹ Nafion® is a sulfonated tetrafluorethylene copolymer used in many electrochemical energy conversion applications.¹⁸⁻²¹

The sulfonic acid groups add capability of Nafion® to act as acid catalyst for alkylation, acylation, and oligomerization reactions.^{22, 23} The phase diagram of Nafion has been studied by several groups using Small-angle X-ray scattering (SAXS) and Small Angle Neutron Scattering (SANS) techniques.^{24, 25} They have shown that these materials micro separate into hydrophobic matrix and hydrophilic ionic domains. These ionic domains swell in the presence of a polar solvent and forms bicontinuous channels for solvents. Ultimately, they dissociated to form cylindrical aggregates as the polymer solvent content increases. Another well studied ionomer is polystyrene sulfonate (PSS)²⁶⁻²⁹ The chemical structure for PSS in its Na⁺ salt shown in Figure 1.1.

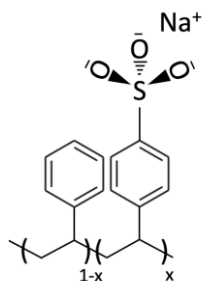


Figure 1.1: Chemical structure of sulfonated polystyrene sodium salt.

The present study is focused on PSS due to significant knowledge^{4, 5, 30-36} availability for comparison. Recent MD simulations by Agrawal et al.³¹ have investigated the structure of PSS in melts and they have observed formation of elongated ionic clusters. These ionic clusters constrain the dynamics of the chains as shown by Weiss et al.³⁶ that

reported that a small fraction of ionizable groups on a polystyrene with below the entanglement length, are sufficient to significantly slow the polymer motion.

1.2 Association of Ionomers

Association of ionic groups form ionic clusters. These clusters govern the overall structure and dynamics, as well as transport properties of ionic polymers in melts and in solutions.^{30, 36-39}

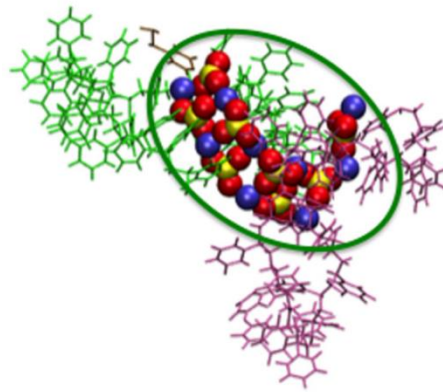


Figure 1.2: Visualization of a cluster of SO_3^- groups [S (yellow), O (red), and Na (blue)] for PSS melts with a sulfonation fraction $f = 0.10$ and associated polymers chains.³⁰

An example of an ionic cluster in PSS melts obtained by MD simulations and shown in Figure 1.2.³⁰ Eisenberg et al. described the formation of ionic clusters and captured their stability as a balance between electrostatic and elastic forces.^{1, 12, 28} Initially, ion pairs are formed by ionizable groups in the presence of counterions. These ion pairs associate into multiples. Finally, existing multiplets assemble to form clusters.

The electrostatic work W required to separate an ion pair is given by:²⁸

$$W = -\frac{e^2}{4\pi\epsilon_0\epsilon_r r} \quad (1.1)$$

where e is the charges of the ions, ϵ_0 is the permittivity of vacuum, ϵ_r is the dielectric constant of media and r is the separation distance between positive and negative charge in an ion pair. The corresponding elastic force f on polymer chains is given by:²⁸

$$f = \frac{3kTh}{\bar{h}^2} \quad (1.2)$$

where k is the Boltzmann constant. \bar{h}^2 and h are mean square end-to-end distance for the free polymer chain and actual separation of the polymer chain ends respectively.

1.3 Impact of Ionic Clusters

Impact of clusters on structure and dynamics of polymer melts has been studied by significant number of research groups.^{30-35, 39-49} Weiss and coworkers have shown that introducing a small number of ionizable groups to the polymer affect the structure and dynamics of the polymer significantly.^{32, 44-49} These clusters often dominate the structure of these materials and are characterized by an inter-aggregate distance signature (often termed an ionic peak) in the static scattering factor, measured by both small angle X-rays and neutrons. The shape of the aggregates has been further probed by tunneling electron microscopy (TEM),³³ where within the resolution of the measurements, significant number of ionic clusters appears spherical.^{50, 51}

Recent molecular dynamics simulations by Agrawal and coworkers^{30, 31} studied the formation of clusters at different dielectric constants ϵ . They found that the ionic groups aggregates into ladder like large clusters at $\epsilon = 1$. However, these ionic clusters break into

small clusters as the dielectrics of the medium increases and consequently enhances the mobility of polymer chains. These simulations show that the behavior of the ionic cluster behaviour could be strongly effected by different dielectric constaants environments.

1.4 Polymers in Solutions

The conformation of polymers in solutions is determaind by their interaction of the ionomers with the solvents.⁵² To undertsand the effects of ionic groups, the interaction of non-ionic polymers will be first discussed. In absence of ionic groups, the solvent quality is described as good, theta or poor.⁵³ In good solvents, polymer-solvent interactions are stronger than the polymer-polymer interactions. In theta solvents, polymer-polymer interactions are equal to the polymer-solvent interactions. Flexible polymers assume a Gaussian coil conformation in theta solvents and swell in good solvents. In a poor solvent, flexible chains collapse as the polymer-polymer interactions are stronger than the polymer-solvent interactions.⁵²

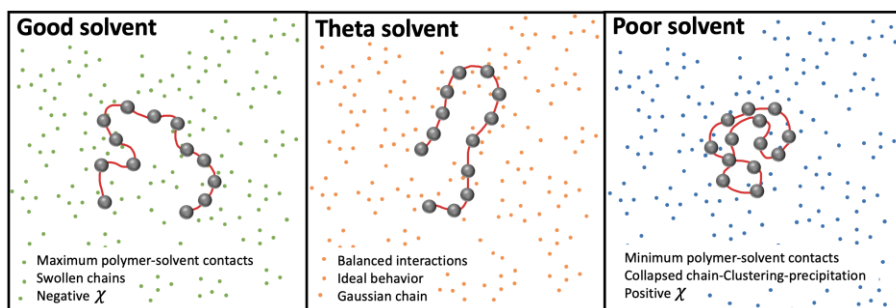


Figure 1.3: Schematics of a flexible polymer chain in good, theta and poor solvents. green: good solvent molecules, orange: theta solvent molecules, blue: poor solvent molecules, black: monomers in polymer chain.

The interactions between the polymer and solvent components is measured by the Flory-Huggins parameter χ . As a first approximation, the monomers and the solvent molecules can be described as particles on a lattice as shown in Figure 1.4. Each lattice point is occupied by either a monomer or a solvent molecule. The interaction parameter χ is given by⁵²

$$\chi = \left(\frac{z}{k_B T} \right) \left[\epsilon_{ms} - \frac{1}{2} (\epsilon_{mm} + \epsilon_{ss}) \right] \quad (1.3)$$

where z is the number of nearest neighbors per unit monomer, k_B is the Boltzmann constant, and T is the temperature. The interaction energies of monomer-solvent, monomer-monomer and solvent-solvent are given by ϵ_{ms} , ϵ_{mm} , and ϵ_{ss} respectively.

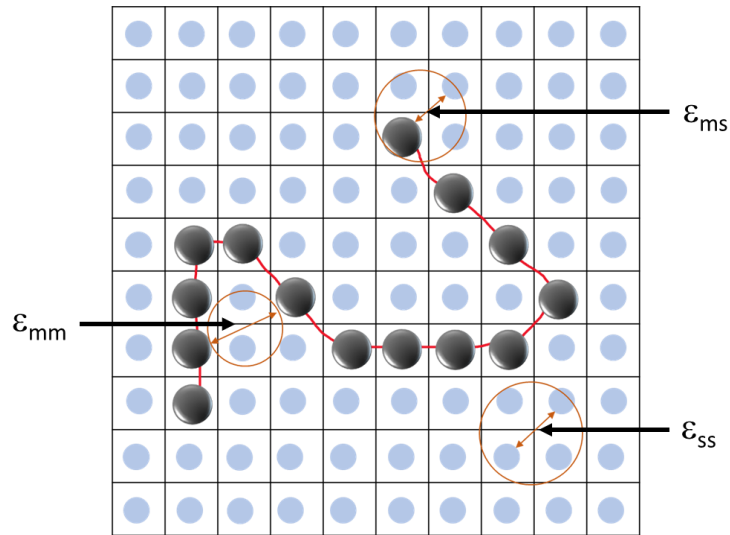


Figure 1.4: Flory-Huggins lattice model for a polymer (black) in a solvent (blue).

A positive χ means that the interaction energies of monomer-monomer are smaller than of the monomer-solvent. A negative χ means, monomer-solvent interactions are larger than monomer-monomer promoting dissolution of polymer. The size of the polymer chain

is governed by the solvent quality. One measure of the polymer size is the radius of gyration R_g ,

$$R_g \sim bN^\nu \quad (1.4)$$

where, N is the degree of polymerization, b is the Kuhn length of the polymer which defines the stiffness of the polymer. The scaling exponent $\nu = 1/3$ for poor, $1/2$ for theta and $3/5$ for good solvents.^{52, 53}

Ionic groups drive the formation of ionic clusters due to high electrostatic intermolecular interactions. The molecular level understanding of ionic cluster behavior on structure and dynamics of the polymer in melts and as well as in different solvent environments remain open questions despite enormous efforts. Therefore, in this research, we studied clustering effects in PSS melts and solutions using molecular dynamic (MD) simulations and quasi elastic neutron scattering (QENS).

This dissertation is organized as follows. In Chapter 2 the experimental and computational techniques used in these studies are reviewed. Our investigation required to probe the structure and dynamics of polymer in solutions and melts in multiple length scale, which includes atomistic to nanoscale. Molecular dynamic (MD) simulations were used to probe the structure of polymer melts. Quasi-elastic neutron scattering was used to investigate segmental motion of polymer in solutions. Chapter 3 focuses on distribution effects of ionic groups along polymer chain on structure and dynamics of the PSS melts. Chapter 4 explores the nonlinear elongation flows effects on aggregation in associating polymer melts using a coarse-grained bead spring model. Chapter 5 further investigate the flow behavior of PSS melts ranging from ionomer regime to polyelectrolyte regime using

fully atomistic MD simulations. Chapter 5 probes the segmental motion of PSS in cyclohexane and a mixture of cyclohexane/ethanol solvents using QENS. Chapter 6 discusses the structure and dynamics of polydots formed by confining luminescent polymers, poly para phenylene ethynylene (PPEs), into nano dimensions.

1.5 References

- (1) Eisenberg, A.; Kim, J.-S. *Introduction to ionomers*; Wiley, New York,, 1998.
- (2) Lundberg, R.; Phillips, R. Influence of sample history on ionomer properties. *J. Polym. Sci., Polym. Lett. Ed.* **1984**, *22*, 377-384.
- (3) Weiss, R.; Turner, S.; Lundberg, R. Sulfonated polystyrene ionomers prepared by emulsion copolymerization of styrene and sodium styrene sulfonate. *J. Polym. Sci., Polym. Chem. Ed.* **1985**, *23*, 525-533.
- (4) Zhang, L.; Brostowitz, N. R.; Cavicchi, K. A.; Weiss, R. Perspective: Ionomer research and applications. *Macromolecular Reaction Engineering* **2014**, *8*, 81-99.
- (5) Zhang, Z.; Huang, C.; Weiss, R.; Chen, Q. Association energy in strongly associative polymers. *J. Rheol* **2017**, *61*, 1199-1207.
- (6) Li, D.; Park, E. J.; Zhu, W.; Shi, Q.; Zhou, Y.; Tian, H.; Lin, Y.; Serov, A.; Zulevi, B.; Baca, E. D. Highly quaternized polystyrene ionomers for high performance anion exchange membrane water electrolyzers. *Nature Energy* **2020**, *5* (5), 378-385.
- (7) Chen, N.; Wang, H. H.; Kim, S. P.; Kim, H. M.; Lee, W. H.; Hu, C.; Bae, J. Y.; Sim, E. S.; Chung, Y.-C.; Jang, J.-H. Poly (fluorenyl aryl piperidinium) membranes and ionomers for anion exchange membrane fuel cells. *Nat. Commun.* **2021**, *12*, 1-12.

- (8) Balogun, E.; Cassegrain, S.; Mardle, P.; Adamski, M.; Saatkamp, T.; Holdcroft, S. Nonconformal Particles of Hyperbranched Sulfonated Phenylated Poly (phenylene) Ionomers as Proton-Conducting Pathways in Proton Exchange Membrane Fuel Cell Catalyst Layers. *ACS Energy Letters* **2022**, *7*, 2070-2078.
- (9) Macocinschi, D.; Filip, D.; Ciubotaru, B.-I.; Dumitriu, R. P.; Varganici, C.-D.; Zaltariov, M.-F. Blends of sodium deoxycholate-based poly (ester ether) urethane ionomer and hydroxypropylcellulose with mucosal adhesiveness. *International Journal of Biological Macromolecules* **2020**, *162*, 1262-1275.
- (10) Zhou, J.; Xu, Q.; Fan, C.; Ren, H.; Xu, S.; Hu, F.; Wang, L.; Yang, K.; Ji, Q. Characteristics of chitosan-modified glass ionomer cement and their effects on the adhesion and proliferation of human gingival fibroblasts: an in vitro study. *Journal of Materials Science: Materials in Medicine* **2019**, *30* (3), 1-11.
- (11) Thage, R.; Semegni, Y.; Naidoo, S. Computer-aided: modelled sustainable hybrid catalysts for a nano-drug delivery system. *South African Journal of Chemistry* **2020**, *73*, 103-110.
- (12) Eisenberg, A.; Rinaudo, M. Polyelectrolytes and ionomers. *Polymer bulletin (Berlin. Print)* **1990**, *24*.
- (13) Hallinan Jr, D. T.; Balsara, N. P. Polymer electrolytes. *Annu. Rev. Mater. Res.* **2013**, *43*, 503-525.
- (14) Sing, C. E.; Zwanikken, J. W.; De La Cruz, M. O. Electrostatic control of block copolymer morphology. *Nature materials* **2014**, *13*, 694-698.

- (15) Abidin, M. N. Z.; Nasef, M. M.; Veerman, J. Towards the development of new generation of ion exchange membranes for reverse electrodialysis: A review. *Desalination* **2022**, *537*, 115854.
- (16) Safronova, E. Y.; Voropaeva, D. Y.; Novikova, S.; Yaroslavtsev, A. On the Influence of Solvent and Ultrasonic Treatment on Properties of Cast Nafion® Membranes. *Membranes and Membrane Technologies* **2022**, *4* (1), 39-47.
- (17) Iezzi, R. C.; Santos, R. D.; Silva, G. C. d.; Paganin, V. A.; Ticianelli, E. A. CO tolerance and stability of proton exchange membrane fuel cells with Nafion® and Aquivion® membranes and Mo-based anode electrocatalysts. *Journal of the Brazilian Chemical Society* **2018**, *29*, 1094-1104.
- (18) Orsino, C. M.; Moore, R. B. Thermal transitions and mechanical relaxations in perfluorinated ionomers. *Fascinating Fluoropolymers and Their Applications* **2020**, 205-225.
- (19) Jang, E.-S.; Kamcev, J.; Kobayashi, K.; Yan, N.; Sujanani, R.; Talley, S. J.; Moore, R. B.; Paul, D. R.; Freeman, B. D. Effect of water content on sodium chloride sorption in cross-linked cation exchange membranes. *Macromolecules* **2019**, *52* (6), 2569-2579.
- (20) Geng, K.; Tang, H.; Li, Y.; Liu, L.; Li, N. A facile strategy for disentangling the conductivity and selectivity dilemma enables advanced composite membrane for vanadium flow batteries. *Journal of Membrane Science* **2020**, *607*, 118177.
- (21) Darling, R. M.; Saraidaridis, J. D.; Shovlin, C.; Fortin, M. The Influence of Current Density on Transport of Vanadium Acetylacetonate through a Cation-Exchange Membrane. *Journal of The Electrochemical Society* **2022**, *169* (3), 030514.

- (22) Harmer, M. A.; Sun, Q.; Vega, A. J.; Farneth, W. E.; Heidekum, A.; Hoelderich, W. F. Nafion resin–silica nanocomposite solid acid catalysts. Microstructure–processing–property correlations. *Green Chemistry* **2000**, *2* (1), 7-14.
- (23) Harmer, M. A.; Farneth, W. E.; Sun, Q. High surface area nafion resin/silica nanocomposites: a new class of solid acid catalyst. *Journal of the American Chemical Society* **1996**, *118* (33), 7708-7715.
- (24) Gebel, G.; Lambard, J. Small-angle scattering study of water-swollen perfluorinated ionomer membranes. *Macromolecules* **1997**, *30*, 7914-7920.
- (25) Gebel, G. Structural evolution of water swollen perfluorosulfonated ionomers from dry membrane to solution. *Polymer* **2000**, *41*, 5829-5838.
- (26) Jalal, N. M.; Jabur, A. R.; Hamza, M. S.; Allami, S. Sulfonated electrospun polystyrene as cation exchange membranes for fuel cells. *Energy Rep.* **2020**, *6*, 287-298.
- (27) Sivasankaran, A.; Sangeetha, D.; Ahn, Y.-H. Nanocomposite membranes based on sulfonated polystyrene ethylene butylene polystyrene (SSEBS) and sulfonated SiO₂ for microbial fuel cell application. *Chem. Eng. J.* **2016**, *289*, 442-451.
- (28) Eisenberg, A. Clustering of ions in organic polymers. A theoretical approach. *Macromolecules* **1970**, *3*, 147-154.
- (29) Baum, R. N.; Rebis, E. N.; Reilly, P. B. Sulfonated polystyrene compositions and methods of treating boiler water. Google Patents: 1971.
- (30) Agrawal, A.; Perahia, D.; Grest, G. S. Clustering effects in ionic polymers: Molecular dynamics simulations. *Phys. Rev. E* **2015**, *92*, 022601.

- (31) Agrawal, A.; Perahia, D.; Grest, G. S. Cluster morphology-polymer dynamics correlations in sulfonated polystyrene melts: computational study. *Phys. Rev. Lett.* **2016**, *116*, 158001.
- (32) Qiao, X.; Weiss, R. Nonlinear rheology of lightly sulfonated polystyrene ionomers. *Macromolecules* **2013**, *46*, 2417-2424.
- (33) Zhou, N. C.; Chan, C. D.; Winey, K. I. Reconciling STEM and X-ray scattering data to determine the nanoscale ionic aggregate morphology in sulfonated polystyrene ionomers. *Macromolecules* **2008**, *41*, 6134-6140.
- (34) Register, R. A. Morphology and Structure–Property Relationships in Random Ionomers: Two Foundational Articles from *Macromolecules*. *Macromolecules*: 2020; Vol. 53, pp 1523–1526.
- (35) Seitz, M. E.; Chan, C. D.; Opper, K. L.; Baughman, T. W.; Wagener, K. B.; Winey, K. I. Nanoscale morphology in precisely sequenced poly (ethylene-co-acrylic acid) zinc ionomers. *J. Am. Chem. Soc.* **2010**, *132*, 8165-8174.
- (36) Weiss, R.; Zhao, H. Rheological behavior of oligomeric ionomers. *J. Rheol.* **2009**, *53*, 191-213.
- (37) Lu, X.; Steckle, W.; Weiss, R. Ionic aggregation in a block copolymer ionomer. *Macromolecules* **1993**, *26*, 5876-5884.
- (38) Huang, C.; Chen, Q.; Weiss, R. Rheological behavior of partially neutralized oligomeric sulfonated polystyrene ionomers. *Macromolecules* **2017**, *50*, 424-431.

- (39) Mohottalalage, S. S.; Aryal, D.; Thurston, B. A.; Grest, G. S.; Perahia, D. Effects of Ionic Group Distribution on the Structure and Dynamics of Amorphous Polymer Melts. *Macromolecules* **2021**, *55*, 217–223.
- (40) Ma, B.; Nguyen, T. D.; Pryamitsyn, V. A.; Olvera de la Cruz, M. Ionic correlations in random ionomers. *ACS nano* **2018**, *12*, 2311-2318.
- (41) Frischknecht, A. L.; Paren, B. A.; Middleton, L. R.; Koski, J. P.; Tarver, J. D.; Tyagi, M.; Soles, C. L.; Winey, K. I. Chain and ion dynamics in precise polyethylene ionomers. *Macromolecules* **2019**, *52*, 7939-7950.
- (42) Hall, L. M.; Stevens, M. J.; Frischknecht, A. L. Dynamics of model ionomer melts of various architectures. *Macromolecules* **2012**, *45*, 8097-8108.
- (43) Kwon, S. H.; Kang, H.; Sohn, Y.-J.; Lee, J.; Shim, S.; Lee, S. G. Molecular dynamics simulation study on the effect of perfluorosulfonic acid side chains on oxygen permeation in hydrated ionomers of PEMFCs. *Scientific Reports* **2021**, *11* (1), 1-10.
- (44) Weiss, R.; Yu, W.-C. Viscoelastic behavior of very lightly sulfonated polystyrene ionomers. *Macromolecules* **2007**, *40*, 3640-3643.
- (45) Weiss, R.; Fitzgerald, J.; Kim, D. Viscoelastic behavior of lightly sulfonated polystyrene ionomers. *Macromolecules* **1991**, *24*, 1071-1076.
- (46) Liu, S.; Cao, X.; Huang, C.; Weiss, R.; Zhang, Z.; Chen, Q. Brittle-to-ductile transition of sulfonated polystyrene ionomers. *ACS Macro Letters* **2021**, *10* (4), 503-509.
- (47) Kirkmeyer, B. P.; Weiss, R. A.; Winey, K. I. Spherical and vesicular ionic aggregates in Zn-neutralized sulfonated polystyrene ionomers. *J. Polym. Sci. B Polym. Phys.* **2001**, *39*, 477-483.

- (48) Chakrabarty, K.; Seery, T.; Weiss, R. Characterization of ionomer solutions. 1. Phase behavior and gelation of sulfonated polystyrene ionomers in decalin. *Macromolecules* **1998**, *31* (21), 7385-7389.
- (49) Ling, G. H.; Wang, Y.; Weiss, R. Linear viscoelastic and uniaxial extensional rheology of alkali metal neutralized sulfonated oligostyrene ionomer melts. *Macromolecules* **2012**, *45*, 481-490.
- (50) Register, R. A. Morphology and Structure–Property Relationships in Random Ionomers: Two Foundational Articles from *Macromolecules*. ACS Publications: 2020.
- (51) Seitz, M. E.; Chan, C. D.; Opper, K. L.; Baughman, T. W.; Wagener, K. B.; Winey, K. I. Nanoscale morphology in precisely sequenced poly (ethylene-co-acrylic acid) zinc ionomers. *Journal of the American Chemical Society* **2010**, *132*, 8165-8174.
- (52) Rubinstein, M.; Colby, R. *Polymer physics*; New York: Oxford university press, 2003.
- (53) De Gennes, P.-G.; Gennes, P.-G. *Scaling concepts in polymer physics*; Cornell university press, 1979.

CHAPTER TWO

METHODOLOGY

This study probes the structure and dynamics of model polymer systems at multiple time and length scales using molecular dynamics simulations (MD)¹ and quasi-elastic neutron scattering (QENS)² techniques. The first section of the chapter captures the fundamentals of classical atomistic MD simulations. The second section focuses on coarse grained (CG) bead-spring MD simulations, in which the polymer chains are treated as beads connected by a non-extensible spring.^{1, 3} Though atomistic models capture the chemistry and local details of the system, the time and length scales one can access are limited due to computational costs. CG models reduce the number of degrees of freedom^{4, 7} and thus permits one to access longer time and length scales essential for studies of macromolecules. The third section focuses on the fundamentals of scattering in general and presents details of QENS, which is employed to probe the segmental dynamics of polymers on time scales from pico- to nano-seconds and length scales from angstrom to nanometer, in solutions.^{2, 8}

2.1 Molecular Dynamics Simulations

In classical MD simulations the trajectories of interacting particles are determined by integrating Newton's equations of motion. MD simulations give the instantaneous positions and velocities of the particles and allow one to follow the time evolution of the system.¹ The basic concepts of classical MD simulations are presented here.

2.1.1 Newton's Equation of Motion

In classical MD simulations, Newton's equations of motion are solved for a set of particles,

$$F_i = m_i a_i \quad (2.1)$$

$$a_i = \frac{d^2 r_i}{dt^2} \quad (2.2)$$

where F_i is the force acting on particle i , m_i is its mass, a_i is its acceleration, r_i is its position, and t is time. The solution of equations of motion results in trajectories that describe the positions, velocities, and accelerations of each particle in the system. The force is expressed as the gradient of potential energy, where ∇ is the del operator and U_i is the potential energy of the system. The force and energy are given by:

$$F_i = -\nabla_i U_i \quad (2.3)$$

$$\nabla = i \frac{\partial}{\partial x} + j \frac{\partial}{\partial y} + k \frac{\partial}{\partial z} \quad (2.4)$$

where i, j, k are unit vectors for direction x, y and z . Newton's equations of motion are numerically integrated using the velocity-Verlet algorithm.^{9, 10} In this integration scheme, the position, and velocity of each particle in the system are updated from time t to time $t + \Delta t$, where Δt is the chosen time step.

$$r(t + \Delta t) = r(t) + v(t)\Delta t + \frac{1}{2} a(t)\Delta t^2 \quad (2.5)$$

$$v(t + \Delta t) = v(t) + \frac{1}{2} \Delta t [a(t) + a(t + \Delta t)] \quad (2.6)$$

Figure 2.1 describes a flow chart of the MD simulation process. The system is built in a simulation cell by defining initial positions and velocities for all particles. Newton's equations of motion are solved to generate new positions and velocities. These steps are repeated until a final state is reached. This final state depends on the goals of the study and the properties of the system.

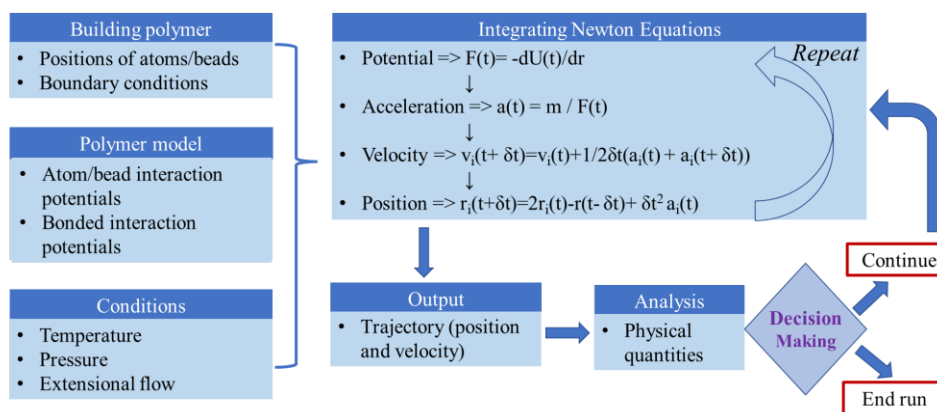


Figure 2.1: A basic MD simulation flow chart used in this work.

2.1.2 Force Field

Atoms are treated as point particles with a mass m . The interaction potentials between atoms are defined by a set of mathematical expressions and constants which are essential for reproducing the chemical structure and selected properties. The proper choice of the potentials describing the interactions between the atoms is important to obtaining reliable results in MD simulations. For atomistic simulations we use the Optimized Potentials for Liquid Simulations – All Atom (OPLS/AA, and will be referred to here as OPLS) developed by Jorgensen et al.^{10, 11} OPLS¹² force fields were optimized to study alkanes. The potential terms are represented as follows:

$$U_{OPLS} = U_{bonded} + U_{nonbonded} \quad (2.7)$$

$$U_{bonded} = U_{bond} + U_{angle} + U_{torsion} \quad (2.8)$$

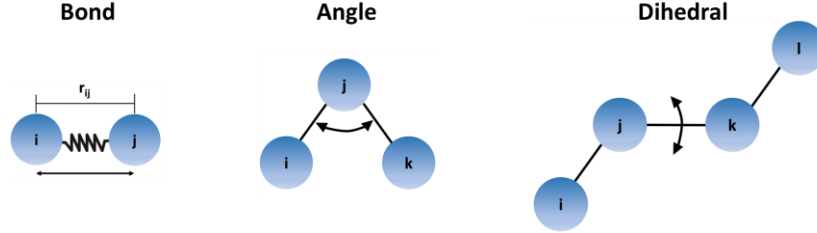


Figure 2.2: Types of bonded interactions.

The intramolecular interactions (U_{bonded}) are categorized by bond, angular and dihedral potentials as shown by Figure 2.2. Covalent bonds are modeled as harmonic potentials. U_{bond} is given by:

$$U_{bond}(r_{ij}) = k_r(r_{ij} - r_0)^2 \quad (2.9)$$

where r_{ij} is the distance between atoms i and j , and r_0 is their equilibrium separations. Similarly, the three-body angle bending potentials (i,j,k) are also described as harmonic potentials and is given by:

$$U_{angle}(\theta_{ijk}) = k_\theta(\theta_{ijk} - \theta_0)^2 \quad (2.10)$$

θ_{ijk} is the angle between the vectors r_{ji} , and r_{jk} , and θ_0 is its equilibrium value. The dihedral potentials are given by:

$$U_{dihedral}(\phi_{ijkl}) = \sum_{n=i}^{n=l} \frac{k_n}{2} [1 - (-1)^n \cos(n\phi)] \quad (2.11)$$

where, ϕ is the dihedral angle.

The intermolecular, non-bonded potential contains two terms, the 12-6 Lennard-Jones (LJ) interaction, and the long-range Coulomb interaction (Equation 2.12)

$$U_{non-bonded}(r_{ij}) = U_{LJ}(r_{ij}) + U_{coul}(r_{ij}) \quad (2.12)$$

The LJ potential used is given by equation 2.13 and the Coulomb interaction by 2.14.

$$U_{LJ}(r_{ij}) = 4\varepsilon_{ij} \left[\left(\frac{\sigma_{ij}}{r_{ij}} \right)^{12} - \left(\frac{\sigma_{ij}}{r_{ij}} \right)^6 \right] \quad (2.13)$$

$$U_{coul}(r_{ij}) = \frac{q_i q_j}{4\pi\varepsilon_0 r_{ij}} \quad (2.14)$$

where ε_{ij} is the LJ energy which is defined as the strength of interactions between two non-bonded atoms i and j , σ_{ij} is the distance at which the LJ potential between the two particles is zero. ε_{ij} and σ_{ij} are specific for each different pair of atoms. ^{1, 9} For the Coulomb interaction, q_i is the charge of an atom and ε_0 is the vacuum permittivity.

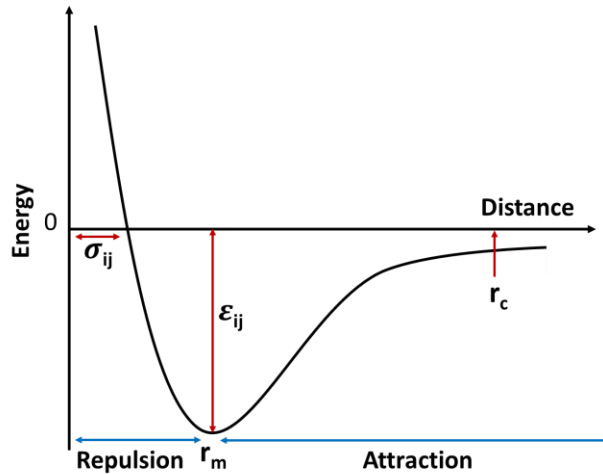


Figure 2.3: Schematics of Lennard-Jones potential.

Figure 2.3 illustrates the LJ potential between two atoms as a function of distance r . At infinite r , the force between the atoms goes to zero. The interaction between the two atoms reaches its minimum at a distance $r_m = 2^{1/6} \sigma_{ij}$. In this work, all LJ interactions are cut-off at $r_c = 12 \text{ \AA}$ where the force between two atoms becomes significantly less than $k_B T$. The Coulomb interactions are treated with long-range particle-particle particle-mesh algorithm (PPPM) Ewald¹³ with a real space cutoff of 12 \AA . The Large-Scale Atomic/Molecular Massively Parallel Simulator (LAMMPS)¹⁴ and the GRONingen MACHine for Chemical Simulations (GROMACS)¹⁵⁻¹⁷ MD codes are used to perform all the simulations.

Some of the studies focused on coarse grained simulations because it enables one to simulate larger time and length scales with minimal computational costs. Next part of the section provides an overview of coarse-grained models.

2.2 Coarse Grained Model and Methodology

Coarse grained simulations were carried out using the Kremer-Grest bead-spring model.¹⁸ In this model, beads of mass m , and diameter σ are connected by a finitely extensible, non-linear elastic (FENE) spring to form a chain.¹⁸ A pair of beads separated by a distance r interact with a Lennard-Jones potential, is given by:

$$U_{ij} = \begin{cases} 4\epsilon_{ij} \left[\left(\frac{\sigma}{r_{ij}} \right)^{12} - \left(\frac{\sigma}{r_{ij}} \right)^6 \right] & r_{ij} \leq r_{\text{cut}} \\ 0 & r_{ij} > r_{\text{cut}} \end{cases} \quad (2.15)$$

with r_{cut} set here to 2.5σ .

The FENE bond potential is given by:

where $R_0 = 1.5\sigma$ sigma is the maximum bond extension and spring constant $k = 30\epsilon\sigma^2$.¹⁹

$$U_{FENE} = \begin{cases} -0.5kR_0^2 \ln \left[1 - \left(\frac{r_{ij}}{R_0} \right)^2 \right] + 4\epsilon_{ij} \left[\left(\frac{\sigma}{r_{ij}} \right)^{12} - \left(\frac{\sigma}{r_{ij}} \right)^6 \right] \\ \infty \end{cases} \quad (2.16)$$

2.3 Fundamentals of Scattering

Neutron scattering techniques are effective and powerful tool for probing the structure and dynamics of polymeric materials because of its non-ionizing, non-destructive, isotope sensitivity, and high penetration characteristics.²⁰ Neutrons interact with the nuclei while X-rays interact with electrons. As a result, neutrons scatter significantly from elements with low atomic number compared to X-ray scattering.²⁰ Neutrons also have a spin of 1/2, and it interacts with soft materials elastically and inelastically during scattering events. In addition, neutron techniques are also employed to study the structure of soft materials at interfaces and surface using neutron reflectivity.²¹

Neutrons follow the de Broglie's law,²¹ that is given by

$$\lambda = \frac{h}{mv} \quad (2.17)$$

where, λ is the neutron wavelength, v is the velocity and $h = 6.626 \times 10^{-34}$ Js is the Plank constant.

The energy E of a neutron given by

$$E = \frac{1}{2}mv^2 \quad (2.18)$$

From equation (2.17) and (2.18),

$$E = \frac{h^2}{2m\lambda^2} \quad (2.19)$$

Neutrons are classified into hot, thermal, and cold neutrons based on their energy. A few characteristics of neutrons shown in Table 2.1.

Table 2.1: Range of temperature, energy and wavelength for hot, thermal and cold neutrons.²²

Neutron	Temperature (K)	Energy (meV)	Wavelength (Å)
Cold	1-120	0.1-10	30-3
Thermal	60-1000	5-100	4-1
Hot	1000-6000	100-500	1-0.4

Cold neutrons with wavelength ranging from 3-30 Å are ideal to study polymer systems because it allows us to probe the segmental motion of polymer on length scales from 1-100 nm and time scales from pico- to nano-second which ultimately affect the bulk properties such as transport and flow characteristics of the material.²³

As a result of irradiating a sample with neutrons, the scattering events can be subdivided into elastic and inelastic components which provide structural and dynamics of the system. Figure 2.4 is the schematic diagram for elastic neutron scattering.^{20, 21} E_i , k_i , and λ_i are the incident neutron energy, wave vector, and wavelength respectively, and E_f , k_f , and λ_f are energy, wave vector, and the wavelength of scattered neutrons respectively.

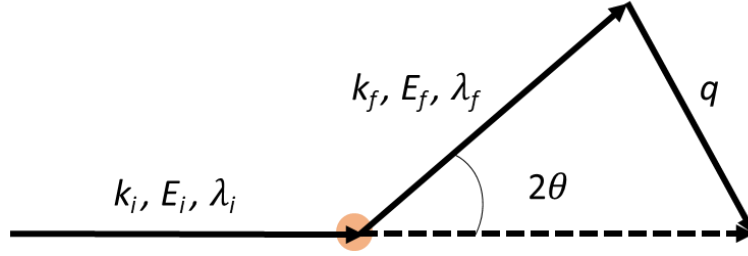


Figure 2.4: Vector diagram of elastic neutron scattering.

Energy and momentum transfer are conserved during the neutron scattering.²⁴ The momentum transfer vector q is demonstrated by

$$q = k_f - k_i = \frac{4\pi \sin\theta}{\lambda} \quad (2.20)$$

The energy change during the scattering event is given by

$$\Delta E = \hbar\omega = E_f - E_i = \frac{\hbar^2}{2m} (k_i^2 - k_f^2) \quad (2.21)$$

Scattered neutrons obey the Bragg's law,

$$n\lambda = 2d \sin\theta \quad (2.22)$$

Here, d is the spacing between the two-scattering point, θ is the scattering angle, and diffraction order n . From equation 2.20 and 2.22, the length scale d can be approximated as

$$d = \frac{2\pi}{q} \quad (2.23)$$

This relation shows that the small dimensions are captured at higher q and vice-versa in a scattering experiment. The interactions of neutrons with a given material are defined by scattering cross-section σ and measured in units of barns.

The sample is irradiated by a neutron beam with a flux J_0 , and flux J will be scattered as shown in Figure 2.5. The scattering cross section of a given material is measured by the ratio between scattered and incident flux.^{2, 24}

$$\frac{J}{J_0} = \frac{d\sigma}{d\Omega} \quad (2.24)$$

Equation 2.24 provides the structural information of the material.

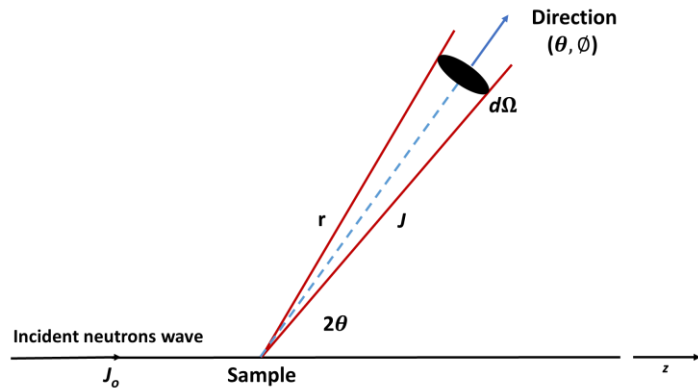


Figure 2.5: Schematic representation for neutron interaction with a given sample. Ω is the solid angle and θ is the scattering angle.^{20, 24}

Dynamic details of the system are extracted from the double differential cross section²

$$\frac{d^2\sigma}{d\Omega dE} = \frac{1}{\hbar} \frac{d^2\sigma}{d\Omega d\omega} \quad (2.25)$$

which gives the probability of neutrons scattered by the sample in the solid angle of $d\Omega$.

Equation 2.25 quantifies the dynamics of the system in terms of density fluctuation of scattered neutrons with time.

The differential cross-section is equal to the measured absolute intensity and depends on scattering length b , and neutron cross section σ of scattering center. The relationship between neutron scattering length and cross section is demonstrated by^{2, 24}

$$\sigma = 4\pi b^2 \quad (2.26)$$

Coherent scattering length (b_{coh}) is the average of scattering lengths of zero nuclear spin states and incoherent scattering length (b_{inc}) is the divergence of b from the mean value due to the existence of isotopes with non-zero nuclear spin.²

$$b_{coh} = \langle b \rangle \quad (2.27)$$

$$b_{inc} = (\langle b^2 \rangle - \langle b \rangle^2)^{1/2} \quad (2.28)$$

Expressions for incoherent and coherent scattering cross sections are given by:

$$\sigma_{coh} = 4\pi \langle b \rangle^2 \quad (2.29)$$

$$\sigma_{inc} = 4\pi (\langle b^2 \rangle - \langle b \rangle^2) \quad (2.30)$$

In neutron experiments, isotopic labeling of one species will yield high contrast which gives a better special resolution. For instance, difference in incoherent scattering lengths of deuterium and hydrogen allows to investigate dynamics as well as structure on complex materials. Some of the common elements in polymers and their coherent and incoherent scattering cross sections are listed in Table 2.2.²

Table 2.2: Coherent and incoherent scattering cross sections of common elements.²

Element	Coherent cross section (10 ⁻²⁴ cm ²)	Incoherent cross section (10 ⁻²⁴ cm ²)
Hydrogen	1.75	79.91
Deuterium	5.59	2.04
Carbon	5.55	0.001
Oxygen	4.23	0
Sulfur	1.01	0.007

The scattered neutrons could undergo change in energy during scattering and capturing energy exchange information of the neutrons can be used to probe the molecular motions in soft matter.² In elastic scattering, double differential scattering cross section $\frac{d^2\sigma}{d\Omega d\omega}$, can be extracted in terms of probability of neutron scattering per unit solid angle and energy transfer.²⁴ The number of neutrons scattered into a solid angle of $d\Omega$ possess the final energy between $\hbar\omega$ and $(\hbar\omega + \hbar d\omega)$ is given by ^{2, 22, 24}

$$\frac{d^2\sigma}{d\Omega d\omega} = \frac{k_f}{k_i} \frac{1}{2\pi} \sum_i \sum_j \langle b \rangle \int_{-\infty}^{\infty} \langle \exp[-iqr_i(t)] \exp[-iqr_j(0)] \rangle \exp(i\omega t) dt \quad (2.31)$$

Equation 2.31 can be written for incoherent and coherent components,

$$\begin{aligned} \frac{d^2\sigma}{d\Omega d\omega} &= \frac{k_f}{k_i} \frac{\langle b^2 \rangle}{2\pi} \sum_i \int_{-\infty}^{\infty} \langle \exp[-iqr_i(t)] \exp[-iqr_i(0)] \rangle \exp(i\omega t) dt \\ &+ \frac{k_f}{k_i} \frac{\langle b^2 \rangle}{2\pi} \sum_{i \neq j} \sum \int_{-\infty}^{\infty} \langle \exp[-iqr_i(t)] \exp[-iqr_j(0)] \rangle \exp(i\omega t) dt \end{aligned} \quad (2.32)$$

Presenting equations 2.29 and 2.30 to equation 2.32, we obtain

$$\frac{d^2\sigma}{d\Omega d\omega} = \frac{1}{4\pi} N \frac{k_f}{k_i} (\sigma_{coh} S_{coh}(q, \omega) + \sigma_{inc} S_{inc}(q, \omega)) \quad (2.33)$$

From equation 2.33, coherent dynamics scattering function $S_{coh}(q, \omega)$ and incoherent dynamics scattering function $S_{inc}(q, \omega)$, can be correlated to their corresponding intermediate scattering functions as shown below²⁴

$$S_{coh}(q, \omega) = \frac{1}{2\pi} \int_{-\infty}^{\infty} S_{coh}(q, t) \exp(i\omega t) dt \quad (2.34)$$

$$S_{inc}(q, \omega) = \frac{1}{2\pi} \int_{-\infty}^{\infty} S_{inc}(q, t) \exp(i\omega t) dt \quad (2.35)$$

where the coherent $S_{coh}(q, t)$, and incoherent $S_{inc}(q, t)$, intermediate scattering functions are given as²⁴

$$S_{coh}(q, t) = \frac{1}{N} \sum_{i,j}^N \langle \exp[-iqr_i(0)] \exp[iqr_j(t)] \rangle \quad (2.36)$$

$$S_{inc}(q, t) = \frac{1}{N} \sum_i^N \langle \exp[-iqr_i(0)] \exp[iqr_i(t)] \rangle \quad (2.37)$$

van Hove correlation function or time dependent pair correlation function in space is the inverse Fourier transform of intermediate scattering function and given by²⁴

$$g(r, t) = \frac{1}{(2\pi)^3} \int_{-\infty}^{\infty} S_{coh}(q, t) \exp(iqr) dq \quad (2.38)$$

$$g_s(r, t) = \frac{1}{(2\pi)^3} \int_{-\infty}^{\infty} S_{inc}(q, t) \exp(iqr) dq \quad (2.39)$$

The equation 2.38 provides time-dependent structural information because it captures the interference effects of scatters which have same average scattering length, while equation 2.39 provides the dynamic information by capturing the time correlations that exists between the positions of the same scatter at different times.

2.3.1 Quasi-elastic neutron scattering (QENS)

QENS is a limiting case of inelastic neutron scattering which is characterized by energy transfers being minimal from the neutrons to the sample. It detects inelastic components as well as the elastic component as described in Figure 2.6. An elastic peak (signature) centered at zero energy transfer with finite peak width. Depending on the finite loss or gain of energy transfer from the neutrons to the sample, inelastic peaks are observed in either in positive (neutrons lose energy) or negative (neutrons gain energy) side of energy transfer E axis as shown in Figure 2.6.

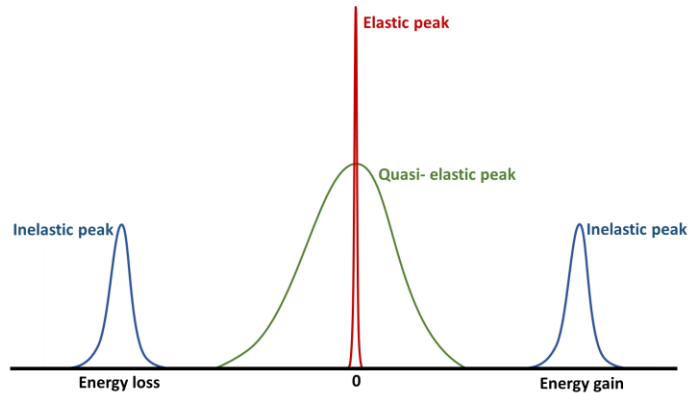


Figure 2.6: Schematic diagram for elastic, quasi-elastic, and inelastic peaks in QENS spectrum.

In neutron scattering, scattered neutrons may gain or lose energy due to the translational or rotational motions of atoms in the given sample. Energy transfer during the scattering event causing the elastic peak to undergo broadening as known as quasi-elastic peak.

QENS spectra provide information on scattering function $S(q, \omega)$ versus energy transfer ($E = \hbar\omega$) and the energy transfer is related to the Angular frequency ω . The scattering function $S(q, \omega)$ is measured in the QENS experiment and is given by:²

$$S(q, \omega) = DWF \{ A_0(q)\delta\omega + [1 - A_0(q)]S_{qE}(q, \omega) \} + S_{in}(q, \omega) \quad (2.40)$$

Debye-Waller factor (*DWF*), which accounts for thermal motions in the sample and $A_0(q)$ accounts for elastic incoherent scattering which becomes zero for diffusive motion.²⁵ $S_{qE}(q, \omega)$ and $S_{in}(q, \omega)$ are the quasi-elastic and inelastic incoherent component of the scattering function respectively. Dirac delta function is denoted by $\delta(\omega)$ at zero frequency. The inelastic component $S_{in}(q, \omega)$ is out of the energy window of the QENS instrument. In this work only the $S_{qE}(q, \omega)$ is measured. The dynamic structure factor $S(q, \omega)$, is given by²⁴

$$S(q, \omega) = DWF \times \{S_{qE}(q, \omega)\} \quad (2.41)$$

The Fourier transform relationship between dynamic scattering function $S(q, \omega)$, intermediate scattering function $S(q, t)$ and van Hove correlation function $g(r, t)$ is illustrated in Figure 2.7. The intermediate scattering function subject into data analysis and is modeled to different diffusion mechanisms.

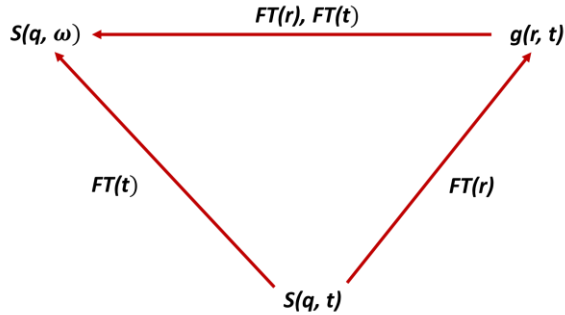


Figure 2.7: The Fourier transform relationship between $S(q, \omega)$, $S(q, t)$ and $g(r, t)$.^{23, 24}

Scattering function assumes a simple exponential form in simple diffusion²⁴

$$S(q, \omega) = A(q, \omega) \exp(-Dq^2 t) \quad (2.42)$$

$A(q, \omega)$ is corresponding to Debye-Waller factor. The *DWF* factor which accounts for thermal motions in the sample. D is translational diffusion constant.

For systems with multiple scale dynamics, scattering function diverge from the simple exponential form and takes the form of stretched exponential as in equation 2.43.²⁴ The function is also known as Kohlrausch-Williams-Watts (KWW) function where β is stretched exponential and τ_α is characteristic relaxation time,

$$S(q, \omega) = A(q, \omega) \exp\left[-\left(\frac{t}{\tau_\alpha}\right)^\beta\right] \quad (2.43)$$

2.4 References

- (1) Allen, M. P.; Tildesley, D. J. *Computer simulation of liquids*; Oxford university press, 2017.
- (2) Bée, M. Quasielastic neutron scattering. **1988**.
- (3) Binder, K.; Horbach, J.; Kob, W.; Paul, W.; Varnik, F. Molecular dynamics simulations. *J. Phys. Condens. Matter* **2004**, *16*, S429.
- (4) Praprotnik, M.; Junghans, C.; Delle Site, L.; Kremer, K. Simulation approaches to soft matter: Generic statistical properties vs. chemical details. *Comput. Phys. Commun.* **2008**, *179*, 51-60.
- (5) Tschöp, W.; Kremer, K.; Batoulis, J.; Bürger, T.; Hahn, O. Simulation of polymer melts. I. Coarse-graining procedure for polycarbonates. *Acta Polymerica* **1998**, *49*, 61-74.

- (6) Fritz, D.; Koschke, K.; Harmandaris, V. A.; van der Vegt, N. F.; Kremer, K. Multiscale modeling of soft matter: scaling of dynamics. *Phys. Chem. Chem. Phys.* **2011**, *13*, 10412-10420.
- (7) Peter, C.; Kremer, K. Multiscale simulation of soft matter systems. *Faraday discussions* **2010**, *144*, 9-24.
- (8) Mongcopa, K. I. S.; Gribble, D. A.; Loo, W. S.; Tyagi, M.; Mullin, S. A.; Balsara, N. P. Segmental Dynamics Measured by Quasi-Elastic Neutron Scattering and Ion Transport in Chemically Distinct Polymer Electrolytes. *Macromolecules* **2020**, *53* (7), 2406-2411.
- (9) Frenkel, D.; Smit, B. *Understanding molecular simulation: from algorithms to applications*; Elsevier, 2001.
- (10) Jorgensen, W. L.; Madura, J. D.; Swenson, C. J. Optimized intermolecular potential functions for liquid hydrocarbons. *J. Am. Chem. Soc.* **1984**, *106*, 6638-6646.
- (11) Jorgensen, W. L.; Maxwell, D. S.; Tirado-Rives, J. Development and testing of the OPLS all-atom force field on conformational energetics and properties of organic liquids. *J. Am. Chem. Soc.* **1996**, *118*, 11225-11236.
- (12) Murzyn, K.; Bratek, M.; Pasenkiewicz-Gierula, M. Refined OPLS all-atom force field parameters for n-pentadecane, methyl acetate, and dimethyl phosphate. *The Journal of Physical Chemistry B* **2013**, *117* (51), 16388-16396.
- (13) Hockney, R.; Eastwood, J. *Computer Simulation Using Particles*. CRC Press. 1988.
- (14) Plimpton, S. Fast parallel algorithms for short-range molecular dynamics. *J. Comput. Phys.* **1995**, *117*, 1-19.

- (15) Abraham, M. J.; Murtola, T.; Schulz, R.; Páll, S.; Smith, J. C.; Hess, B.; Lindahl, E. GROMACS: High performance molecular simulations through multi-level parallelism from laptops to supercomputers. *SoftwareX* **2015**, *1*, 19-25.
- (16) Berendsen, H. J.; van der Spoel, D.; van Drunen, R. GROMACS: a message-passing parallel molecular dynamics implementation. *Computer physics communications* **1995**, *91*, 43-56.
- (17) Pronk, S.; Páll, S.; Schulz, R.; Larsson, P.; Bjelkmar, P.; Apostolov, R.; Shirts, M. R.; Smith, J. C.; Kasson, P. M.; Van Der Spoel, D. GROMACS 4.5: a high-throughput and highly parallel open source molecular simulation toolkit. *Bioinformatics* **2013**, *29*, 845-854.
- (18) Auhl, R.; Everaers, R.; Grest, G. S.; Kremer, K.; Plimpton, S. J. Equilibration of long chain polymer melts in computer simulations. *J. Chem. Phys.* **2003**, *119*, 12718-12728.
- (19) Kremer, K.; Grest, G. S. Dynamics of entangled linear polymer melts: A molecular-dynamics simulation. *J. Chem. Phys.* **1990**, *92*, 5057-5086.
- (20) Pynn, R. Neutron scattering: a primer. *Los Alamos Science* **1990**, *19*, 1-31.
- (21) Russell, T. X-ray and neutron reflectivity for the investigation of polymers. *Materials science reports* **1990**, *5*, 171-271.
- (22) Squires, G. L. *Introduction to the theory of thermal neutron scattering*; Courier Corporation, 1996.
- (23) Higgins, J. S.; Benoit, H. C. *Polymers and neutron scattering*. **1994**.
- (24) Roe, R.-J. *Methods of X-ray and neutron scattering in polymer science*; Oxford University Press on Demand, 2000.

(25) Tyagi, M.; Alegría, A.; Colmenero, J. Heterogeneous dynamics of poly (vinyl acetate) far above T_g: A combined study by dielectric spectroscopy and quasielastic neutron scattering. *J. Chem. Phys.* **2005**, *122*, 244909.

CHAPTER THREE

EFFECTS OF IONIC GROUP DISTRIBUTION ON THE STRUCTURE AND DYNAMICS OF AMORPHOUS POLYMERS MELTS

3.1 Abstract

Ionizable groups tethered to a polymer backbone often associate to form ionic clusters, whose features are determined by the balance of the polymer backbone and electrostatics. These assemblies impact the dynamics of the macromolecules and their ability to transport ions. Here, using fully atomistic molecular dynamics (MD) simulations we investigate the effects of the distribution of ionizable groups along the polymer backbone on cluster characteristics and the resulting impacts on the structure and dynamics of amorphous polymers. Particularly, we probe polystyrene sulfonates (PSS) with random, precise, and block configuration of the SO_3^- sulfonate groups along the backbone with Na^+ as the counterion. We find that the distribution of the ionic groups affects the shape and distribution of the clusters as well as the internal packing of the ionizable groups in the cluster and the number of unique chains that participate in each cluster, affecting the structure and the dynamics of the polymers. The signature of ionic clusters, observed in the static structure factor $S(q)$ for all three distributions, is significantly more pronounced for the precise and blocky polymers compared to the random one. Remarkably, we find that the local of the polymer segments are not only affected by the number and size of the clusters but also by the number of polymer chains associated with clusters.

3.2 Introduction

Polymers that consist of ionic groups tethered to their backbone often associate to form clusters that drive the structure and the dynamics of these macromolecules.¹⁻³ They control over the structure and dynamics of the polymers, impact the mechanical stability as well as ion and water transport characteristics in these materials which in turn, affect their many applications from clean energy to biotechnology. In the low ionic decoration regime, often termed the ionomer regime, (less than ca. 20% decoration),¹ both the electrostatic interactions and the chain conformation affect the properties of the polymers, where the distribution of ionic groups along the backbone affect both. However, the critical impact of the distribution of the ionic groups along the polymer backbone, remains an open question, predominantly since the vast number of studies have been constrained by synthetic routes that often produce a specific distribution. Here using molecular dynamics (MD) simulations, we investigate the effects of the distribution of ionizable groups along the polymer backbone on cluster formation and the interrelation with the structure and dynamics of amorphous polymers.

Driven by synthetic routes, a large number of experimental³⁻⁹ and computational¹⁰⁻¹⁴ studies have focused on polymers with random distribution of ionizable groups. These macromolecules cluster and constrain the dynamics of the chains as shown by Weiss et al.⁶ who showed that a small fraction of ionizable groups on a short polystyrene, below the entanglement length, are sufficient to significantly slow the polymer motion. These clusters often dominate the structure of these melts and are characterized by an inter-aggregate distance signature (ionic peak) in the static scattering factor $S(q)$, where q is the

momentum transfer vector, measured by both small angle X-ray and neutron scattering. The shape of the aggregates is reflected in the line shape of the ionic peak and has been further probed by tunneling electron microscopy (TEM),⁷ where within the resolution of the measurements, a significant number of ionic clusters appear spherical.^{9, 15} Further insight regarding chain conformation is obtained from the scaling of $S(q)$ with q at the chain packing regime.

Recent synthetic efforts were able to tether ionizable groups in a precise distance through Acyclic Diene Metathesis (ADMET) polycondensation, forming relatively short polymers with well-defined distribution of ionizable groups.¹⁶ These polymers exhibit significant differences in their structure and dynamics in comparison with random copolymers, as have been shown by Winey and coworkers for precisely sequenced poly(ethylene-co-acrylic acid) ionomers.⁹ The ionomer peak in these polymers exhibits a well-defined interaggregate correlation compared with randomly spaced materials, as has been shown by X-ray scattering and numerical simulations, with chain packing signatures that are typical to semicrystalline macromolecules.^{9, 14} Computational studies were able to capture the higher intensity and narrower lines of the ionomer signature observed experimentally and provided further insight regarding the dynamics. Studies of the segmental motion by Frischknecht et al.¹⁷ on precise poly(ethylene-co-acrylic acid) ionomers showed that local motion of the chains slows down as clusters are formed in excellent agreement with quasielastic neutron scattering. Hall et al.¹³ studied precise ionomer melts using coarse grained models with explicit counterions and compared with the corresponding random system. They observed that the clusters relax faster than the

polymer for the precise ionomers; however, this is reversed for the random system. The behavior of the precise polymers is typical of semicrystalline polymers.

The structure and transport characteristics of polymers with random and precise distribution of ionizable groups along the polymer backbone are clearly distinctive. The fundamentals that underlie these differences, however, remain unresolved. Using atomistic molecular dynamics (MD) simulations, the current study probes the effects of the distribution of the ionizable groups along the backbone of an amorphous model polymer on the shape and size of the ionic clusters along with the impact on the packing of the ionizable groups within clusters. These are correlated with mesoscopic structure and dynamics of the melts, providing insight into materials designed with desired structure-properties characteristics. Specifically, we investigate ionomer melts of random (R), precise (P), and block (B) polystyrene sulfonate (PSS) fully neutralized with Na^+ counterions. The wealth of knowledge available for PSS is invaluable for focusing on the impact of distribution of the ionizable groups. Despite many ongoing uses of this polymer, the span of technologies is constantly expanding, where the interaction between clustering and properties is a key to their use.¹⁸ Further, PSS remains amorphous and therefore the results provide insight into the inherent effects of ionic group distribution. The correlations between the distribution of the ionizable groups along the polymer backbone, cluster characteristics and adaptation ability of the material as resolved by MD simulations are discussed.

3.3 Model and Simulation Methods

Random, precise, and block PSS molecules of 80 monomers (molecular weight ~8950 g/mol) with 10% sulfonation were constructed using Polymer Builder and Amorphous Cell modules in BIOVIA™ Materials Studio. For the random system, eight sulfonated groups were randomly added to each chain. For the precise system, each chain had one sulfonation group every 10th monomer starting on 5th monomer. Finally, for the block system, 4 sulfonated monomers were placed consecutively every 24th monomer resulting in polymers with two blocks of 4 sulfonated monomers per chain. These systems contained a total of 270, 248 and 280 molecules for random, precise, and block, respectively, with Na⁺ as the counter-ion.

The All-Atom Optimized Potentials for Liquid Simulations (OPLS-AA) force field by Jorgensen et al.^{19, 20} were used to model the system. Additional parameters for the sulfonate groups are given in Refs.²¹⁻²³. The polymers were initially equilibrated using LAMMPS.²⁴ The intermolecular forces were described by Lennard-Jones interactions with an attractive r^{-6} and a repulsive r^{-12} terms and Coulomb interactions. The electrostatic interactions were calculated using particle-particle particle mesh (PPPM) with a real space cutoff of 1.2 nm and precision of 10^{-6} Kcal mol⁻¹ Å⁻¹ for the attractive term of the Lennard-Jones interactions and 5×10^{-4} for the electrostatic interactions. The repulsive (r^{-12}) Lennard-Jones interaction is truncated at 1.2 nm. The reference system propagator algorithm (RESPA)²⁵ with multi-time-scale integrator was used to accelerate the simulation. The time step is 1.0 fs for the bond, angle, dihedral, van der Waals interactions, and direct interactions part of the electrostatic interactions and 4.0 fs for long-range interactions.

Periodic boundary conditions were used in all simulations. LAMMPS data files were converted into GROMACS²⁶⁻²⁸ [structure (.gro) and topology (.top)] because of enhanced efficiency and melts were further equilibrated. Conversion is carried out using a combination of ParmEd and InterMol tools.³²⁹ The electrostatics were treated using the Particle Mesh Ewald (PME)³⁰ algorithm and a Fourier grid spacing of 0.12 nm. All harmonic bonds involving hydrogen atoms were replaced with constraints using the LINCS algorithm.³¹ The temperature is maintained using the Bussi-Parrinello thermostat (V-rescale)³² with a time constant of 0.1 ps. System pressure is maintained at 1 bar using the barostat of Berendsen et al.³³ The simulations were carried out using 2 fs time step. MDAnalysis³⁴ toolkit was used to perform equilibrium analysis.

All three melts were first equilibrated at 600 K at a constant pressure of 1 atm using the Nose-Hoover thermostat and barostat for ~ 5 ns in LAMMPS. The dielectric constant ϵ was then increased to 30 to reduce the residual electrostatic screening between the ionic groups. Increasing ϵ breaks the ionic clusters, allowing the chains to locally equilibrate.¹⁰ The melts were run for 30 ns at constant volume after which the dielectric constant was reset to 1. Each of the systems was then run for 1000 ns in GROMACS at constant volume at density $\rho = 0.94 \text{ g/cm}^3$. This procedure allowed us to follow the formation of the ionic clusters and dynamics of the chains. Ionic clusters were formed over a period of ca. 120-150 ns after ϵ was set to 1. After this period no significant changes were observed in either cluster sizes or their distribution. All results shown here are averaged over the last 850 ns of the run.

3.4 Results

Illustrations of cluster morphologies of SO_3^- assemblies observed in random, precise, and block PSS melts are shown in Figure 3.1. Many of the ionic clusters for R-PSS are elongated, whereas the clusters are more globular in P-PSS melts, with mixed structures of both elongated and globular for the B-PSS. The results for R-PSS are consistent with the elongated clusters observed by MD simulations of Agrawal et al.¹⁰ Note that a rich variety of shapes have been observed for numerous ionomers, however there is no clear driving forces for the different morphologies have been yet established.

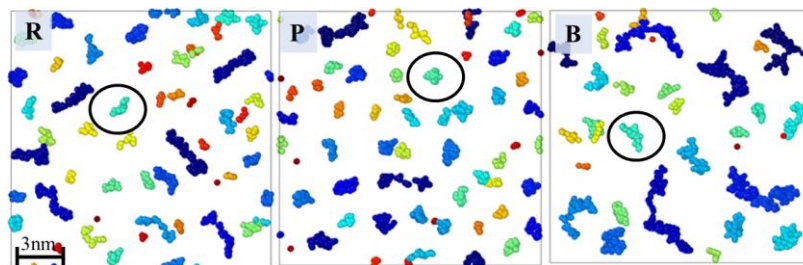


Figure 3.1: Visualization of SO_3^- groups in melts of random (R), precise (P), and block (B) PSS for $f = 0.10$ at 600 K after 1000 ns. Clusters in each system are colored based on number of SO_3^- groups associated (red < orange < yellow < green < teal < blue). For clarity, 1/8 of the systems are shown. Black circled cluster represent the average cluster of SO_3^- groups for each system.

The distribution of the ionizable groups along the backbone affects not only the topology of the clusters but also their size. The ionic cluster size distributions N_{nc} , normalized to total number of chains N , are shown in Figure 3.2 as a function of N_C , the number of sulfur atoms per cluster. Two ionic groups are considered to be in the same cluster if two sulfur atoms are separated by less than 6 \AA , a number dictated by the chemical structure of the sulfonated groups. The average cluster sizes measured are 6.3, 5.8 and 10.1 for the random, precise and block systems, respectively.

The cluster distributions are relatively broad for all three melts with that of B-PSS the broadest. The cluster distribution for the block chains exhibits a much longer tail that shows that larger assemblies are formed.

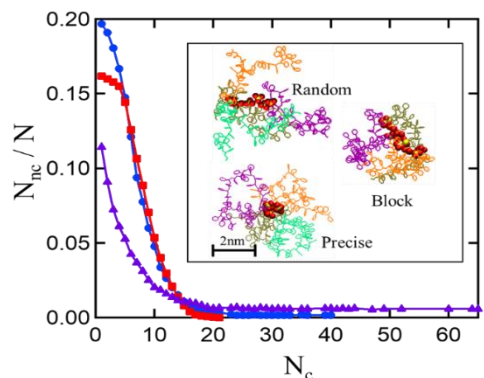


Figure 3.2: Number of clusters N_{nc} , normalized to total number of chains N , as a function of cluster size N_c (number of sulfur atoms), for random (\bullet), precise (\blacksquare), and block (\blacktriangle) PSS melts. Inset shows the snapshots of cluster of SO_3^- groups (enlarged yellow and red spheres are sulfur and oxygen respectively) and associated polymers chains for each system. For clarity, half the length of chains is shown. Different colors in the inset represent distinct chains.

The ionic clusters serve as physical crosslinks in these ionomer melts, and thus affect the structural stability of PSS melts compared to corresponding non-sulfonated PS. The ionic assembly may consist of ionizable groups tethered to different chains (distinct or unique chains) or groups that reside on the same backbone. The number of unique polymer chains N_{uc} associated with each of the clusters together with the size and shape of the clusters govern the overall dynamics of the melts and thus their structural stability.³ Illustrations of unique chains which contribute to an ionic cluster of average size for each of the three systems are shown in the inset of Figure 3.2.

Ionic clusters of average size consist of four unique chains for random and precise systems and three for block system. The fraction of unique chains decreases with increasing cluster size for all three systems as shown in Figure 3.3. At large N_c , the number of unique chains is directly proportional to the cluster size. Significantly fewer unique chains are associated with a given cluster size for the block melts compared to random and precise systems.

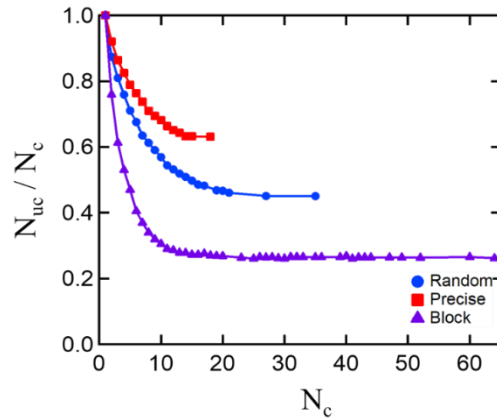


Figure 3.3: Averaged number of unique chains N_{uc} , normalized to cluster size N_c for random, precise, and block PSS melts.

Further insight into the effects of the ionic distribution on the structure of the melts was obtained from the static structure factor $S(q) = |\sum_i b_i e^{i\mathbf{q} \cdot \mathbf{r}_i}|^2 / \sum_i b_i^2$, where \mathbf{q} is the momentum transfer vector, and b_i and \mathbf{r}_i are the scattering length and position vectors of atom i , respectively. Due to the periodic boundary conditions, the wave vectors \mathbf{q} are limited to $\mathbf{q} = \frac{2\pi}{L} (n_x, n_y, n_z)$, where L is the length of the simulation cell and n_x , n_y , and n_z are integers. $S(q)$ was calculated using the scattering length of the elements for neutrons which experimentally have provided in-depth insight into the structure of amorphous

polymers. The scattering lengths b_i for neutrons for each of the elements are listed in Table 3.1.

Table 3.1: Neutron scattering lengths of elements.³⁵

Element	Scattering lengths (10^{-15} m)
H	-3.74
C	6.65
S	2.80
O	5.80
Na	3.63

$S(q)$ as a function of q for the three different melts are shown in Figure 3.4a with the data averaged over the last 850 ns of the run. For high q , which corresponds to shorter intramolecular distances, the distribution of the ionic groups has hardly any effect. The correlation of the ionic clusters is expressed in a peak at low q centered around $q = 0.214 \text{ \AA}^{-1}$, 0.254 \AA^{-1} and 0.123 \AA^{-1} , which corresponds to an average distance between ionic clusters of ~ 29 , 25 , and 51 \AA for random, precise, and block melts, respectively. While the precise and the blocky melts consist of rather similar interaggregate distances, the block co-polymer is characterized by significantly larger dimensions. This low q peak is broader for the random polymer than for the precise and block melts indicating a relatively higher degree of interaggregate correlations even though the polymer is amorphous. Previous X-ray studies of precise polyethylene ionomers^{9, 16} have shown similar trends, though in this case the precise ionomers partially crystallize whereas the random polymer remains amorphous.

To characterize the internal correlations within ionic clusters, we calculated the sulfur-sulfur (S-S) radial distribution function $g(r)$. The results are shown in Figure 3.4b. For all three systems, the first peak at $\sim 4.3 \text{ \AA}$, corresponds to the closest distance between two sulfur atoms in a cluster, whereas the second and third correlation peaks are notably different. The second correlation peak that captures the position of the next neighbor sulfur is rather broad for the random distribution melt and most sharp for the block co-polymer. It is interesting to note that the molecular dimensions captured by $g(r)$ and those of the ionic peak are entirely different. The trend of the second correlation peak in $g(r)$ and the q dependence and intensity pattern of $S(q)$ appear correlated. Higher correlations are more intense for the block co-polymer melt, where significantly more sulfur atoms are tethered in proximity to each other. The pair correlation function shows the clear differences in the packing of the sulfonated groups within the ionic clusters, that appear to propagate to correlations in the nanometer dimensions reflected in $S(q)$.

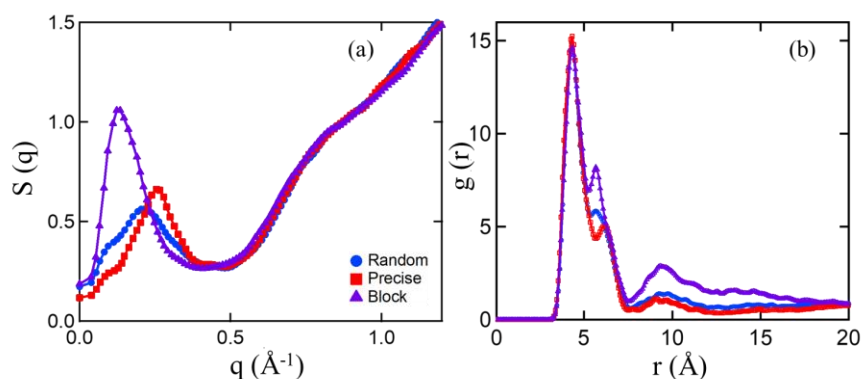


Figure 3.4: (a) $S(q)$ as a function of q , and (b) Sulfur-sulfur radial distribution function for random, precise, and block PSS melts.

Following the observations of correlation between the packing of the sulfur atoms and the ionic peaks for different ionizable group distribution, we set to resolve the effects

on dynamics. Measurements on two different length scales were carried out, the mean square displacement of the molecules and segmental dynamics. The overall mobility of the polymer chains was followed by measuring the mean square displacement, $MSD = \langle [r_i(t) - r_i(0)]^2 \rangle$ of the center of mass (COM) of the chains for the three systems as shown in Figure 3.5a. Even though the polymer does not move their own dimensions over the time of the simulations (1000 ns) due to the presence of the ionic groups which act as physical crosslinks, differences in the local segmental motion are observed between the three melts. For comparison, the mean squared radius of gyration is $\langle Rg^2 \rangle^{1/2} = 4.8$ nm for R-PSS, 5.9 nm P-PSS and 4.0 nm for B-PSS. Interestingly, over the time scale of the measurement, the local mobility of the block chains is higher than for the random and precise systems, although the ionic clusters are larger. The distribution of ionic groups along the polymer chains affects the number of chains that participate in individual clusters as shown in Figure 3.3, altering the nature of the physical crosslinks. For the blocky distribution, the connectivity of the polymer chains across clusters is lower compared to the two other distributions, while for precise and random position of sulfonated phenyl rings along the polymer backbone reduces the local motion of the chains.

Zooming into the internal dynamics of the polymers, we compared the MSD of phenyl groups and sulfonated phenyl rings. As seen in Figure 3.5b, the motion of sulfonated phenyl rings for all distributions is significantly slower than that of the nonsulfonated rings, as previously observed for random PSS melts by Agrawal et al.¹¹ For random and precise melts, about 97.5% of the sulfonated groups reside within assemblies, thus they are more constrained, compared with the non-sulfonated rings. The motion of both sulfonated and

nonsulfonated phenyl rings in the block melts is slightly faster compared to their motion in the random and precise melts almost all of the sulfonated rings confined. In comparison with the local motion of both phenyl rings in the random and precise melt systems, we observe that in the precise melt system the local motion of non-sulfonated rings is slower, whereas the motion of sulfonated rings is slightly higher than that in random melt. MSD is averaged over all sulfonated groups in the melts, therefore, the number of confined S atoms and their internal packing within the clusters affect their motion. While hardly any S atoms reside outside the clusters, their MSD is directly correlated with the overall motion of the center of mass.

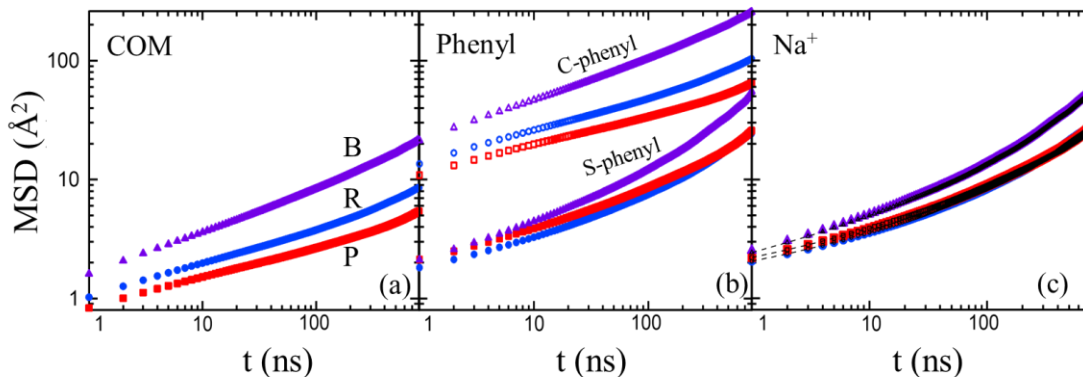


Figure 3.5: Mean square displacement as a function of time for (a) center of mass of chains (b) phenyl rings without sulfonated groups (open symbols) and sulfonated phenyl rings (closed symbols) (c) Na^+ ions (closed symbol) and sulfur (black dash line and symbol) in the ionic group for the random (\bullet), precise (\blacksquare), and block (\blacktriangle) PSS melts.

The relation between the dynamics of ionic species and the corresponding counterions are the critical factors that determine the transport ability of polymers. As seen in Figure 3.5c, the mobility of Na^+ counterions in the block melt is slightly higher than for the random and precise melts, showing similar trends of sulfonated phenyl rings as seen in

Figure 3.5b. Further, Figure 3.5c shows that Na^+ ions are condensed on the ionic groups as they move largely with ionic groups in all three systems.

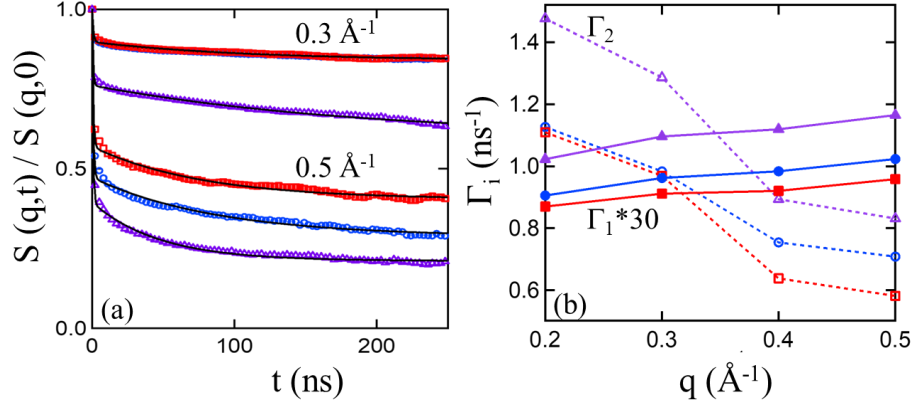


Figure 3.6: (a) $S(q,t)/S(q,0)$ vs time t , for the indicated q values (symbols) and double exponential fit (black solid line), (b) Effective diffusion coefficient Γ_i , as a function of q for the random (\circ), precise (\square), and block (\triangle) PSS melts. Slow (Γ_1) components are represented by solid symbols and lines and fast (Γ_2) components by open symbols and dashed lines.

As segmental dynamics is key to understanding the mesoscopic motion of polymers, the normalized dynamic structure factor $S(q,t)/S(q,0)$ was calculated. Dynamic structure factor $S(q,t) = \frac{1}{N} \sum_{i,j=1}^N b_i b_j \exp [iq \cdot (\mathbf{r}_i(t) - \mathbf{r}_j(0))]$ captures correlated motion of different length scales, depending on q . $S(q,t)$ was calculated using 300 configurations, each separated by 1 ns for the last 300 ns of the run. $S(q,t)$ is calculated for q 's on the order of magnitude of the inter-ionic domain correlations and smaller length scales. Representative $S(q,t)$ curves normalized to $S(q,0)$ are shown in Figure 3.6 for two values of q .

For all q values measured over the entire time span, the relaxation is rather slow except at very early times, where a signature of very fast dynamics, compared to the polymer motion, is observed. At larger length scales, $S(q,t)$ for the precise and random melts practically overlap where the dynamic scattering block melt decays slightly faster. With decreasing dimensions, away from the ionic peak, $S(q,t)$ for the three melts decays slightly faster.

Table 3.2: Slow (Γ_1) and fast (Γ_2) time constants and corresponding pre-exponential factors extracted from double exponential fits for random (R), precise (P) and block.

q (\AA^{-1})	Random				Precise				Block			
	$\Gamma_1(\text{ns}^{-1})$	A_1	$\Gamma_2(\text{ns}^{-1})$	A_2	$\Gamma_1(\text{ns}^{-1})$	A_1	$\Gamma_2(\text{ns}^{-1})$	A_2	$\Gamma_1(\text{ns}^{-1})$	A_1	$\Gamma_2(\text{ns}^{-1})$	A_2
0.2	0.030	0.10	1.13	0.89	0.029	0.10	1.11	0.91	0.034	0.19	1.48	0.81
0.3	0.032	0.12	0.98	0.88	0.030	0.12	0.97	0.88	0.036	0.24	1.29	0.76
0.4	0.033	0.29	0.75	0.71	0.031	0.34	0.64	0.65	0.037	0.27	0.89	0.73
0.5	0.034	0.37	0.71	0.63	0.032	0.43	0.58	0.57	0.039	0.32	0.83	0.67

$S(q,t)$ could not be captured by a single exponential pointing to complex dynamics. With chains being confined by the ionic clusters, a sum of two exponentials $S(q,t) = A_1 e^{-\Gamma_1 t} + A_2 e^{-\Gamma_2 t}$, was used to capture the behavior of $S(q,t)$, where Γ_1 and Γ_2 are effective diffusion coefficients with $\Gamma_1 < \Gamma_2$, and A_1 and A_2 ($A_1 + A_2 = 1$) are weight constants that provide the relative contributions of each of the dynamic processes to the overall dynamics. The fits are shown as a solid line in Figure 3.6a for all three PSS melts, and the corresponding effective diffusion coefficients are shown in Figure 3.6b. The values for slow and fast time constants and corresponding pre-exponential factors are given in Table 2.

The slowest effective diffusion Γ_1 slightly increases with increasing q , in agreement with $S(q,t)$ previous results by Agrawal et al.¹⁰ for random melts. This is consistent with the ionic clusters acting as physical crosslinkers and inhibiting relaxation of the chains locally. A crossover region is observed for the faster relaxation times Γ_2 corresponding to the length scales of ~ 16 Å. This dimension is in the order of magnitude of the Kuhn length of PS and attributed to the confinement region, where the chain dynamics are strongly affected by the chains being tethered to an ionic cluster.^{10, 36, 37} Both random and precise systems show almost similar magnitudes of dynamics and trends, with the block system exhibiting slightly faster dynamics compared to the random and precise systems.

3.5 Conclusions

Here the structure and dynamics of PSS melts were studied as the distribution of ionizable groups along the polymer backbone was varied. The shape of the clusters and their size as well as internal packing of the sulfur groups within the clusters were followed and correlated with the structure as extracted by $S(q)$ and dynamics as reflected in MSD and $S(q,t)$. Though the effects observed appear small, particularly since the polymer is confined by the ionic clusters, the studies have provided new insight into the length scale of confinement, and the correlation of cluster features and the macroscopic dynamics in such melts. We find that the distribution of sulfonated groups along the polymer chain backbone affects the shape, size, and packing of the ionizable groups within the cluster, and in turn affects the mesoscopic properties. Random PSS melts consist of predominantly

elongated clusters, whereas the clusters are more globular in precise PSS melts. A mix of both elongated and globular clusters coexist in block melts. The cluster size distribution for all melts is relatively broad, with the block melts comprised of larger clusters compared to random and precise. Further, the internal packing of the sulfonated groups within the ionic clusters as reflected in the pair correlation function is affected by the distribution of the ionic groups along the polymer backbone, such controlling the cohesion of the clusters. These differences in the packing of the sulfonated groups within the ionic clusters appear to propagate to correlations in the nanometer dimensions reflected in $S(q)$. As expected for all melts, the polymer motion is constrained on multiple length scales. However, fast and slow dynamic processes are detected by $S(q,t)$ that are attributed directly to cluster-confined segments and those that reside further away.

The local mobility of the block chains is higher than the random and precise, even though the ionic clusters are larger. It brings to light an intriguing insight regarding the dynamics of the polymers, where the number of unique chains associated with one cluster is directly correlated with the dynamics of the polymers. With fewer unique chains associated with a given cluster size for the block melts compared to other systems, results in faster dynamics. Finally, the Na^+ ions are condensed on the ionic groups as they move largely with ionic groups in all three systems however, counter dynamics in the block melt is slightly higher than the random and precise melts. The new insight into the correlations of ionizable group distributions along amorphous polymer backbone provides an opening for design of polymers whose clustering characteristics are controlled, affecting their potential applications.

3.6 Acknowledgements

D.P. gratefully acknowledges NSF Grant No. DMR-1611136 and DOE Grant No. DE-SC007908. The authors kindly acknowledge the use of computational resources provided by NSF MRI-1725573. This work was made possible in part by advanced computational resources deployed and maintained by Clemson Computing and Information Technology. This research used resources at the National Energy Research Scientific Computing Center (NERSC), a U.S. Department of Energy Office of Science User Facility operated under Contract No. DE-AC02-05CH11231. This work was performed, in part, at the Center for Integrated Nanotechnologies, a U.S. Department of Energy and Office of Basic Energy Sciences user facility. Sandia National Laboratories is a multimission laboratory managed and operated by National Technology and Engineering Solutions of Sandia LLC, a wholly owned subsidiary of Honeywell International Inc., for the U.S. Department of Energy's National Nuclear Security Administration under Contract DE-NA0003525. The views expressed in this article do not necessarily represent the views of the U.S. DOE or the United States Government.

3.7 References

- (1) Eisenberg, A.; Kim, J.-S. *Introduction to ionomers*; Wiley, New York,, 1998.
- (2) Eisenberg, A. Clustering of ions in organic polymers. A theoretical approach. *Macromolecules* **1970**, *3*, 147-154.
- (3) Eisenberg, A.; Hird, B.; Moore, R. A new multiplet-cluster model for the morphology of random ionomers. *Macromolecules* **1990**, *23*, 4098-4107.

- (4) Kirkmeyer, B. P.; Weiss, R. A.; Winey, K. I. Spherical and vesicular ionic aggregates in Zn-neutralized sulfonated polystyrene ionomers. *J. Polym. Sci. B Polym. Phys.* **2001**, *39*, 477-483.
- (5) Peiffer, D.; Weiss, R.; Lundberg, R. Microphase separation in sulfonated polystyrene ionomers. *J. Polym. Sci. : Polym. Phys.* **1982**, *20*, 1503-1509.
- (6) Weiss, R.; Zhao, H. Rheological behavior of oligomeric ionomers. *J. Rheol.* **2009**, *53*, 191-213.
- (7) Zhou, N. C.; Chan, C. D.; Winey, K. I. Reconciling STEM and X-ray scattering data to determine the nanoscale ionic aggregate morphology in sulfonated polystyrene ionomers. *Macromolecules* **2008**, *41*, 6134-6140.
- (8) Moore, R. B.; Bittencourt, D.; Gauthier, M.; Williams, C. E.; Eisenberg, A. Small-angle x-ray scattering investigations of ionomers with variable-length side chains. *Macromolecules* **1991**, *24*, 1376-1382.
- (9) Seitz, M. E.; Chan, C. D.; Opper, K. L.; Baughman, T. W.; Wagener, K. B.; Winey, K. I. Nanoscale morphology in precisely sequenced poly (ethylene-co-acrylic acid) zinc ionomers. *J. Am. Chem. Soc.* **2010**, *132*, 8165-8174.
- (10) Agrawal, A.; Perahia, D.; Grest, G. S. Cluster morphology-polymer dynamics correlations in sulfonated polystyrene melts: computational study. *Phys. Rev. Lett.* **2016**, *116*, 158001.
- (11) Agrawal, A.; Perahia, D.; Grest, G. S. Clustering effects in ionic polymers: Molecular dynamics simulations. *Phys. Rev. E* **2015**, *92*, 022601.

- (12) Ma, B.; Nguyen, T. D.; Pryamitsyn, V. A.; Olvera de la Cruz, M. Ionic correlations in random ionomers. *ACS nano* **2018**, *12*, 2311-2318.
- (13) Hall, L. M.; Stevens, M. J.; Frischknecht, A. L. Dynamics of model ionomer melts of various architectures. *Macromolecules* **2012**, *45*, 8097-8108.
- (14) Hall, L. M.; Seitz, M. E.; Winey, K. I.; Opper, K. L.; Wagener, K. B.; Stevens, M. J.; Frischknecht, A. L. Ionic aggregate structure in ionomer melts: effect of molecular architecture on aggregates and the ionomer peak. *J. Am. Chem. Soc.* **2012**, *134*, 574-587.
- (15) Register, R. A. Morphology and Structure–Property Relationships in Random Ionomers: Two Foundational Articles from *Macromolecules*. *Macromolecules*: 2020; Vol. 53, pp 1523–1526.
- (16) Baughman, T. W.; Chan, C. D.; Winey, K. I.; Wagener, K. B. Synthesis and morphology of well-defined poly (ethylene-co-acrylic acid) copolymers. *Macromolecules* **2007**, *40*, 6564-6571.
- (17) Frischknecht, A. L.; Paren, B. A.; Middleton, L. R.; Koski, J. P.; Tarver, J. D.; Tyagi, M.; Soles, C. L.; Winey, K. I. Chain and ion dynamics in precise polyethylene ionomers. *Macromolecules* **2019**, *52*, 7939-7950.
- (18) Labriola, L.; Jadoul, M. Sodium polystyrene sulfonate: still news after 60 years on the market. Oxford University Press: 2020.
- (19) Jorgensen, W. L.; Maxwell, D. S.; Tirado-Rives, J. Development and testing of the OPLS all-atom force field on conformational energetics and properties of organic liquids. *J. Am. Chem. Soc.* **1996**, *118*, 11225-11236.

- (20) Jorgensen, W. L.; Madura, J. D.; Swenson, C. J. Optimized intermolecular potential functions for liquid hydrocarbons. *J. Am. Chem. Soc.* **1984**, *106*, 6638-6646.
- (21) He, X.; Guvench, O.; MacKerell Jr, A. D.; Klein, M. L. Atomistic simulation study of linear alkylbenzene sulfonates at the water/air interface. *J. Phys. Chem. B* **2010**, *114*, 9787-9794.
- (22) Cannon, W. R.; Pettitt, B. M.; McCammon, J. A. Sulfate anion in water: model structural, thermodynamic, and dynamic properties. *J. Phys. Chem.* **1994**, *98*, 6225-6230.
- (23) Chandrasekhar, J.; Spellmeyer, D. C.; Jorgensen, W. L. Energy component analysis for dilute aqueous solutions of lithium (1+), sodium (1+), fluoride (1-), and chloride (1-) ions. *J. Am. Chem. Soc.* **1984**, *106*, 903-910.
- (24) Plimpton, S. Fast parallel algorithms for short-range molecular dynamics. *J. Comput. Phys.* **1995**, *117*, 1-19.
- (25) Tuckerman, M.; Berne, B. J.; Martyna, G. J. Reversible multiple time scale molecular dynamics. *J. Chem. Phys.* **1992**, *97*, 1990-2001.
- (26) Pronk, S.; Páll, S.; Schulz, R.; Larsson, P.; Bjelkmar, P.; Apostolov, R.; Shirts, M. R.; Smith, J. C.; Kasson, P. M.; Van Der Spoel, D. GROMACS 4.5: a high-throughput and highly parallel open source molecular simulation toolkit. *Bioinformatics* **2013**, *29*, 845-854.
- (27) Abraham, M. J.; Murtola, T.; Schulz, R.; Páll, S.; Smith, J. C.; Hess, B.; Lindahl, E. GROMACS: High performance molecular simulations through multi-level parallelism from laptops to supercomputers. *SoftwareX* **2015**, *1*, 19-25.

- (28) Berendsen, H. J.; van der Spoel, D.; van Drunen, R. GROMACS: a message-passing parallel molecular dynamics implementation. *Computer physics communications* **1995**, *91*, 43-56.
- (29) Shirts, M. R.; Klein, C.; Swails, J. M.; Yin, J.; Gilson, M. K.; Mobley, D. L.; Case, D. A.; Zhong, E. D. Lessons learned from comparing molecular dynamics engines on the SAMPL5 dataset. *J. Comput. Aided Mol. Des.* **2017**, *31*, 147-161.
- (30) Essmann, U.; Perera, L.; Berkowitz, M. L.; Darden, T.; Lee, H.; Pedersen, L. G. A smooth particle mesh Ewald method. *J. Chem. Phys.* **1995**, *103*, 8577-8593.
- (31) Hess, B.; Bekker, H.; Berendsen, H. J.; Fraaije, J. G. LINCS: a linear constraint solver for molecular simulations. *J. Comput. Chem.* **1997**, *18*, 1463-1472.
- (32) Bussi, G.; Donadio, D.; Parrinello, M. Canonical sampling through velocity rescaling. *J. Chem. Phys.* **2007**, *126*, 014101.
- (33) Berendsen, H. J.; Postma, J. v.; van Gunsteren, W. F.; DiNola, A.; Haak, J. R. Molecular dynamics with coupling to an external bath. *J. Chem. Phys.* **1984**, *81*, 3684-3690.
- (34) Michaud-Agrawal, N.; Denning, E. J.; Woolf, T. B.; Beckstein, O. MDAAnalysis: a toolkit for the analysis of molecular dynamics simulations. *J. Comput. Chem.* **2011**, *32*, 2319-2327.
- (35) Sears, V. F. Neutron scattering lengths and cross sections. *Neutron news* **1992**, *3*, 26-37.

- (36) Kanaya, T.; Kaji, K.; Kitamaru, R.; Higgins, J. S.; Farago, B. Dynamics of polyelectrolyte solutions by neutron spin echo: molecular weight dependence. *Macromolecules* **1989**, *22*, 1356-1359.
- (37) Nyström, B.; Roots, J.; Higgins, J.; Gabrys, B.; Peiffer, D.; Mezei, F.; Sarkissian, B. Dynamics of polystyrene sulfonate ionomers in solution. A neutron spin-echo study. *J. Polym. Sci., Part C: Polym. Lett.* **1986**, *24*, 273-281.

CHAPTER FOUR

NONLINEAR ELONGATION FLOWS IN ASSOCIATING POLYMER MELTS: FROM HOMOGENEOUS TO HETEROGENEOUS FLOW

4.1 Abstract

Response to elongational flow is fundamental to soft matter and directly impacts new developments in a broad range of technologies in polymer processing, microfluidics to controlled flow in biosystems. Of particular significance are the effects of elongational flow on self-assembled systems where the interactions between the fundamental building blocks control their adaptation. Here we probe the effects of associating groups on the structure and dynamics of linear polymer melts in uniaxial elongation using molecular dynamics simulations. We study model polymers with randomly incorporated backbone associations with interaction strengths varying from 1-10 $k_B T$. These associating groups drive the formation of clusters in equilibrium with an average size that increases with interaction strength. Flow drives these clusters to continuously break and reform as chains stretch. These flow-driven cluster dynamics drive a qualitative transition in polymer elongation dynamics from homogenous to nanoscale localized yield and cavitation as the association strength increases.

4.2 Introduction

Response to elongational forces is fundamental to what makes soft matter soft, and it encapsulates a broad range of phenomena. Dense complex fluids, from slurries and colloids to blood flow, and industrially processed polymers, either form or function under elongational flow.¹⁻³ The shape, the dimensions, and the adaptability of the building blocks of these complex fluids determine their structure and dynamics during elongation. Polymer melts constitute one such dense system with immense technological significance⁴⁻⁶ that are routinely processed under elongational flow. Many of these macromolecules contain associating groups that are critical for their technological function and at the same time drive unique rheological behavior. While the challenges in processing of associative polymers have been long realized,⁷⁻¹¹ little is known about the response of these complex fluids to uniaxial elongational flow. Here, using molecular dynamics simulations, we show that the heterogeneous breakup of the associative clusters under flow drive dynamic heterogeneity of chains and nanostructured flow patterns that could impact the processing of complex fluids. Under strong flow the associative clusters rapidly break up and reform. We show that the highest flow rates, the cluster size distribution becomes independent of the strength of the associating groups as the flow becomes so strong that it overpowers the associative interactions, resulting in a convergence of the terminal viscosity at high flow rate.

Formation of associative polymer complexes are driven by a variety of molecular interactions including hydrogen bonding, π - π interactions, metal-ligand coordination, and long-lived ionic interactions.^{12,13} These mechanisms can differ substantially in the

coordination and cohesive strength of their associations. Hydrogen bonding and π - π interactions are governed by short range interactions with strengths of association that depend on the polarizability and steric interactions of the associating groups. In contrast, ionizable associating groups exhibit long range forces and thus result in large clusters with complex nanostructures that control the structure, dynamics, and rheological response of ionic polymers.¹⁴ However, the impact of the interaction strength of the associating groups influences the structure of the clusters under elongational flow and their resulting impact on the overall flow response remains unknown.

The technological impact of elongational flow on complex fluids formed by polymers have motivated a number of experimental and computational studies. For non-associating systems, several recent experimental efforts have probed the structure and rheology of entangled^{10, 11, 15, 16} and unentangled¹⁶⁻¹⁸ homopolymer melts and solutions in extensional flows where the degree of entanglement controls their viscoelastic response. These studies have observed that strong extensional flows significantly elongate polymer chains as expected, but generate distinct trends in nonlinear viscosities that vary with elongation rate, molecular weight N , entanglement segment length N_e ,^{19, 20} dilution ϕ ²¹,²² and proximity to the glass transition temperature T_g .²³

Molecular dynamics simulations have been able to relate some of these trends in nonlinear rheology to changes in viscous dissipation as chains become highly elongated in melts and solutions.²⁴⁻²⁷ O'Connor et al.^{24, 25} recently showed that the rate-dependence of the extensional viscosity of homopolymer melts changes with molecular weight N due to a cross-over in dissipation mechanism as elongation rates increase. At low rates, the

dissipation is dominated by diffusive relaxation of chain conformations, whereas at high rates the dissipation is dominated by the advective drag of the flow field on the elongated chains. Polymer solutions also exhibit a sharp distinction between their *equilibrium* modes of dissipation and their *nonequilibrium* dissipation in elongated states. Recent theoretical models were successful in predicting the rate-dependent viscosity of elongated systems observed in experiments. These models promote tube model parameters like the monomeric friction and entanglement density to dynamic variables that can evolve as functions of the nonequilibrium chain order.^{26, 28-31}

Less is known for associating systems in nonlinear elongation. For ionic polymers, Shabbir et al.^{15, 16} and Wu et al.¹⁸ reported that increasing the strength of the associating groups increases the elastic modulus and decreases processability. These authors showed that extension rates faster than the reciprocal of the associating group lifetime led to brittle failure and extension rates slower than the reciprocal of the associating group lifetime lead to continuous stretching that nearly reaches steady state at the highest Hencky strain of order 5. Hinton et al.^{10, 11} demonstrated that weakening the strength of the association from that of ionic interactions to hydrogen bonding further decreased the elastic modulus and only moderately increases processability. Recently, Schafer et al.³² developed theories that predict that the intermolecular reversible crosslinks in silk proteins can shift the alignment-to-stretch transition of semi-dilute polymers to much smaller strain rates. Schafer and McLeish³³ also found that intermolecular associations in silk can also reduce the critical specific work for flow-induced crystallization.

Here, we employ molecular simulations to study the structural evolution and rheological behavior of associating polymer melts under elongation flow. The complexity of the system is reduced by using a coarse-grained bead-spring model in which the association groups are incorporated in the form of beads with stronger cohesive attraction. These “sticky beads” are randomly distributed along the chain backbone.³⁴ The strength of the interaction between associating groups is varied from 1 to $10k_B T$. The lower end of this range is characteristic of the interaction energies that drive co-polymer assembly. With increasing interaction strength, the model captures the association of polar groups, such as those present in non-ionic surfactants, and our largest interactions approach ionic interaction strengths. This range is sufficient to produce qualitative changes in both the equilibrium cluster structure and nonlinear flow behavior of our associating melts, as illustrated in Figure 4.1.

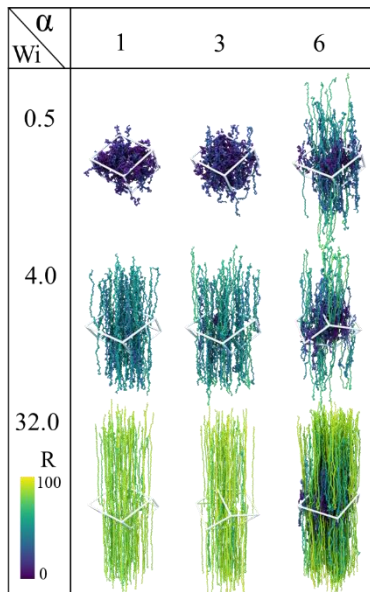


Figure 4.1: Snapshots illustrating chain stretching for associating group strength $\alpha = 1, 3$ and 6 for $Wi = 0.5, 4$ and 32 at strain $\varepsilon = 10$. For clarity, $1/4$ of systems are shown. Chains are colored according to their end-to-end distance R .

4.3 Model and Simulation Methods

Polymers are modeled with a fully flexible bead-spring model.³⁵ A homopolymer melt with no associating groups of 500 linear chains of length $N = 100$ beads of mass m and diameter σ were first constructed following the procedure of Auhl et al.³⁶ The beads are connected with finitely extensible (FENE) springs. The beads interact with a Lennard-Jones potential with a length-scale σ , cutoff $r_{\text{cut}} = 2.5\sigma$, and energy scale $\varepsilon_{\alpha\beta}$. The indices $\alpha\beta$ are either 1 or 2 and indicate bead type. We include associativity by using two types of beads. Non-associating beads are type 1 and interact with and LJ cohesion strength ε_{11} . After the homopolymer melt is equilibrated, we randomly select five beads on each chain to be associating beads of type 2. The cohesion between associating groups is modeled by setting the LJ interaction strength $\varepsilon_{22} \geq \varepsilon_{11}$. The cross term is set to $\varepsilon_{12} = \varepsilon_{11}$ so that only pairs of associating beads experience excess cohesion. Each system is then run for $10^7 \tau$, where $\tau = \sigma (m/\varepsilon_{11})^{1/2}$, until the average cluster size of the associating groups no longer changes.³⁴ All simulated melts are maintained at a temperature $T = \varepsilon_{11}/k_B$, which is $\sim 2T_g$ ³⁷ and we vary the dimensionless ratio $\alpha = \varepsilon_{22}/\varepsilon_{11}$ from 1 to 10 such that interaction energy between associating beads ranges from $1 - 10 k_B T$.

The equations of motion are integrated with a time step $\Delta t = 0.01\tau$ at temperature $T = \varepsilon_{11}/k_B$ with a thermostat damping time of 10τ and density $\rho \approx 0.89\sigma^{-3}$. To model uniaxial extensional flow, melts are elongated along the z -axis of the simulation box at a constant Hencky strain rate $\dot{\varepsilon} \equiv \partial\Lambda/\partial t$, where Λ is the stretch ratio along the z -axis. Since polymers are nearly incompressible, the two perpendicular directions both contract as $\Lambda^{-1/2}$. Flow is maintained by integrating the g-SLLOD equations of motion³⁸ with a Nosé-

Hoover thermostat. The simulation box is regularly remapped during flow with generalized Kraynik-Reinelt (GKR) boundary conditions to prevent the simulation cell from becoming too skewed.^{39, 40} During flow, we measure the extensional stress $\sigma_E = \sigma_{zz} - 0.5(\sigma_{xx} + \sigma_{yy})$ and the transient extensional viscosity (stress-growth coefficient) $\eta_E^+(\varepsilon) = \sigma_E/\dot{\varepsilon}$.

Unlike experiments, simulations with periodic boundary conditions can maintain uniaxial elongation flows of bulk-fluids to arbitrarily large strains. This allows us to maintain flows well past experimental limits and accumulate sufficient statistics to resolve distributions for ε cluster sizes and chain conformations over large strains. The stress reaches a time-independent plateau after a true strain of $\varepsilon = 4$ as shown in Figure 4.2a. The results reported here are obtained by averaging simulation data over a strain interval $\varepsilon = 5 - 10$, which we refer to as steady state. In this regime all measured quantities such as the average end-to-end distance $\langle R \rangle$ of the chains and cluster distribution do not change. Over this range of strain, the stress fluctuates (due to finite size effects) about a well-defined average value. In this regime we denote the average steady-state viscosity by η_E to distinguish from the early time transient viscosity $\eta_E^+(\varepsilon)$. We note that this interval is given in true strain such that the range of $\varepsilon = 5-10$ corresponds to stretch ratios λ from $\sim 150-21000$. This interval, enabled by periodic simulations, is much larger than can be assessed by experiments and thus provides the first microscopic insight into the steady state extensional flow of associating polymers.

The strength of flow is measured in terms of a dimensionless Weissenberg number $Wi = \dot{\varepsilon}\tau_R$, where $\tau_R = \tau_e Z^2$ is the Rouse time⁴¹ for chains in a melt with no associating groups

($\alpha = 1$). The Rouse time is the longest dissipative relaxation time for a linear chain in the absence of entanglements, τ_e is the entanglement time and $Z = N/N_e$ is the number of entanglements per chain and N_e is the entanglement length. By measuring the strength of the flow in terms of Wi and degree of entanglements in terms of Z , allows a direct comparison with experimental result. Previous work on linear²⁴, ring⁴² and ring-linear blends⁴³ show excellent agreement between the experimentally observed extensional viscosity and simulation results using the model studied here. For the fully flexible model used here, $N_e \sim 84$ ^{44,45}, $\tau_e = 10^4 \tau$ ⁴⁶, and we vary Wi from 0.1 to 32. All simulations were run using the Large Scale Atomic Molecular Massively Parallel Simulator (LAMMPS)⁴⁷ software.

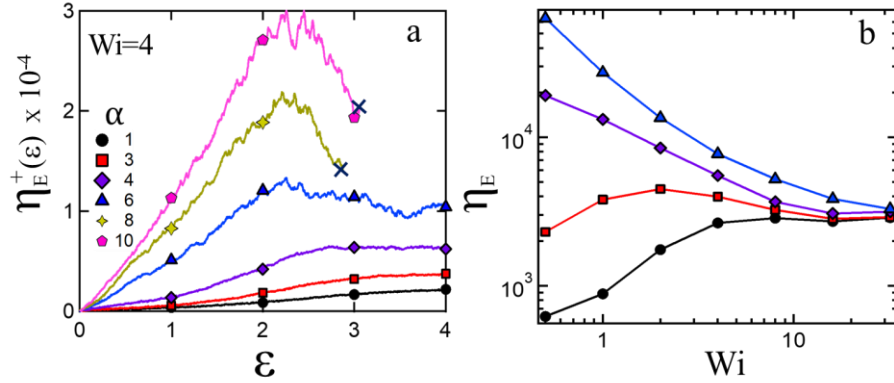


Figure 4.2: (a) Transient extensional viscosity $\eta_E^+(\varepsilon)$ as a function of Hencky strain ε for association strengths $\alpha = 1, 3, 4, 6, 8,$ and 10 at a $Wi = 4$. A cross indicates the strain at which cavities are observed for $\alpha = 8$ and 10 . (b) Terminal viscosities computed by averaging η_E over the strain interval from 5 to 10 versus Wi for $\alpha = 1, 3, 4$ and 6 .

4.4 Results

The startup extensional viscosities $\eta_E^+(\epsilon)$ versus ϵ for $Wi = 4$ for melts with interaction ratio α varying from 1-10 are plotted in Figure 4.2a. As α increases, our simulations capture the experimentally¹⁰ observed transition from steady flow to solid-like yield and failure. For $\epsilon_s \leq 4$, $\eta_E^+(\epsilon)$ increases monotonically until approaching a plateau at large strain. For $\alpha = 6$, the startup viscosity increases non-monotonically, exhibiting an overshoot around strain $\epsilon \sim 2$ and reaches a steady-state by $\epsilon \sim 4$. As illustrated in Figure 4.1, this change in behavior is associated with the heterogenous breakup and flow of the system. For $\alpha \geq 8$, the stress maximum becomes more pronounced and is followed by a sudden drop in stress due to rapid strain localization and cavity formation. These cavitation events, shown in Figure 4.3, are probably precursors to the runaway strain localization and macroscopic failure observed in filament stretching experiments.¹⁰

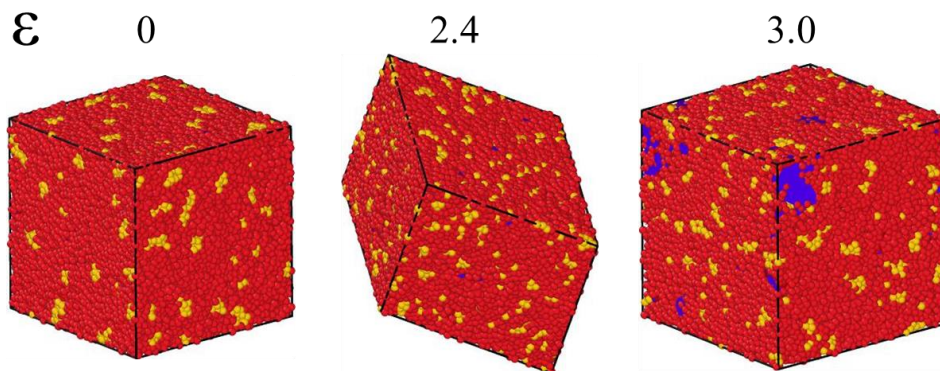


Figure 4.3: Snapshots of systems with interaction ratio $\alpha=10$ with cavities for $Wi=4$ at strain $\epsilon = 0, 2.4$ (maximum stress) and $\epsilon = 3.0$. Non-associating beads, stickers and cavities are visualized by red, yellow, and blue colors, respectively.

The transition to solid-like yield, as the interaction ratio α increases, produces a massive rise in the terminal extensional viscosity, as shown in Figure 4.2b for ε_s from 1-6 and Wi from 0.5-32. At $Wi = 0.5$, η_E increases by two orders of magnitude as ε_s increases from 1 to 6. Considering that only 5% of monomers are driving this large change in macroscopic dissipation, it is no wonder that these materials are so challenging to formulate and process. Interestingly, while all systems differ dramatically in their dissipation at low Wi , they all approach a similar plateau in viscosity at high rates, $Wi > 10$. This convergence appears to be due to fragmentation of the clusters in sufficiently strong flows. In equilibrium, the average size of clusters increases significantly with increasing interaction ratio α ,³⁴ but we will show that strong extensional flow breaks up these clusters into smaller fragments. In non-associating homopolymers, stress growth and steady-state dissipation are controlled by chain conformations elongating within the entanglement network. However, for these strongly associating systems, polymer elongation is instead mediated - or locally hindered - by chains coupling to a transient network of associating clusters. This produces enhanced strain hardening at all elongation rates, as shown in Figure 4.4(a) which compares the stress – strain curves of $\alpha = 1$ and 6 systems for Wi from 0.5-32. Associating melts show large and roughly linear growth in stress with strain at all rates, while non-associating melts exhibit much lower initial slopes and delayed strain hardening that only becomes appreciable above strains ~ 2 .

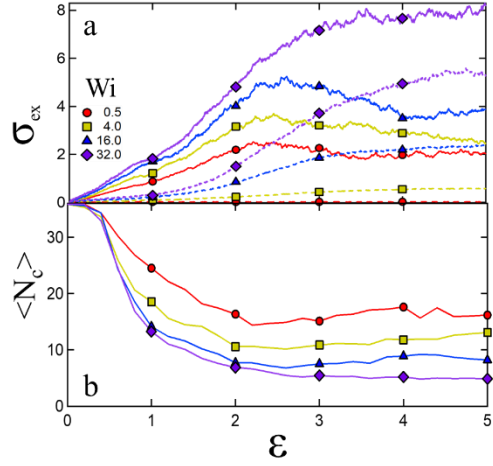


Figure 4.4: (a) Extensional stress σ_{ex} for interaction ratio $\alpha = 1$ (dash lines) and 6 (solid lines) and (b) average cluster size $\langle N_c \rangle$ as a function of strain ϵ for $\alpha = 6$ and $Wi = 0.5, 4, 16,$ and 32 .

The large stresses produced by elongating the chains drive the breakup of larger clusters of associating beads, reducing the average cluster size as shown in Figure 4.4(b). A cluster's size is defined by the number of associating beads within 1.5σ of another member of the cluster. Similar results are obtained for cutoff distances of 1.4 and 1.6σ . The average cluster size decreases gradually with increasing extensional stress and reaches a constant value for strains $\epsilon \sim 3$. This cluster fragmentation process alters the temporary network and the coupling of chain conformations to the macroscopic flow, which can produce the heterogenous behavior seen in Figure 4.1.

The probabilities $P(N_c)$ of associating clusters of sizes N_c for $\alpha = 2 - 6$ are shown in Figure 4.5 for equilibrium and for $Wi = 1$ and 8 . The average $\langle N_c \rangle$ for all systems and Wi are shown in the inset of Figure 4.4(c). In equilibrium, both $P(N_c)$ and the average cluster size N_c change significantly and qualitatively as the strength of the associating groups increases from $\alpha = 2$ to 6 . At $\alpha = 2$, the most common cluster size is ~ 1 bead

with a tail extending to larger sizes. As strength increases, $P(N_c)$ develops a well-defined peak of larger clusters. However, these differences diminish with increasing Wi as the flow breaks up larger clusters into smaller ones, producing distributions at low N_c that converge toward a common curve. Notably, for $\alpha = 6$, the system has no small clusters ($N_c < 10$) in equilibrium, but by $Wi = 8$, the flow-induced fragmentation process generates a distribution of small clusters that is qualitatively like the distributions of systems with weaker associations. At the highest Wi , $P(N_c)$ becomes independent of α as the flow becomes so strong that it overpowers the associative interactions. This coincides with the high-rate convergence of the terminal viscosity (Figure 4.2b). In this regime, advection drives the clusters to form and dissolve so rapidly that the viscosity becomes independent of the strength of the associating groups.

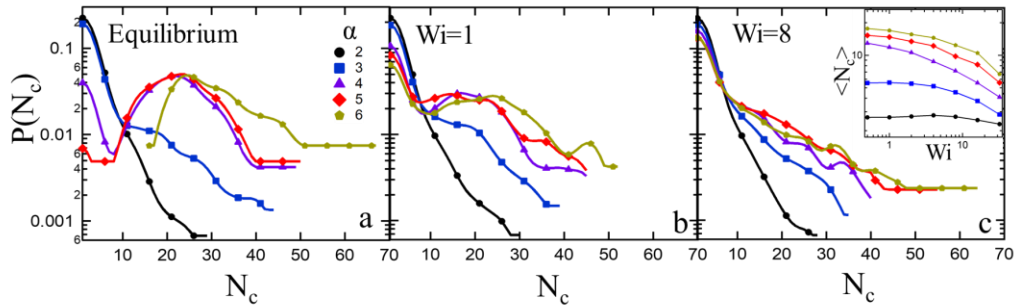


Figure 4.5: Probability $P(N_c)$ as a function of cluster size N_c for interaction ratio $\alpha = 2 - 6$, (a) at equilibrium (b) for $Wi = 1$ and (c) $Wi = 8$. Inset shows the average cluster size $\langle N_c \rangle$ as a function of Wi for corresponding systems.

To capture these kinetics, the average contact lifetime of two associating beads was determined by measuring the time two associating group remain continuously in contact. Here, two beads are in contact if separated by a distance less than 1.5σ . In equilibrium,

for $\alpha > 3$ the average contact lifetime is immeasurably large (larger than the simulation time). However, under flow, the average lifetimes are significantly reduced as most associating groups stay in contact for very short times, less than 0.5τ , before separating. This indicates that cluster fragmentation is dominated by advection, especially as cluster strengths increase. Interestingly, while fragmentation depends on mean cluster sizes, we find that the distribution of pair-wise contact lifetimes becomes independent of Wi for large Wi .

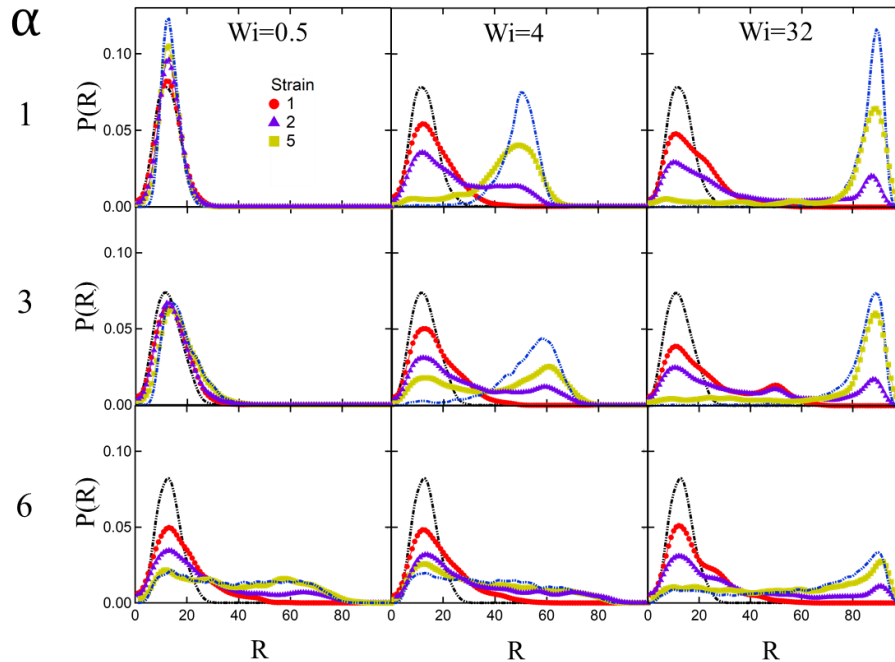


Figure 4.6: Distribution function $P(R)$ of the end-to-end distance R for $\alpha = 1, 3$ and 6 for $Wi=0.5, 4$ and 32 for strain $\varepsilon = 1, 2$ and 5 . Black and blue dot-dashed lines corresponding to $P(R)$ for equilibrium and average over strain interval 5-10, respectively.

The heterogeneous breakup of clusters drives a dynamic heterogeneity in the elongation of individual polymer chains. Figure 4.6 shows the probability distributions

$P(R)$ of the end-to-end distances R of chains at several strains for $Wi = 0.5, 4$ and 32 . For the non-associating system ($\alpha = 1$), a narrow distribution at small R in equilibrium transitions to a narrow distribution at a large R by moving through a transient broad distribution. This intermediate broadening occurs because the susceptibility of individual chains to align in the flows depends upon their initial orientation and conformation, but eventually all the chains become elongated to a degree that increases with increasing Wi ²⁴, ²⁵. For strongly interacting associating groups ($\alpha = 6$), a fraction of chains stretch out, broadening the distribution, while other chains resist alignment because they are trapped within unyielding associating complexes. This produces a broad bimodal $P(R)$ as strain localizes and is accommodated by some chains that have been pulled taut enough to break free of anchoring points within large clusters.

The heterogeneous elongation of chains produces a self-reinforcing feed-back with the cluster dynamics. As chains elongate toward full extension, they must maintain their backbone contour length, which inhibits the advection of larger clusters. This tends to reduce the size of clusters that elongated chains can participate in, which makes them even easier to elongate, further amplifying the effect. This feedback produces cross-correlations in $P(R)$ and $P(N_c)$. These results highlight that chain and cluster dynamics are highly correlated during nonlinear flow, and that these correlations can produce large changes in nanoscale structure and dynamics that can be used to engineer the nanoscale response of associating polymers to macroscopic deformations.

4.5 Conclusions

Our simulations have identified how a small fraction of associating groups along polymer backbones can dramatically alter the structure, dynamics, and deformation behavior of unentangled polymer melts. Increasing the association strength dramatically enhances both the extensional viscosity and strain hardening until systems eventually develop a yield-like overshoot and fail by cavitation. For intermediate interaction strengths $\sim 3 - 6 k_B T$ and low rates, systems flow with an additional dissipation due to the work of breaking associations. As rates increase, chains develop a bimodal, stretching dynamics due to the heterogeneous breakup of associating clusters that localizes elongation in a fraction of the chains. Elongated chains hinder cluster convection and rapidly pull out of larger clusters, which makes it easier for them to elongate further.

In the limit of high strain rates, the viscous dissipation of all systems converges toward a common value independent of association strength α and strain rate. This appears to be due to the correlated dynamics of chain elongation and clusters fragmentation driving the cluster-size distribution $P(N_c)$ toward a system-independent distribution in strong flow.

Our results suggest that its unlikely experiments can get to a strain interval where there is a robust steady-state as the dynamics are too slow relatively to the strain limitations of experiments. However, these distributions can still be useful tools for understanding these highly correlated dynamics in transient flows. The approach of all systems towards a common limiting distribution at high-rates provides a useful waypoint for rationalizing processing trends and constructing new theories. It also raises fundamental questions about whether similar behaviors occur during the elongation of other aggregating systems, such

as physical gels. These correlations between cluster fragments, chain stretching, and elongational flow offer new insights into the rich mechanisms governing the rheology of large class of dense soft matter.

4.6 Acknowledgements

D.P. gratefully acknowledges DOE Grant No. DE-SC007908. The authors kindly acknowledge the use of computational resources provided by NSF MRI-1725573. This work was made possible in part by advanced computational resources deployed and maintained by Clemson Computing and Information Technology. This work was supported by the Sandia Laboratory Directed Research and Development Program. This work was performed, in part, at the Center for Integrated Nanotechnologies, an Office of Science User Facility operated for the U.S. Department of Energy (DOE) Office of Science. Sandia National Laboratories is a multimission laboratory managed and operated by National Technology & Engineering Solutions of Sandia, LLC, a wholly owned subsidiary of Honeywell International, Inc., for the U.S. DOE's National Nuclear Security Administration under Contract No. DENA-0003525. The views expressed in this article do not necessarily represent the views of the U.S. DOE or the United States Government.

4.7 References

(1) Beris, A. N.; Horner, J. S.; Jariwala, S.; Armstrong, M.; Wagner, N. J. Recent advances in blood rheology: A review. *Soft Matter* **2021**, *17*, 10591-10613.

- (2) Stein, D. B.; De Canio, G.; Lauga, E.; Shelley, M. J.; Goldstein, R. E. Swirling instability of the microtubule cytoskeleton. *Phys. Rev. Lett.* **2021**, *126* (2), 028103.
- (3) Hopkins, C. C.; Haward, S. J.; Shen, A. Q. Tristability in viscoelastic flow past side-by-side microcylinders. *Phys. Rev. Lett.* **2021**, *126* (5), 054501.
- (4) de Souza, G.; Tarpani, J. R. Interleaving CFRP and GFRP with a Thermoplastic Ionomer: The Effect on Bending Properties. *Appl. Compos. Mater.* **2021**, *28*, 559-572.
- (5) Li, B.; Zhang, C.; Peng, F.; Wang, W.; Vogt, B. D.; Tan, K. 4D printed shape memory metamaterial for vibration bandgap switching and active elastic-wave guiding. *J. Mater. Chem. C* **2021**, *9*, 1164-1173.
- (6) Wang, W.; Madsen, J.; Genina, N.; Hassager, O.; Skov, A. L.; Huang, Q. Toward a Design for Flowable and Extensible Ionomers: An Example of Diamine-Neutralized Entangled Poly (styrene-co-4-vinylbenzoic acid) Ionomer Melts. *Macromolecules* **2021**, *54* (5), 2306-2315.
- (7) Seiffert, S.; Kumacheva, E.; Okay, O.; Anthamatten, M.; Chau, M.; Dankers, P. Y.; Greenland, B. W.; Hayes, W.; Li, P.; Liu, R. *Supramolecular polymer networks and gels*; Springer, 2015.
- (8) Zhang, Z.; Huang, C.; Weiss, R.; Chen, Q. Association energy in strongly associative polymers. *J. Rheo.* **2017**, *61*, 1199-1207.
- (9) Zhang, Z.; Chen, Q.; Colby, R. H. Dynamics of associative polymers. *Soft Matter* **2018**, *14*, 2961-2977.
- (10) Hinton, Z. R.; Alvarez, N. J. The trade-off between processability and performance in commercial ionomers. *Rheol. Acta* **2019**, *58*, 499-511.

- (11) Hinton, Z. R.; Shabbir, A.; Alvarez, N. J. Dynamics of supramolecular self-healing recovery in extension. *Macromolecules* **2019**, *52*, 2231-2242.
- (12) Israelachvili, J. N. *Intermolecular and surface forces*; Academic press, 2015.
- (13) Wu, S.; Chen, Q. Advances and New Opportunities in the Rheology of Physically and Chemically Reversible Polymers. *Macromolecules* **2021**, *55*, on line.
- (14) Eisenberg, A. Clustering of ions in organic polymers. A theoretical approach. *Macromolecules* **1970**, *3*, 147-154.
- (15) Shabbir, A.; Huang, Q.; Chen, Q.; Colby, R. H.; Alvarez, N. J.; Hassager, O. Brittle fracture in associative polymers: the case of ionomer melts. *Soft Matter* **2016**, *12*, 7606-7612.
- (16) Shabbir, A.; Huang, Q.; Baeza, G. P.; Vlassopoulos, D.; Chen, Q.; Colby, R. H.; Alvarez, N. J.; Hassager, O. Nonlinear shear and uniaxial extensional rheology of polyether-ester-sulfonate copolymer ionomer melts. *J. Rheol.* **2017**, *61*, 1279-1289.
- (17) Ling, G. H.; Wang, Y.; Weiss, R. Linear viscoelastic and uniaxial extensional rheology of alkali metal neutralized sulfonated oligostyrene ionomer melts. *Macromolecules* **2012**, *45*, 481-490.
- (18) Wu, S.; Cao, X.; Zhang, Z.; Chen, Q.; Matsumiya, Y.; Watanabe, H. Molecular design of highly stretchable ionomers. *Macromolecules* **2018**, *51*, 4735-4746.
- (19) Wingstrand, S. L.; Alvarez, N. J.; Huang, Q.; Hassager, O. Linear and nonlinear universality in the rheology of polymer melts and solutions. *Phys. Rev. Lett.* **2015**, *115*, 078302.

- (20) Morelly, S. L.; Palmese, L.; Watanabe, H.; Alvarez, N. J. Effect of finite extensibility on nonlinear extensional rheology of polymer melts. *Macromolecules* **2019**, *52*, 915-922.
- (21) Costanzo, S.; Huang, Q.; Ianniruberto, G.; Marrucci, G.; Hassager, O.; Vlassopoulos, D. Shear and extensional rheology of polystyrene melts and solutions with the same number of entanglements. *Macromolecules* **2016**, *49*, 3925-3935.
- (22) André, A.; Shahid, T.; Oosterlinck, F.; Clasen, C.; Van Ruymbeke, E. Investigating the transition between polymer melts and solutions in nonlinear elongational flow. *Macromolecules* **2021**, *54*, 2797-2810.
- (23) Shahid, T.; Clasen, C.; Oosterlinck, F.; van Ruymbeke, E. Diluting entangled polymers affects transient hardening but not their steady elongational viscosity. *Macromolecules* **2019**, *52*, 2521-2530.
- (24) O'Connor, T. C.; Alvarez, N. J.; Robbins, M. O. Relating chain conformations to extensional stress in entangled polymer melts. *Phys. Rev. Lett.* **2018**, *121*, 047801.
- (25) O'Connor, T. C.; Hopkins, A.; Robbins, M. O. Stress relaxation in highly oriented melts of entangled polymers. *Macromolecules* **2019**, *52*, 8540-8550.
- (26) Ianniruberto, G.; Marrucci, G. Molecular dynamics reveals a dramatic drop of the friction coefficient in fast flows of polymer melts. *Macromolecules* **2020**, *53*, 2627-2633.
- (27) Ianniruberto, G.; Marrucci, G.; Masubuchi, Y. Melts of linear polymers in fast flows. *Macromolecules* **2020**, *53*, 5023-5033.
- (28) Ianniruberto, G.; Brasiello, A.; Marrucci, G. Simulations of fast shear flows of PS oligomers confirm monomeric friction reduction in fast elongational flows of

monodisperse PS melts as indicated by rheoptical data. *Macromolecules* **2012**, *45*, 8058-8066.

(29) Yaoita, T.; Isaki, T.; Masubuchi, Y.; Watanabe, H.; Ianniruberto, G.; Marrucci, G. Primitive chain network simulation of elongational flows of entangled linear chains: Stretch/orientation-induced reduction of monomeric friction. *Macromolecules* **2012**, *45*, 2773-2782.

(30) Baig, C.; Mavrantzas, V. G.; Kroger, M. Flow effects on melt structure and entanglement network of linear polymers: Results from a nonequilibrium molecular dynamics simulation study of a polyethylene melt in steady shear. *Macromolecules* **2010**, *43*, 6886-6902.

(31) McIlroy, C.; Olmsted, P. D. Deformation of an amorphous polymer during the fused-filament-fabrication method for additive manufacturing. *J. Rheol.* **2017**, *61*, 379-397.

(32) Schaefer, C.; Laity, P. R.; Holland, C.; McLeish, T. C. Stretching of Bombyx mori Silk Protein in Flow. *Molecules* **2021**, *26* (6), 1663.

(33) Schaefer, C.; McLeish, T. C. B. Theoretical rheo-physics of silk: Intermolecular associations reduce the critical specific work for flow-induced crystallisation. *arXiv:2112.01965* **2021**.

(34) Senanayake, M.; Perahia, D.; Grest, G. S. Effects of interaction strength of associating groups on linear and star polymer dynamics. *J. Chem. Phys.* **2021**, *154*, 074903.

(35) Kremer, K.; Grest, G. S. Dynamics of entangled linear polymer melts: A molecular-dynamics simulation. *J. Chem. Phys.* **1990**, *92*, 5057-5086.

- (36) Auhl, R.; Everaers, R.; Grest, G. S.; Kremer, K.; Plimpton, S. J. Equilibration of long chain polymer melts in computer simulations. *J. Chem. Phys.* **2003**, *119*, 12718-12728.
- (37) Grest, G. S. Communication: Polymer entanglement dynamics: Role of attractive interactions. *J. Chem. Phys.* **2016**, *145* (14), 141101.
- (38) Daivis, P. J.; Todd, B. A simple, direct derivation and proof of the validity of the SLLOD equations of motion for generalized homogeneous flows. *J. Chem. Phys.* **2006**, *124* (19), 194103.
- (39) Dobson, M. Periodic boundary conditions for long-time nonequilibrium molecular dynamics simulations of incompressible flows. *J. Chem. Phys.* **2014**, *141*, 184103.
- (40) Nicholson, D. A.; Rutledge, G. C. Molecular simulation of flow-enhanced nucleation in n-eicosane melts under steady shear and uniaxial extension. *J. Chem. Phys.* **2016**, *145*, 244903. DOI: 10.1063/1.4972894.
- (41) Doi, M.; Edwards, S. F. *The theory of polymer dynamics*; oxford university press, 1988.
- (42) O'Connor, T. C.; Ge, T.; Rubinstein, M.; Grest, G. S. Topological linking drives anomalous thickening of ring polymers in weak extensional flows. *Phys. Rev. Lett.* **2020**, *124* (2), 027801.
- (43) Borger, A.; Wang, W.; O'Connor, T. C.; Ge, T.; Grest, G. S.; Jensen, G. V.; Ahn, J.; Chang, T.; Hassager, O.; Mortensen, K. Threading–unthreading transition of linear-ring polymer blends in extensional flow. *ACS Macro Lett.* **2020**, *9*, 1452-1457.
- (44) Sukumaran, S. K.; Grest, G. S.; Kremer, K.; Everaers, R. Identifying the primitive path mesh in entangled polymer liquids. *J. Polym. Sci. B Polym. Phys.* **2005**, *43*, 917-933.

- (45) Hoy, R. S.; Foteinopoulou, K.; Kröger, M. Topological analysis of polymeric melts: Chain-length effects and fast-converging estimators for entanglement length. *Phys. Rev. E* **2009**, *80*, 031803.
- (46) Ge, T.; Robbins, M. O.; Perahia, D.; Grest, G. S. Healing of polymer interfaces: Interfacial dynamics, entanglements, and strength. *Phys. Rev. E* **2014**, *90*, 012602.
- (47) Thompson, A. P.; Aktulga, H. M.; Berger, R.; Bolintineanu, D. S.; Brown, W. M.; Crozier, P. S.; in't Veld, P. J.; Kohlmeyer, A.; Moore, S. G.; Nguyen, T. D. LAMMPS-A flexible simulation tool for particle-based materials modeling at the atomic, meso, and continuum scales. *Comput. Phys. Commun.* **2021**, *271*, 108171.

CHAPTER FIVE

RESPONSE OF SULFONATED POLYSTYRENE MELTS TO NONLINEAR ELONGATION FLOWS

5.1 Abstract

Ionizable polymers form dynamic networks with domains controlled by two distinct energy scales, ionic interactions and van der Waals forces, that evolve under elongational flows during their processing into viable materials. Molecular level insight of their non-linear response, paramount to controlling their structure, is attained by fully atomistic molecular dynamics simulations of a model ionizable polymer, randomly sulfonated polystyrene. As a function of increasing elongational flow rates, these networks display an initial elastic response followed by an ionic strength dependent strain hardening, and eventually strain-thinning. Flow-driven ionic assembly dynamics that continuously break and reform, control the response of the melts, resulting in a heterogeneous distribution of chain elongation.

5.2 Introduction

Macromolecules behavior under flow and shear is in the core of their processing into variable materials.¹⁻³ Their response to shear and extensional flow has shed light on fundamental characteristics that lead to the unique viscoelastic properties of polymers,^{4, 5} where any constraint such as chemical^{6, 7} or physical^{8, 9} crosslinks, or entanglements^{10, 11} have profound effects on their response.^{12, 13} Flow often drives stretching and alignment of macromolecules resulting in shear thinning and crystallization.^{14, 15} With significant

ongoing efforts to resolve the effects of elongational flow on entangled flexible and semiflexible polymers,^{15,16} little is known on the response of macromolecules that consist of multiple chemically distinct segments, with distinct but different interactions, within one chains. Here using fully atomistic molecular dynamics (MD) simulations, we study the effects of elongational flow on polymers with distinct chemical groups whose behavior is controlled by vastly different energy scales.

Significant number of macromolecules, with an immense technological impact,^{2,3} consist of more than one component resulting in fluids whose structure and dynamics are controlled by distinct energy scales. One such a class is formed by ionizable polymers whose melt structure consists of ionic assemblies, either as clusters or as continuous networks, controlled by electrostatic interactions, in a matrix of nonionic polymers, controlled by van der Waals forces.^{17,18} These polymers are characterized by higher melt and solution viscosities compared with their non-ionic homologues, attributed to interchain associations of the ionic groups that slow chain relaxation. The properties of these polymers depend not only on the chemical structure of the polymer but also on the number, strength, and distribution of the ionic groups.^{12,19-27} Fundamentally, the challenge lies in the response of a system that consists of two distinct energy scales, van der Waals interactions that dominates the non-ionic domains, and electrostatic interactions that are typically an order of magnitude stronger.^{1,18}

Experiments^{28,29} and simulations^{16,30} have shown that chemically distinct polymer melts whose inherent stress relaxation characteristics follows similar scaling, exhibit different behavior in elongational flows. Ongoing studies have focused on the response of

flexible and semiflexible polymers whose motion is constrained by entanglements.^{10, 11, 31} In these systems, flow effects have been theoretically attributed to different phenomena, all pointing to reduction in the entanglement time τ_e , of the polymers. One approach constitutes extending equilibrium theories of entangled melts, envisioning the entanglement as dynamic constraints that becomes highly anisotropic under flow, affecting the entanglement length.³²⁻³⁵ O’Conner et al.³⁰ described the chain relaxation by equilibrium parameters such as the Rouse time and disentanglement times. On the other hand, Ianniruberto et al. and Costanzo et al. have shown that under flow the monomeric friction between polymeric chains decreases as they align, leading to a decrease in τ_e with increasing flow rate.^{36, 37}

On route to understanding the response of polymers to elongational flows, we³⁸ recently probed associative polymers, macromolecules that assemble due to attraction between distinctive groups along their backbone, using a coarse-grained (CG) bead spring model. The interaction strength of the associating groups, which was randomly introduced along the backbone was varied. We found that the heterogeneous breakup of the associative clusters under flow drive dynamic heterogeneity of the chains and nanostructured flow patterns that could impact the processing of complex fluids.

This coarse-grained study provides a first glimpse into the response of associating polymers to elongational flows. However, controlling the response of ionizable polymer networks requires the atomistic details that determine the structure of the ionic assemblies and the chain conformation. It is particularly critical since the actual morphology of the ionic assemblies, including spherical, elongated and even ladder-like structures²⁴ to those

of continuous networks, depends on the degree of ionization of the polymers and electrostatic surroundings affecting the macroscopic dynamics of these networks.

The current study explores molecular length scale effects of elongational flow of intrinsically unentangled melts of sulfonated polystyrene (SPS) in its sodium salt form, as the number of ionizable groups tethered is varied from a fraction $f = 0$ to 0.55 of the available sites. This sulfonation levels span the range from the ionomer regime, where distinct clusters are formed, to the polyelectrolyte regime where the melts consist of bicontinuous ionic-nonionic domains. We find that dynamic nature of the ionizable clusters is in the core of the response of ionizable polymers to elongational flow, where the molecular insight offers significant new grasp of the response of distinctive domains, formed in ionizable polymers.

5.3 Model and simulation methods

Sulfonated atactic polystyrene molecules of molecular weight ~ 11000 g/mol (106 monomers) were constructed using Polymer Builder and Amorphous Cell modules in BIOVIA™ Materials Studio. Sulfonation groups were randomly added along each chain to reach the desired fraction. The five systems contained a total of 148, 148, 138, 145 and 148 unique molecules for $f = 0, 0.9, 0.20, 0.35$ and 0.55 respectively. The All-Atom Optimized Potentials for Liquid Simulations (OPLS-AA) force field³⁹⁻⁴¹ was used to model the interactions. Additional parameters for the sulfonate groups are specified in references 44-46.^{42, 43} Each system was equilibrated at $T=500\text{K}$, following the procedure described in Mohottalalage et al.²⁵ and then run for 1000 ns.

To model uniaxial extensional flow, melts are elongated along the z-axis at a constant Hencky strain rate $\varepsilon \equiv \partial \ln L(t) / \partial t$, where $L(t)$ is the length of the simulation cell at time t in the elongation direction. Since the melts are nearly incompressible, the two perpendicular directions are contracted to keep the density constant. Flow is maintained by integrating the g-SLLOD equations of motion, and generalized Kraynik-Reinelt boundary conditions are used to prevent the simulation box from becoming too small in the perpendicular directions.^{44,45} The extensional stress σ_E is difference between the stress component along the extension axis (z-axis) and the average stress in the transverse directions. The transient extensional viscosity (stress growth coefficient) $\eta_E^+ = \sigma_E / \dot{\varepsilon}$. These simulations can achieve uniaxial elongational flows with large strains and enables us to access steady-state statistics in our atomistic samples. The steady-state properties are obtained by averaging simulation data over an interval of strain ε from 5 to 10 which corresponds to stretch $\lambda = L(t)/L(0)$ from ~ 150 -22000. This large range of extensions is typically not achieved experimentally.⁴⁶⁻⁴⁸ Over this range of strain, the stress fluctuates about a well-defined average value. In this regime, we denote the average steady-state viscosity by η_E to distinguish from the early time transient viscosity $\eta_E^+(\varepsilon)$. In the present study, we varied the strain rate from $\dot{\varepsilon} = 10^{7.5}$ to 10^9 s^{-1} . All simulations were carried out using LAMMPS with a time step of $\delta t = 1 \text{ fs}$.

5.4 Results

Visualization of the various constituents of the melts at low and at high strain rates presented in Figure 5.1. As the response of the system differs significantly at low and high strain rates, different length scales are depicted in the visualization.

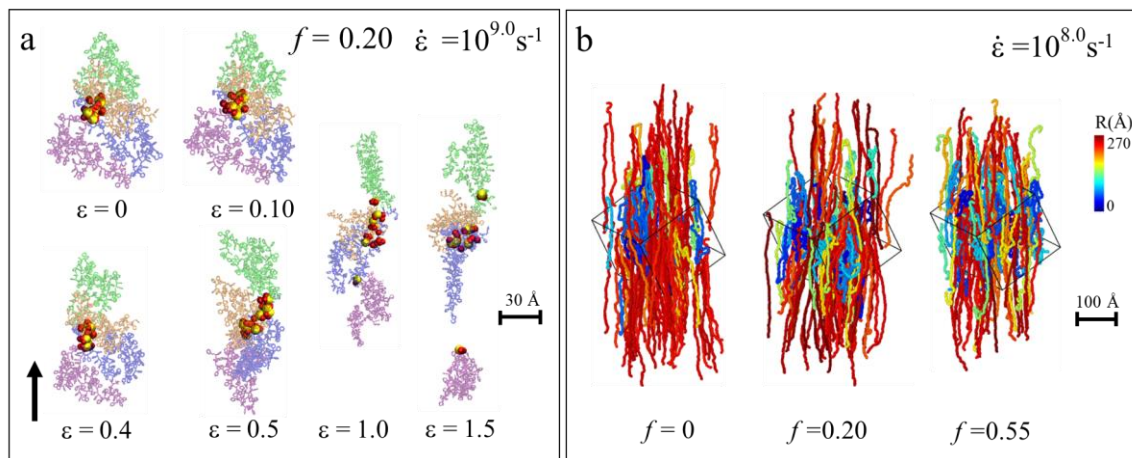


Figure 5.1: (a) Visualization of an isolated cluster of SO_3^- groups (yellow and red spheres are sulfur and oxygen respectively) at the indicated strain ϵ for $f = 0.20$ and $\dot{\epsilon} = 10^9 \text{ s}^{-1}$, plotted with representative associated polymer chains. The different colors represent distinct chains. Black arrow corresponds to the flow direction. (b) Snapshots of the polymer backbone for strain $\epsilon = 10$ for the indicated sulfonation levels for $\dot{\epsilon} = 10^8 \text{ s}^{-1}$. Chains are colored according to their end-to-end distance R .

In Figure 5.1a, a representative cluster and the chains tethered to the sulfur groups are depicted for low strain, while in Figure 5.1b, the backbone of the chains is visualized at high strain $\epsilon = 10$. At low strain, the chains first stretch and retract, typical for the elastic regime. Increasing the strain results in breakup of the clusters. At high strain, a significant heterogeneity of chain elongation is observed as shown in Figure 5.1b. This heterogeneity increases significantly with f . The intermix of chain elongation is attributed to constraints exerted on the chains by the ionic clusters. With increasing f , both the size and the number

of clusters as well as the degree of continuity of the ionic assemblies all increase, resulting in larger inhomogeneity in chain elongation.

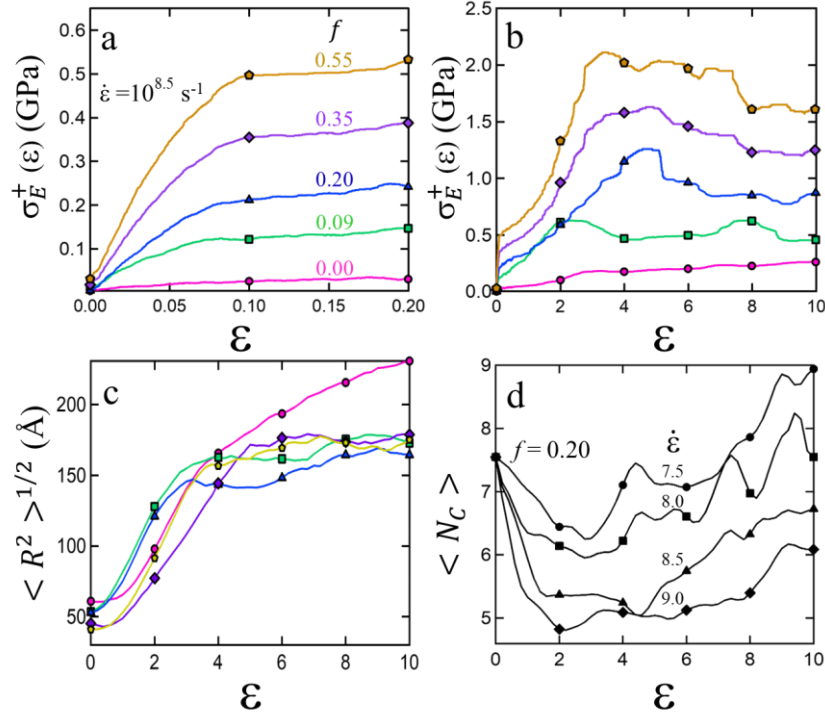


Figure 5.2: Transient extensional stress $\sigma_E^+(\epsilon)$ as a function of strain ϵ at the indicated sulfonation fraction f for (a) low strain ϵ and (b) for the entire range of strains ϵ up to 10 for $\dot{\epsilon} = 10^{8.5} \text{ s}^{-1}$. (c) Average rms end-to-end $\langle R^2 \rangle^{1/2}$ of the chains for $\dot{\epsilon} = 10^{8.5} \text{ s}^{-1}$ and (d) average size of the ionic cluster $\langle N_C \rangle$ for $f = 0.20$ for shear rates $\dot{\epsilon} = 10^{7.5} \text{ s}^{-1}$, $10^{8.0} \text{ s}^{-1}$, $10^{8.5} \text{ s}^{-1}$, and $10^{9.0} \text{ s}^{-1}$, from top to bottom.

The chain response in terms of the transient extensional stress $\sigma_E^+(\epsilon)$ as a function of strain is presented in Figure 5.2, together with the corresponding chain dimensions and average cluster size. At low strain rates (Figure 5.2a) an initial linear response ($0 < \epsilon < 0.1$) is observed for all ionizable polymers ($f > 0$), followed by strain-hardening up to a strain $\epsilon \sim 1-3$. At larger strains, the system softens. An initial elastic response is typical for many polymers. However strain hardening has been observed experimentally by Shabbir et al.⁹

and Stadler et al.⁴⁹ for limited number of polymers but the molecular origin is yet to be determined.

In the initial region the average chain dimension does not change as shown in Figure 5.2c. This region is well described by traditional rubber elasticity. With increasing strain rates, the stress increases, indicative of a strain hardening regime which is rather surprising for unentangled melts. Practically while the polymer backbone is at temperatures above their glass transition temperature (i.e., in the liquid phase), the presence of ionic assemblies drives strain hardening, a behavior which is typical to solids. A close look at $\langle R^2 \rangle^{1/2}$ shows that the chains elongate as the clusters break as shown in Figure 5.2d for $f=0.20$. Thus, the hardening is attributed to the work to break up the clusters and stretch the chains. At higher strain, the stress decreases, indicative of softening of the melt. This softening is attributed to the dynamic nature of the ionizable assemblies that form and reform under elongational flows.³⁸ In absence of ionizable groups, $f=0$, the chain assumes different characteristics where hardly any strain-hardening is observed.

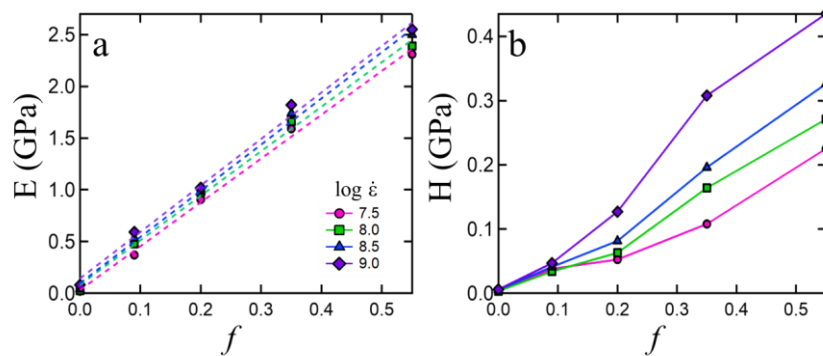


Figure 5.3: (a) Elastic modulus E , and (b) hardening modulus H , as a function of sulfonation fraction f .

From classical rubber elasticity, the modulus $E = \frac{\sigma_E^+(\varepsilon)}{\lambda^2 - \lambda^{-1}}$. Results for E as a function of sulfonation fraction f are shown in Figure 5.3a. E increases linearly with sulfonation fraction and is essentially independent on the extensional strain rates. The hardening modulus H is shown Figure 5.3b increases with f all extensional strain rates. The hardening modulus for PS ($f = 0$) is independent of strain rates and slightly increases with strain rates up to $f \sim 0.2$ (in the ionomer regime).

With increasing f to the polyelectrolyte region, H increases significantly with the strain rate. In the polyelectrolyte region, the ionic assemblies form larger continuous networks where constant formation and breaking up of clusters in the presence of extensional flows becomes a more convoluted process.

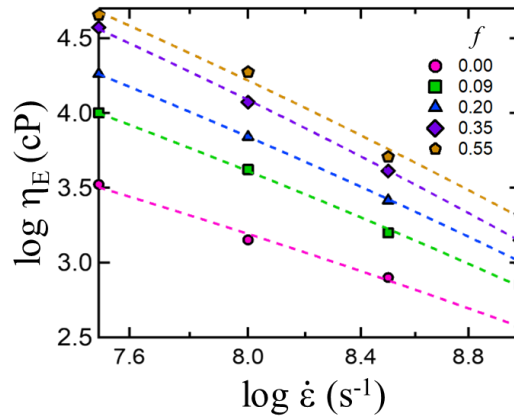


Figure 5.4: Terminal viscosities η_E versus extensional strain rate $\dot{\varepsilon}$ for the indicated sulfonation fractions.

The steady-state viscosity η_E is shown in Figure 5.4, decreases with increasing extensional rate $\dot{\varepsilon}^\beta$ for all f indicative of strain thinning. The thinning exponent $\beta = -0.6$ for $f = 0$ which is consistent with recent experiments by Sridhar et al.⁵⁰ and Marrucci et

al.⁵¹ where they observed similar trends of thinning behavior with $\beta = -0.5$ for PS melts. As the sulfonation fraction increases, β decreases from -0.6 for $f = 0$ to -0.9 for $f = 0.55$, suggesting a stronger extensional thinning with increasing sulfonation fractions. With the polymer backbone reaching their largest extension at strains of ~ 4 for $f > 0$, the shear thinning is attributed to the dynamic nature of the clusters whose average size increases with increasing sulfonations.

The interrelation between ionic assemblies and chain conformation under flow is in the core of the response of the polymer. The probability distribution $P(R)$ of the *end-to-end* distances of the chains, under flow are shown in Figure 5.5a. The non-sulfonated PS ($f = 0$) exhibits a well-defined distribution at small R in equilibrium (quiescent melts, not exposed to flow).

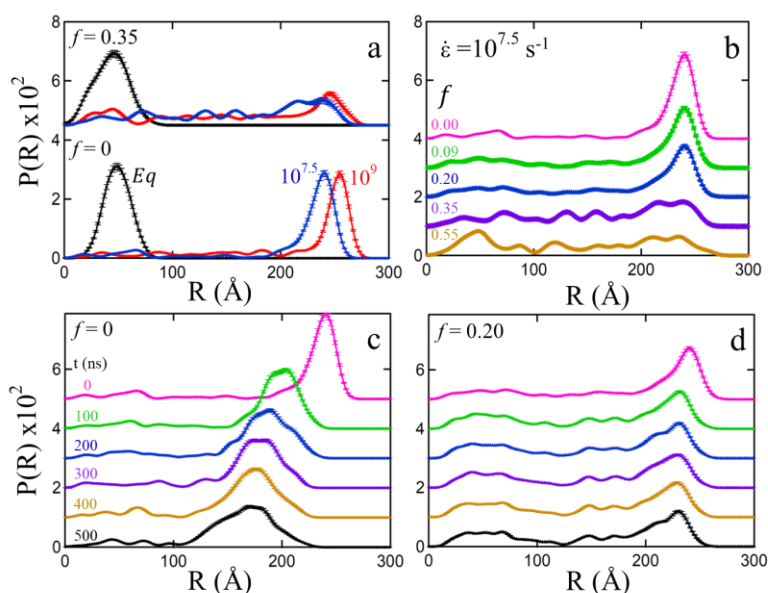


Figure 5.5: (a) Distribution $P(R)$ of the end-to-end distance R for $f = 0$ and 0.35 in equilibrium and at 2 extension rates. Curves are shifted by 0.045 for clarity. (b) $P(R)$ at $\dot{\epsilon} = 10^{7.5} \text{ s}^{-1}$ for 5 values of f . Curves are shifted by 0.01 vertically for clarity. $P(R)$ after secession of flow at a rate of $\dot{\epsilon} = 10^{7.5} \text{ s}^{-1}$ and strain $\epsilon = 10$ for (c) $f = 0$ and (d) for $f = 0.2$.

As expected,^{16, 29, 30, 48, 52} the peak of the end-to-end distribution shifts to larger R , indicative that the chains under elongational flow. However, for $f > 0$, continuous break up and reform of ionic clusters lead to heterogeneity in the elongation of individual polymer chains. As a result, a broad distribution of the end-to-end distance R is observed at respective extensional rates as shown in Figure 5.5b. The peak intensity corresponding to the distribution at a large R decreases with f , further indicates the nonlinear deformation causes ionic clusters to breakup and reorganize rapidly as chains elongate in the flow field. The ionic assemblies clearly control the response of the polymers to elongational flows that are exerted during processing. Understanding the relaxation of the ionizable polymers following succession of elongational flows provides is critical to controlling their structure. $P(R)$ at different times following succession of flow is shown in Figure 5.5c,d for $f=0$ and $f=0.20$. For $f=0$, the chains partially relax over this time as the diffusive time τ_d , is longer than the simulation time. This is consistent with recent studies O'Connor et al.³⁰ that showed that independent of the initial alignment, extended noncharged chains relax back to equilibrium conformations on times $\sim 2 \tau_d$. However, upon increasing the number of ionic groups, a slower retraction is observed for $f = 0.09$ (not shown) and almost no retraction is detected for $f=0.20$ on the time scale of our studies. The chain relaxation process of the elongational flow induced aligned state is considerably slower for SPS systems compare with PS.

5.5 Conclusions

Here, using atomistic molecular simulations we determined the effects of uniaxial elongational flow on SPS melts at sulfonation levels that captures the ionomer and polyelectrolyte regimes. For all $f > 0$, with increasing flow rates an elastic region at small strain is observed followed by strain hardening, a behavior which is typical to solids, and is attributed to the presence of ionic clusters that constrain the chain motion and impact their elongation. At higher strain, the clusters break and reform driving a softening of the melts. The incorporation of sulfonate groups onto PS chains produced a significant increase in the transient stress in the presence of extensional flows. Increasing sulfonation levels increases the extensional stress. The stress develops an overshoot for SPS and the amplitude of the stress overshoot increases with increasing sulfonation level. In parallel, the extensional viscosity of ionomers increases with decreasing strain rate. This is true for all systems investigated however, as the sulfonation level increases the shear-thinning becomes stronger as β decreases.

Substantial heterogeneity in chain stretching is observed for higher sulfonated PS because chains that are trapped within ionic clusters show resistance to align in the presence of extensional flows. This is in accordance with the general trend that the ionic polymer become non-processable at higher ion contents. These ionic clusters undergo continuous strain induced breakup and reassociation of ionic groups under flows. Chain retraction during relaxation from aligned states is closely monitored. These relaxation processes are sensitive to the clusters, leading to slow relaxation of the polymer chains.

Overall, many observations reported through computational studies provide a molecular level insight into long-lived challenges in ionic polymer processing.

5.6 Acknowledgments

D. P. gratefully acknowledges DOE Grant No. DE-SC007908. T. O. gratefully acknowledges startup funding provided by Carnegie Mellon University. The authors kindly acknowledge the use of computational resources provided by NSF MRI-1725573. This work was made possible in part by advanced computational resources deployed and maintained by Clemson Computing and Information Technology. This work was supported by the Sandia Laboratory Directed Research and Development Program. This work was performed, in part, at the Center for Integrated Nanotechnologies, an Office of Science User Facility operated for the U.S. Department of Energy (DOE) Office of Science. Sandia National Laboratories is a multimission laboratory managed and operated by National Technology & Engineering Solutions of Sandia, LLC, a wholly owned subsidiary of Honeywell International, Inc., for the U.S. DOE's National Nuclear Security Administration under Contract No. DENA-0003525. The views expressed in this article do not necessarily represent the views of the U.S. DOE or the United States Government.

5.7 References

(1) Ling, G. H.; Wang, Y.; Weiss, R. Linear viscoelastic and uniaxial extensional rheology of alkali metal neutralized sulfonated oligostyrene ionomer melts. *Macromolecules* **2012**, *45*, 481-490.

- (2) Hinton, Z. R.; Alvarez, N. J. The trade-off between processability and performance in commercial ionomers. *Rheol. Acta* **2019**, *58*, 499-511.
- (3) Hinton, Z. R.; Shabbir, A.; Alvarez, N. J. Dynamics of supramolecular self-healing recovery in extension. *Macromolecules* **2019**, *52*, 2231-2242.
- (4) Qiao, X.; Weiss, R. Nonlinear rheology of lightly sulfonated polystyrene ionomers. *Macromolecules* **2013**, *46*, 2417-2424.
- (5) Weiss, R.; Yu, W.-C. Viscoelastic behavior of very lightly sulfonated polystyrene ionomers. *Macromolecules* **2007**, *40*, 3640-3643.
- (6) Sugimoto, M.; Hida, H.; Taniguchi, T.; Koyama, K.; Aoki, Y. Rheological properties of poly (vinyl chloride)/plasticizer systems—relation between sol–gel transition and elongational viscosity. *Rheologica Acta* **2007**, *46*, 957-964.
- (7) Friedrich, T.; Tieke, B.; Stadler, F. J.; Bailly, C. Improvement of elasticity and strength of poly (N-isopropylacrylamide) hydrogels upon copolymerization with cationic surfmers. *Soft Matter* **2011**, *7*, 6590-6597.
- (8) Shabbir, A.; Huang, Q.; Chen, Q.; Colby, R. H.; Alvarez, N. J.; Hassager, O. Brittle fracture in associative polymers: the case of ionomer melts. *Soft Matter* **2016**, *12*, 7606-7612.
- (9) Shabbir, A.; Huang, Q.; Baeza, G. P.; Vlassopoulos, D.; Chen, Q.; Colby, R. H.; Alvarez, N. J.; Hassager, O. Nonlinear shear and uniaxial extensional rheology of polyether-ester-sulfonate copolymer ionomer melts. *J. Rheol.* **2017**, *61*, 1279-1289.

- (10) Masubuchi, Y.; Matsumiya, Y.; Watanabe, H. Test of orientation/stretch-induced reduction of friction via primitive chain network simulations for polystyrene, polyisoprene, and poly (n-butyl acrylate). *Macromolecules* **2014**, *47*, 6768-6775.
- (11) Yaoita, T.; Isaki, T.; Masubuchi, Y.; Watanabe, H.; Ianniruberto, G.; Marrucci, G. Primitive chain network simulation of elongational flows of entangled linear chains: Stretch/orientation-induced reduction of monomeric friction. *Macromolecules* **2012**, *45*, 2773-2782.
- (12) Huang, C.; Chen, Q.; Weiss, R. Rheological behavior of partially neutralized oligomeric sulfonated polystyrene ionomers. *Macromolecules* **2017**, *50*, 424-431.
- (13) Weiss, R.; Zhao, H. Rheological behavior of oligomeric ionomers. *J. Rheol.* **2009**, *53*, 191-213.
- (14) Nafar Sefiddashti, M. H.; Edwards, B. J.; Khomami, B. Communication: A coil-stretch transition in planar elongational flow of an entangled polymeric melt. *J. Chem. Phys.* **2018**, *148*, 141103.
- (15) Sefiddashti, M. H. N.; Edwards, B. J.; Khomami, B. Configurational microphase separation in elongational flow of an entangled polymer liquid. *Phys. Rev. Lett.* **2018**, *121*, 247802.
- (16) O'Connor, T. C.; Alvarez, N. J.; Robbins, M. O. Relating chain conformations to extensional stress in entangled polymer melts. *Phys. Rev. Lett.* **2018**, *121*, 047801.
- (17) Eisenberg, A.; Hird, B.; Moore, R. A new multiplet-cluster model for the morphology of random ionomers. *Macromolecules* **1990**, *23*, 4098-4107.
- (18) Eisenberg, A.; Kim, J.-S. *Introduction to ionomers*; Wiley, New York,, 1998.

- (19) Castagna, A. M.; Wang, W.; Winey, K. I.; Runt, J. Influence of cation type on structure and dynamics in sulfonated polystyrene ionomers. *Macromolecules* **2011**, *44*, 5420-5426.
- (20) Chu, B.; Wu, D. Q.; Lundberg, R. D.; MacKnight, W. J. Small-angle X-ray scattering (SAXS) studies of sulfonated polystyrene ionomers. 1. Anomalous SAXS. *Macromolecules* **1993**, *26*, 994-999.
- (21) Lefelar, J. A.; Weiss, R. A. Concentration and counterion dependence of cluster formation in sulfonated polystyrene. *Macromolecules* **1984**, *17*, 1145-1148.
- (22) Zhang, L.; Brostowitz, N. R.; Cavicchi, K. A.; Weiss, R. Perspective: Ionomer research and applications. *Macro. Reaction Eng.* **2014**, *8*, 81-99.
- (23) Agrawal, A.; Perahia, D.; Grest, G. S. Clustering effects in ionic polymers: Molecular dynamics simulations. *Phys. Rev. E* **2015**, *92*, 022601.
- (24) Agrawal, A.; Perahia, D.; Grest, G. S. Cluster morphology-polymer dynamics correlations in sulfonated polystyrene melts: computational study. *Phys. Rev. Lett.* **2016**, *116*, 158001.
- (25) Mohottalalage, S. S.; Aryal, D.; Thurston, B. A.; Grest, G. S.; Perahia, D. Effects of Ionic Group Distribution on the Structure and Dynamics of Amorphous Polymer Melts. *Macromolecules* **2021**, *55*, 217–223.
- (26) Stadler, F. J.; Pyckhout-Hintzen, W.; Schumers, J.-M.; Fustin, C.-A.; Gohy, J.-F.; Bailly, C. Linear viscoelastic rheology of moderately entangled telechelic polybutadiene temporary networks. *Macromolecules* **2009**, *42*, 6181-6192.
- (27) Middleton, L. R.; Tarver, J. D.; Cordaro, J.; Tyagi, M.; Soles, C. L.; Frischknecht, A. L.; Winey, K. I. Heterogeneous chain dynamics and aggregate lifetimes in precise acid-

- containing polyethylenes: Experiments and simulations. *Macromolecules* **2016**, *49*, 9176-9185.
- (28) Morelly, S. L.; Palmese, L.; Watanabe, H.; Alvarez, N. J. Effect of finite extensibility on nonlinear extensional rheology of polymer melts. *Macromolecules* **2019**, *52*, 915-922.
- (29) Ianniruberto, G.; Marrucci, G.; Masubuchi, Y. Melts of linear polymers in fast flows. *Macromolecules* **2020**, *53*, 5023-5033.
- (30) O'Connor, T. C.; Hopkins, A.; Robbins, M. O. Stress relaxation in highly oriented melts of entangled polymers. *Macromolecules* **2019**, *52*, 8540-8550.
- (31) Yaoita, T.; Isaki, T.; Masubuchi, Y.; Watanabe, H.; Ianniruberto, G.; Marrucci, G. Primitive chain network simulation of elongational flows of entangled linear chains: Role of finite chain extensibility. *Macromolecules* **2011**, *44*, 9675-9682.
- (32) Ianniruberto, G.; Marrucci, G. Convective constraint release (CCR) revisited. *J. Rheo.* **2014**, *58*, 89-102.
- (33) Ianniruberto, G. Quantitative appraisal of a new CCR model for entangled linear polymers. *J. Rheo.* **2015**, *59*, 211-235.
- (34) Mead, D. W.; Banerjee, N.; Park, J. A constitutive model for entangled polymers incorporating binary entanglement pair dynamics and a configuration dependent friction coefficient. *J. Rheo.* **2015**, *59*, 335-363.
- (35) Sato, T.; Taniguchi, T. Rheology and entanglement structure of well-entangled polymer melts: A slip-link simulation study. *Macromolecules* **2019**, *52*, 3951-3964.
- (36) Ianniruberto, G.; Brasiello, A.; Marrucci, G. Simulations of fast shear flows of PS oligomers confirm monomeric friction reduction in fast elongational flows of

monodisperse PS melts as indicated by rheoptical data. *Macromolecules* **2012**, *45*, 8058-8066.

(37) Costanzo, S.; Huang, Q.; Ianniruberto, G.; Marrucci, G.; Hassager, O.; Vlassopoulos, D. Shear and extensional rheology of polystyrene melts and solutions with the same number of entanglements. *Macromolecules* **2016**, *49*, 3925-3935.

(38) Mohottalalage, S. S.; Senanayake, M.; Clemmer, J. T.; Perahia, D.; Grest, G. S.; O'Connor, T. Nonlinear Elongation Flows in Associating Polymer Melts: From Homogeneous to Heterogeneous Flow. *Phy. Rev. X* **2022**, *12*, 021024.

(39) Jorgensen, W. L.; Maxwell, D. S.; Tirado-Rives, J. Development and testing of the OPLS all-atom force field on conformational energetics and properties of organic liquids. *J. Am. Chem. Soc.* **1996**, *118*, 11225-11236.

(40) Jorgensen, W. L.; Madura, J. D.; Swenson, C. J. Optimized intermolecular potential functions for liquid hydrocarbons. *J. Am. Chem. Soc.* **1984**, *106*, 6638-6646.

(41) Murzyn, K.; Bratek, M.; Pasenkiewicz-Gierula, M. Refined OPLS all-atom force field parameters for n-pentadecane, methyl acetate, and dimethyl phosphate. *J. Phys. Chem. B* **2013**, *117*, 16388-16396.

(42) He, X.; Guvench, O.; MacKerell Jr, A. D.; Klein, M. L. Atomistic simulation study of linear alkylbenzene sulfonates at the water/air interface. *J. Phys. Chem. B* **2010**, *114*, 9787-9794.

(43) Cannon, W. R.; Pettitt, B. M.; McCammon, J. A. Sulfate anion in water: model structural, thermodynamic, and dynamic properties. *J. Phys. Chem.* **1994**, *98*, 6225-6230.

- (44) Dobson, M. Periodic boundary conditions for long-time nonequilibrium molecular dynamics simulations of incompressible flows. *J. Chem. Phys.* **2014**, *141*, 184103.
- (45) Nicholson, D. A.; Rutledge, G. C. Molecular simulation of flow-enhanced nucleation in n-eicosane melts under steady shear and uniaxial extension. *J. Chem. Phys.* **2016**, *145*, 244903. DOI: 10.1063/1.4972894.
- (46) Nielsen, J. K.; Rasmussen, H. K.; Hassager, O.; McKinley, G. H. Elongational viscosity of monodisperse and bidisperse polystyrene melts. *J. Rheo.* **2006**, *50*, 453-476.
- (47) Bach, A.; Almdal, K.; Rasmussen, H. K.; Hassager, O. Elongational viscosity of narrow molar mass distribution polystyrene. *Macromolecules* **2003**, *36*, 5174-5179.
- (48) Huang, Q. When Polymer Chains Are Highly Aligned: A Perspective on Extensional Rheology. *Macromolecules* **2022**, *55*, 715–727.
- (49) Stadler, F. J.; Still, T.; Fytas, G.; Bailly, C. Elongational rheology and brillouin light scattering of entangled telechelic polybutadiene based temporary networks. *Macromolecules* **2010**, *43*, 7771-7778.
- (50) Sridhar, T.; Acharya, M.; Nguyen, D. A.; Bhattacharjee, P. K. On the extensional rheology of polymer melts and concentrated solutions. *Macromolecules* **2014**, *47*, 379-386.
- (51) Marrucci, G.; Ianniruberto, G. Interchain pressure effect in extensional flows of entangled polymer melts. *Macromolecules* **2004**, *37*, 3934-3942.
- (52) Ianniruberto, G.; Marrucci, G. Molecular dynamics reveals a dramatic drop of the friction coefficient in fast flows of polymer melts. *Macromolecules* **2020**, *53*, 2627-2633.

CHAPTER SIX

MOLECULAR INSIGHT INTO DYNAMICS OF SPARSE IONOMER NETWORKS

6.1 Abstract

Tethering ionizable groups to polymers drives formation of physical networks through ionic assemblies, resulting in macroscopic constraints on the motion of the macromolecules in melts and solutions. Resolving the molecular origin of this hindered dynamics, however, remains a critical fundamental challenge whose resolution would enhance control of processing of ionizable polymers. Here using quasi elastic neutron scattering accompanied by molecular dynamics simulations, segmental dynamics of slightly sulfonated polystyrene in solutions is studied as the ionic assemblies are tuned. We find that the ionic assemblies act of a center of confinement where in cyclohexane the chains are constrained in the vicinity of the ionic assemblies. Addition of small amount of ethanol affects the packing of the ionizable groups within the assemblies and in turn releases some of the confinement, enhancing dynamics.

6.2 Introduction

Ionizable groups tethered to polymers enable ion transport that in turn opens the way to a large number of lightweight energy technologies including clean energy generation and storage^{1, 2} as well as numerous biomedical applications.^{3, 4} The ionizable groups drive assembly of the polymers, determining their structure and dynamics, as well as their ion transport ability. Most notable is the immense impact even a small number of ionizable groups, tethered to the polymer, have on constraining the motion of the entire

chain.⁵⁻⁸ Though macroscopically these effects have been long demonstrated, particularly by rheology, the molecular origin of the constraints across length and time scales, critical to controlling the structure of these polymers through processing, remains unresolved. With low ionic content sulfonated polystyrene as a model system, the current study probes the segmental motion in a solution of cyclohexane as the dielectric constant of the solvent is tuned.⁹ We find that the polymer motion is hindered in the vicinity of the ionic assemblies, on the length scale of the Kuhn length, and a slight change in the solvent electrostatics is sufficient to affect the packing of the ionizable groups, which in turn enhances dynamics. These results provide new insight into a long-standing challenge with a direct impact on the processing of ionizable polymers.

Our study is set to resolve the molecular basis that underlines constraints of ionic assembly on segmental dynamics of ionizable polymers in solutions, using quasi elastic neutron scattering^{10, 11} (QENS), with insight from molecular dynamics simulations.¹² QENS captures the segmental motion of polymers on length scales of ca. 0.1-3 nm, on time scales from picoseconds to nanoseconds.¹³ The technique has been instrumental resolving constrained dynamics in a broad range of polymers and their complexes,¹⁴⁻¹⁸ including effects of the glass transition on segmental dynamics in melts as well as effects of confinement by nano particles.¹⁹ As the ionic clusters hinder the macroscopic motion of ionizable polymers^{8, 20-22} QENS has been used to probe dynamics in these systems. Early studies of sulfonated polystyrene (SPS) in the polyelectrolyte regime²³ and recent studies, in polymers in the semicrystalline practices ionomers^{24, 25} have demonstrated the ability of QENS to detect dynamics in these constrained systems. Further, the motion

detected has been directly correlated with macroscopic properties and transport characteristics of ionizable polymers.^{15, 16, 24-26}

With the long-standing issue of how a very small number ionic assemblies constrain macroscopic motion of polymer chains in melts and in solutions, the current study aims to understand the constraint dynamics on SPS with a low number of associative groups, in cyclohexane solutions, on a molecular level. SPS is a well-studied polymer particularly by rheology, providing a reference for comparison to macroscopic dynamics. In the dilute regime, SPS solutions offer a vehicle to understand the effects of confinement in the vicinity of the ionic assemblies, and enables fine tuning of the packing of the ionic groups through electrostatics.⁹

Specifically, SPS-cyclohexane solutions are studied as the temperature is varied across $T_{\theta} \sim 307\text{K}$ for the polystyrene (PS) backbone in cyclohexane.²⁷⁻²⁹ The study is carried out at concentrations above the overlap concentration for PS of the same molecular weight.³⁰ The ionic assemblies are perturbed by tuning the dielectric constant of the solution, through addition of small amounts of ethanol, a high dielectric constant solvent $\epsilon=24.5$ that is fully miscible in cyclohexane.

6.3 Materials and Methods

SPS with dispersity index of 1.04 and 3 mol% sulfonation in its acid form, synthesized by anionic polymerization, were purchased from Polymer Source Inc. Deuterated cyclohexane (d-cyclohexane), C_6D_{12} (D, 99.5%) and deuterated ethanol (d-ethanol), $\text{C}_2\text{D}_5\text{OD}$ (D, 99.0%), purchased from Cambridge Isotope Laboratories were used

as received. The solutions were prepared in d-cyclohexane (weight fraction of cyclohexane, $f_{cyh}=1.0$) and in d-cyclohexane:d-ethanol 95:5 w/w ($f_{cyh}=0.95$).

S(Q,E) measurements were made on BASIS, the backscattering silicon spectrometer¹³ at the Spallation Neutron Source, Oak Ridge National Laboratory. Q is the momentum transfer vector given by $Q = \frac{4\pi\sin\theta}{\lambda}$, λ is the neutron wavelength, θ is the incident angle, and E is energy. Spectra were collected using a band of polychromatic incident neutron beam with bandwidth centered at 6.4 Å. Scattered neutrons, with a wavelength of $\lambda_0 = 6.267$ Å, were Bragg-reflected by the Si (111) analyzer crystals, providing an energy transfer range of -100 to +100 µeV with a Q-averaged energy resolution of 3.5 µeV (Full width at half maximum). The data from multiple detectors were binned into six Q values, covering a Q range from 0.3 Å⁻¹ to 1.3 Å⁻¹. The stationary state was obtained by measuring each sample at 20 K for all Q values. This function includes the instrumental resolution as well as processes outside the dynamic instrumentation range, not captured by the background, and is used in data reduction as a reference for the sample with no motion. Data were collected for a temperature range of 300 K to 360 K. The temperature was controlled using a closed cycle refrigerator with helium gas as the refrigerant. All data were reduced using the Mantid platform³¹ and analyzed utilizing the DAVE³² package. The samples were enclosed in cylindrical aluminum cans with an insert providing 0.1mm thick sample, sealed with indium paste. The samples were weighed before and after measurements to ensure that no solvent evaporation occurred.

Neutron Analysis: Since the solvents are almost fully deuterated, the majority of the QENS incoherent signal originates predominantly from the hydrogen on SPS. The measured scattering intensity $I(Q, E)$, which includes the dynamic structure factor $S(Q, E)$ is given by

$$I(Q, E) = [p_1(Q)\delta(E) + (1 - p_1(Q))S(Q, E)] \otimes R(Q, E) + B(Q, E) \quad (6.1)$$

where $p_1(Q)$ is the elastic scattering contribution from the species that are immobile within the detection range of the instrument. The Dirac delta function $\delta(E)$ accounts for the elastic scattering signal at zero energy transfer. The signal is convoluted with the instrument resolution, $R(Q, E)$ and a background term, $B(Q, E)$, which accounts for the fast processes that are outside the dynamic range of the instrument.³³ The scattering contribution from the solvent was subtracted from the polymer solution for QENS data analysis.

Using DAVE,³² the data measured as $S(Q, E)$ were converted to $S(Q, \omega)$, where ω is the frequency ($E = \hbar\omega$) and convoluted with the Kohlrausch-Williams-Watt the KWW.³⁴ The overall function is given by

$$S_{KWW}(Q, E) = \frac{1}{2\pi} \int_{-\infty}^{\infty} \exp\left(\frac{iEt}{\hbar}\right) \exp\left(-\frac{t}{\tau(Q)}\right)^\beta dt \quad (6.2)$$

where t is time, β is a stretched exponential and τ is characteristic relaxation time, determined by the dynamics of the system. KWW has been successfully employed to capture coupled dynamics processes³⁴⁻³⁷ in numerous polymeric systems.

The time average relaxation time is calculated by $\langle \tau(Q) \rangle = \left(\frac{\tau(Q)}{\beta} \right) \Gamma \left(\frac{1}{\beta} \right)$ where Γ is the Gamma-function at a particular value of β .³⁵ It is inversely proportional to the dynamic processes in the system. The effective diffusion constant D_{eff} is calculated by $\langle \tau(Q) \rangle = \frac{1}{D_{eff} Q^2}$ in Q range that follows Q^2 .

6.4 Results and discussion

The dynamic structure factor $S(Q,E)$ was measured in SPS cyclohexane solutions, over a Q range of $0.3 \leq Q \leq 1.3 \text{ \AA}^{-1}$, corresponding to dimensions of 4.8 \AA to 21 \AA . The results at 300 K are presented in Figure 6.1a, together with the same data, normalized to $I_{max}(Q)$ in Figure 6.1b.

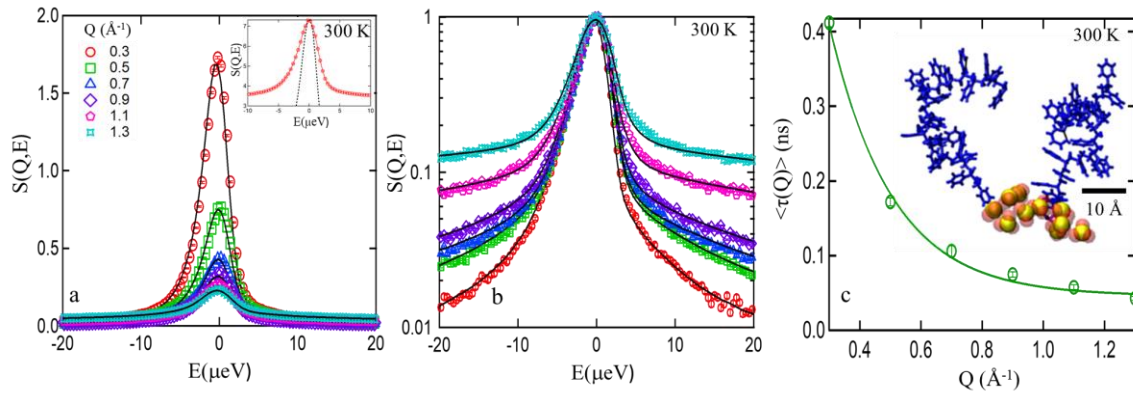


Figure 6.1: a) $S(Q,E)$ as a function of energy E for a 10wt% solution of SPS with 3 mol% random sulfonation in cyclohexane at $T=300 \text{ K}$ at the indicated Q values. The insert presents a representative resolution function superimposed with the data at 300 K at $Q=0.3 \text{ \AA}^{-1}$. b) the same data as in (a), normalized by $I_{max}(Q)$. The solid black lines correspond to KWW fits. (c) $\langle \tau(Q) \rangle$ extracted from KWW fits as function of Q . The solid line is a guide to the eye. The insert captures a representative ionic cluster tethered to representative SPS chains obtained by molecular dynamics simulation.³⁸

With increasing Q , the spectral lines initially rapidly broaden, followed by a slower increase of the linewidth. To analyze the data, a sum of two simple exponentials, corresponding to a slow and a fast motion, was first attempted, in line with the fact that ionizable polymers are confined by the formation of the ionic clusters, thus constitute a confined and a non-confined reions.¹⁹ However, this model was not able to capture the multitude of segmental dynamics in the entire measured Q range. The data are thus analyzed in terms of a stretched exponential, using the KWW³⁴ function. The results are noted by the solid lines in Figure 6.1a and b and the average relaxation times, calculated from this analysis, are plotted in Figure 6.1c. The values of β obtained from the fit are between 0.7 to 0.8 and fluctuate within 5% error for all measurements. At low Q the average relaxation times decrease rapidly with increasing Q up to $\sim 0.8 \text{ \AA}^{-1}$, and plateau at higher Q . The low Q region captures dimensions smaller than $\sim 20 \text{ \AA}$ and cross over to a plateau region at $\sim 10 \text{ \AA}$. These dimensions are slightly smaller than the interionic assembly correlations commonly observed by SAXS for similar systems^{39, 40} and the cross over occurs at the Kuhn length of PS. These dimensions suggest that the slower dynamics in these low sulfonation levels arise in part to confinement of the chains to the ionic assemblies.

With increasing temperature from 300 K to 360 K, across $T_{\theta} \sim 307 \text{ K}$ for PS, the system becomes more dynamic for all Q values measured as manifested in the line broadening, shown in Figure 6.2.

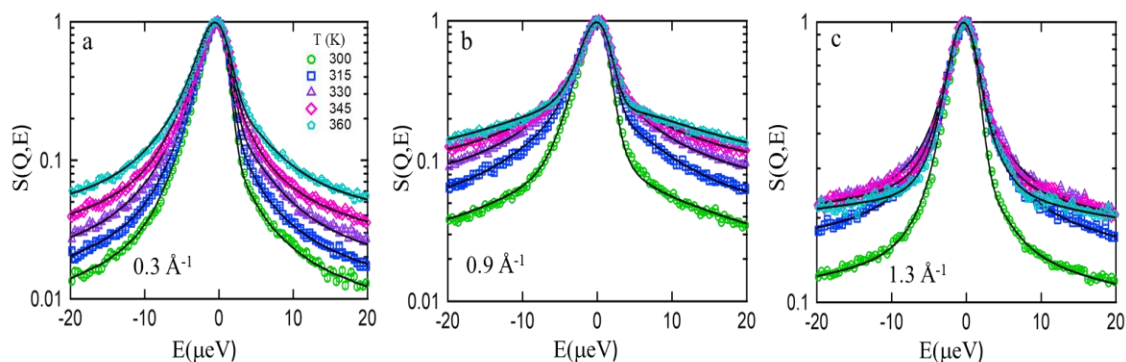


Figure 6.2: $S(Q, E)$ as a function of energy E for SPS in cyclohexane at the indicated three Q values and temperatures. The solid lines correspond to KWW fits.

However, the temperature dependence of the spectral line shape depends on Q . While at low Q (Figure 6.2a), the linewidth increases gradually with increasing temperature, where at the highest Q measured (1.3 \AA^{-1}), the spectra below and above T_θ exhibit notably different line shapes. At the intermediate Q range, where segmental motion is coupled to that of the ionic assembly, the temperature response is similar to that of the high Q region but is distinguished at lower temperatures.

The average relaxation times, extracted from the analysis, are shown in Figure 6.3a. $\langle \tau(Q) \rangle$ decrease with increasing temperature for all Q values, but do not follow an Arrhenius behavior. A clear distinction, observed between the low and the high Q regions, is attributed to the degree of confinement of the chains to the ionic assemblies. At lower Q values, the measurements mostly capture the correlated segmental motion that is relatively non-constrained, and the polymer chain motion is coupled with that of the solvent. In this range, temperature effects are relatively small and are coupled to the viscosity of the

solvent that constitute 90% of the network. At low Q values, however, while the energy associated with the increase in temperature is not enough to dissociate the ionic assemblies, the clusters become internally more dynamics, affecting segmental dynamics.

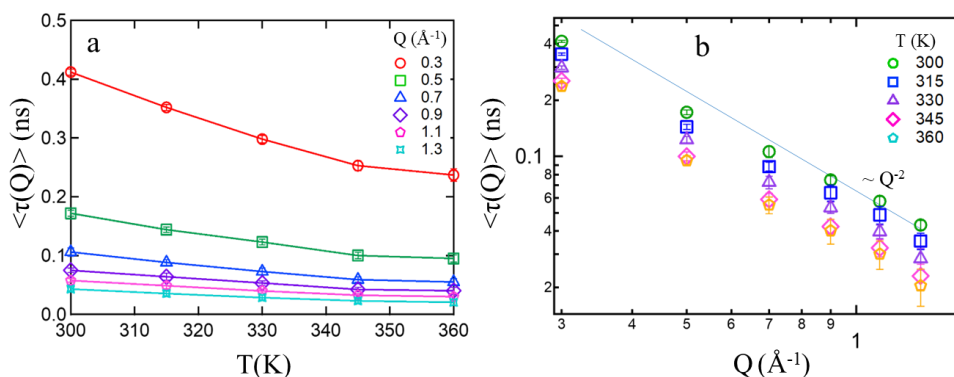


Figure 6.3: Average relaxation times $\langle\tau(Q)\rangle$ as a function of (a) temperature and (b) Q at the indicated temperatures.

The results presented in Figure 6.3a distinctly show that the temperature response of the system depends on the length scale measured. The Q dependence of $\langle\tau(Q)\rangle$ at different temperatures is shown in Figure 6.3b. At high Q values, all curves follow Q^{-2} with a cross over to a lower exponent, at ~ 0.7 - 0.9 \AA^{-1} . At higher Q values the Q^{-2} dependence is indicative of diffusive motion whereas the lower exponent at the ionic cluster length scale, at low Q , corresponds to constrained dynamics. As the chains are confined to the ionic assemblies, some similarities are noted with the dynamics of polymers confined to nanoparticles.¹⁹ In contrast however, the clusters often bridge between different chains, even at these low sulfonation levels,^{38, 41} adding an additional constraint, as observed in rheological studies.⁶⁻⁸

The clusters were then perturbed through adding 5 wt% ethanol to the cyclohexane solutions, tweaking the dielectric environment of the solution. Ethanol is a polar solvent

with a dielectric constant $\epsilon = 24.5$ and is miscible in cyclohexane. The ability of ethanol to affect the clustering in SPS melts has been previously demonstrated by small angle X-ray measurements⁴² and molecular dynamics simulations.⁹ QENS spectra of SPS in cyclohexane-ethanol solution, in comparison with those of the polymer in cyclohexane, are shown in Figure 6.4 for representative Q values at 300 and 360 K.

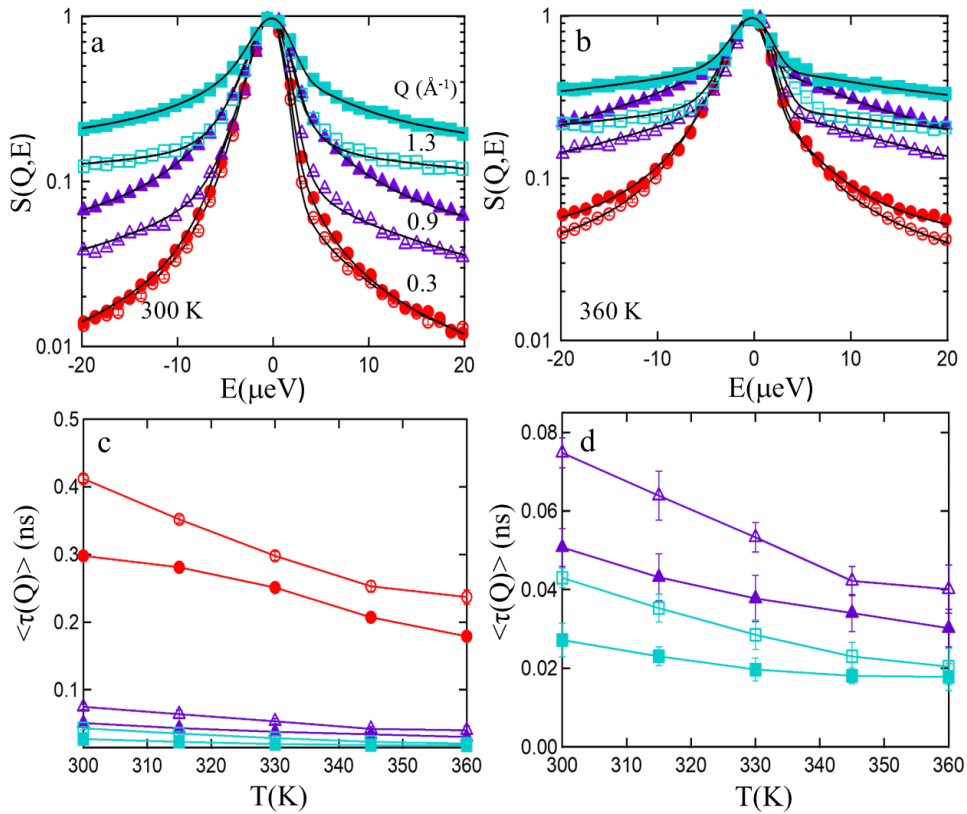


Figure 6.4: $S(Q, E)$ as a function of energy E for SPS in $f_{\text{cyl}} = 1.0$ (open symbols) solutions, and $f_{\text{cyl}} = 0.95$ solutions (bold symbols) at (a) 300 K and (b) 360 K at indicated Q values. The solid line corresponds to KWW fits. (c) Average relaxation times, $\langle \tau(Q) \rangle$ as a function of T for the three Q values presented in a following the same color code as for a. (d) Zooming into the low $\langle \tau(Q) \rangle$ region of Figure 6.4c, with y axis ranging from 0 to 0.085 ns.

For all Q values measured, the lines broaden with addition of ethanol, pointing to enhanced dynamics. The average relaxation times decrease (i.e., the dynamics increases) with increasing temperature as shown in Figure 6.4c. While the dynamics increase in presence of ethanol across the entire Q range, the effects are more pronounced at low Q . Further, the dependence of $\langle \tau(Q) \rangle$ in the presence of ethanol is more pronounced in comparison with those of just cyclohexane.

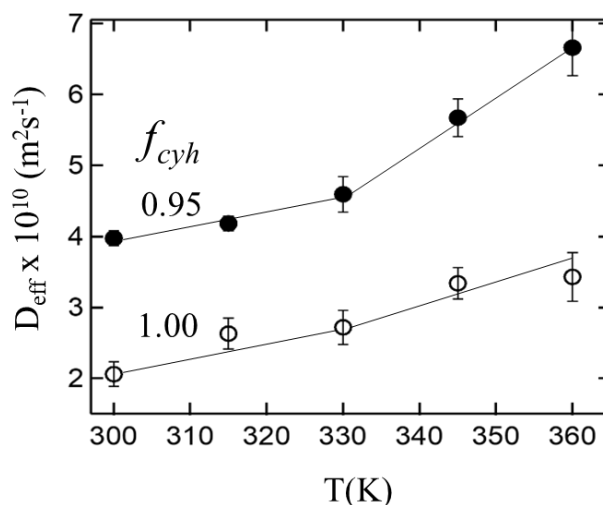


Figure 6.5: D_{eff} as a function of temperature for cyclohexane-ethanol fractions.

The effective diffusion constant D_{eff} , associated with the dynamics on the length scale measured, was extracted from the Q range where the average relaxation times scale with Q^{-2} . The effective diffusion constants D_{eff} is calculated by $\langle \tau(Q) \rangle = \frac{1}{D_{eff}Q^2}$ are shown in Figure 6.5. The characteristic motion is faster in ethanol-cyclohexane solutions compared with cyclohexane only. D_{eff} increases with temperature across the entire temperature range for both solutions where at higher temperatures, it changes faster in

presence of ethanol. This enhancement is attributed to penetration of the ethanol into the ionic assemblies, reducing the overall confinement.

These QENS results clearly demonstrated two dynamics regimes. With the persistence length of polystyrene of ~ 1 nm,⁴³ 2 nm, the largest dimension probed by the QENS measurements, constitute the dimensions around an ionic assembly in which a tethered chains is confined. Below this length, bonds and short segments remain dynamic and coupled with the solvent. As the ionic assemblies were tweaked by the presence of ethanol, the polymer becomes more dynamic. This raises new questions regarding the origin of this enhanced motion. Additional molecular insights attained by molecular dynamics simulations that were carried out on similar solutions as QENS.³⁸ With a solution containing ~ 2.9 million atoms and 148 randomly sulfonated SPS chains (molecular weight $\sim 11,000$ g/mol) with sulfonation level 3% with Na^+ as the counter ion (rather than the acid form for the QENS studies). Note that both the acid form and the sodium form of SPS have been studied,³⁸ and both form aggregates, where the degree of condensation of the counterions slightly varies. The all atoms optimized potential for liquid simulations (OPLS-AA) force fields were used to model the system,^{44, 45} at $T=300$ K and pressure of 1 bar. All simulations were run in GROMACS.⁴¹ Visualization of one representative ionic assembly, or a cluster together with 2 representative chains tethered to these sulfonated groups, are shown in Figure 6.6a, at 2 ns intervals for both cyclohexane and cyclohexane/ethanol solutions. Visually, in the vicinity of the ionic assembly, hardly any changes are observed. This is consistent with the QENS results at $Q = 0.3 \text{ \AA}^{-1}$. On the other hand, visualized chain segments that are not directly tethered within the Kuhn length of the

polymer to an ionic assembly are significantly less constraint. These results suggest that tethering to an ionic assembly is sufficient to decrease the dynamics of the chains.

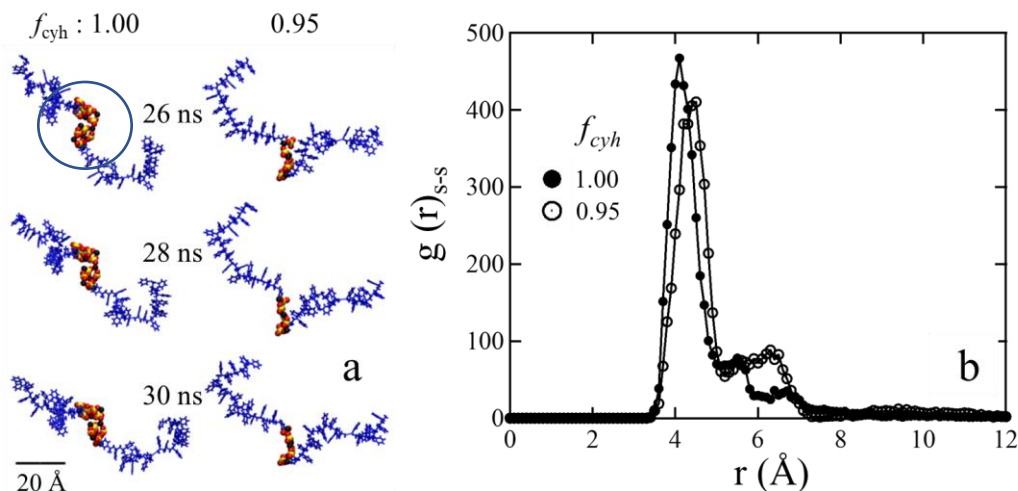


Figure 6.6: Snapshots of a cluster for SPS in (a) $f_{cyh} = 1.00$ and 0.95 at 2 ns intervals. Sulfur is yellow, oxygen is red, sodium is black, and the backbone is blue. (b) Sulfur–sulfur radial distribution function for corresponding system.

The addition of ethanol changes the shape of the clusters and introduces internal degree of freedom that in turn enhances the dynamics of the chains. The changes in internal packing within the ionic assemblies are manifested in the pair correlation function $g(r)$ between the sulfur groups as shown in Figure 6.6b. The second and third signatures are significantly different between the two solutions, in agreement with visual observations that show rearrangements of the ionic groups. Yet these slight differences are sufficient to affect the dynamics pointing to the direct confinement of the chains to the ionic assemblies.

Bridging between clusters strongly affects dynamics in SPS melts.⁴¹ The degree of bridging is reflected in the number of unique chains that participate in the ionic clusters, where

clusters that consist of ionizable groups from distinctive chains, are more likely to constrain chain dynamics.

6.5 Conclusions

Quasi-elastic neutron scattering is used to study segmental dynamics of lightly sulfonated polystyrene solutions in cyclohexane, followed by tracking the polymer motion as the ionic assemblies were perturbed by ethanol. Surprisingly, 3% sulfonation in these solutions below the entanglement length of PS in cyclohexane reduces the mobility of the polymer chains, at large length scales, but smaller than the length scale of the correlation between the ionic assemblies. In contrast, on shorter length scales, the segments remain dynamic.

We find that with some of the chains bridging between the ionic assemblies, a very sparse network is formed affecting the motion of the polymer. Addition of ethanol enhances the dynamics on all the length scales captured in the QENS measurements. Ethanol affects the packing of the ionizable assemblies, introducing freedom by decreasing the chain constraints.

The results provide new fundamental understanding of the inter-relation of ionic cluster cohesion and chain dynamics. These will in turn, impact ionizable polymer processing that determine device integrity and performance.

6.6 Acknowledgments

We kindly acknowledge DOE grant DE-SC0019284 for support. Work at ORNL's Spallation Neutron Source was sponsored by the Scientific User Facilities Division, Office of Basic Energy Sciences, U.S. Department of Energy. Oak Ridge National Laboratory is

managed by UT-Battelle, LLC, for U.S. DOE under Contract No. DEAC05-00OR22725. This research used resources of the National Energy Research Scientific Computing Center (NERSC), a U.S. Department of Energy Office of Science User Facility located at Lawrence Berkeley National Laboratory, operated under Contract No. DE-AC02-05CH11231 using NERSC award BES-ERCAP-20938. This work was performed, in part, at the Center for Integrated Nanotechnologies, an Office of Science User Facility operated for the U.S. Department of Energy (DOE) Office of Science by Los Alamos National Laboratory (Contract 89233218CNA000001) and Sandia National Laboratories (Contract DE-NA-0003525). We kindly acknowledge invaluable discussions with Gary S. Grest of Sandia National Laboratories.

6.7 References

- (1) Adhikari, S.; Pagels, M. K.; Jeon, J. Y.; Bae, C. Ionomers for electrochemical energy conversion & storage technologies. *Polymer* **2020**, 123080.
- (2) Farzin, S.; Johnson, T. J.; Chatterjee, S.; Zamani, E.; Dishari, S. K. Ionomers From Kraft Lignin for Renewable Energy Applications. *Front. Chem.* **2020**, 8, 690.
- (3) Zinjad, P.; Gondhale, P.; Kulkarni, S.; Musmade, B.; Bhope, S.; Padmanabhan, S. Development and validation of HPLC-UV method for the quantitative analysis of carcinogenic organic impurities and its isomers in the sodium polystyrene sulfonate polymer. *Acta Chromatographica* **2021**, 33, 162-169.

- (4) Singh, V. R.; Pandey, S. P.; Singh, P. K. Poly (styrene-sulfonate) hosted Thioflavin-T aggregates: A turn-on and ratiometric sensing platform for ATP recognition. *Dyes and Pigments* **2021**, *194*, 109577.
- (5) Colby, R.; Zheng, X.; Rafailovich, M.; Sokolov, J.; Peiffer, D.; Schwarz, S.; Strzhemechny, Y.; Nguyen, D. Dynamics of lightly sulfonated polystyrene ionomers. *Phys. Rev. Lett.* **1998**, *81*, 3876.
- (6) Weiss, R.; Yu, W.-C. Viscoelastic behavior of very lightly sulfonated polystyrene ionomers. *Macromolecules* **2007**, *40*, 3640-3643.
- (7) Weiss, R.; Fitzgerald, J.; Kim, D. Viscoelastic behavior of lightly sulfonated polystyrene ionomers. *Macromolecules* **1991**, *24*, 1071-1076.
- (8) Qiao, X.; Weiss, R. Nonlinear rheology of lightly sulfonated polystyrene ionomers. *Macromolecules* **2013**, *46*, 2417-2424.
- (9) Agrawal, A.; Perahia, D.; Grest, G. S. Clustering effects in ionic polymers: Molecular dynamics simulations. *Phys. Rev. E* **2015**, *92*, 022601.
- (10) Sakai, V. G.; Arbe, A. Quasielastic neutron scattering in soft matter. *Current Opinion in Colloid & Interface Science* **2009**, *14* (6), 381-390.
- (11) Osti, N.; Etampawala, T.; Shrestha, U.; Aryal, D.; Tyagi, M.; Diallo, S.; Mamontov, E.; Cornelius, C.; Perahia, D. Water dynamics in rigid ionomer networks. *The Journal of chemical physics* **2016**, *145* (22), 224901.
- (12) Agrawal, A.; Perahia, D.; Grest, G. S. Cluster morphology-polymer dynamics correlations in sulfonated polystyrene melts: computational study. *Phys. Rev. Lett.* **2016**, *116*, 158001.

- (13) Mamontov, E.; Herwig, K. W. A time-of-flight backscattering spectrometer at the Spallation Neutron Source, BASIS. *Review of Scientific Instruments* **2011**, *82*, 085109.
- (14) Kanaya, T.; Kawaguchi, T.; Kaji, K. Fast process of amorphous polystyrene below and above the glass transition temperature T_g as studied by quasielastic neutron scattering. *The Journal of chemical physics* **1996**, *104* (10), 3841-3850.
- (15) Mongcopa, K. I. S.; Tyagi, M.; Mailoa, J. P.; Samsonidze, G.; Kozinsky, B.; Mullin, S. A.; Gribble, D. A.; Watanabe, H.; Balsara, N. P. Relationship between segmental dynamics measured by quasi-elastic neutron scattering and conductivity in polymer electrolytes. *ACS Macro Letters* **2018**, *7* (4), 504-508.
- (16) Mongcopa, K. I. S.; Gribble, D. A.; Loo, W. S.; Tyagi, M.; Mullin, S. A.; Balsara, N. P. Segmental Dynamics Measured by Quasi-Elastic Neutron Scattering and Ion Transport in Chemically Distinct Polymer Electrolytes. *Macromolecules* **2020**, *53* (7), 2406-2411.
- (17) Yasuda, Y.; Hidaka, Y.; Mayumi, K.; Yamada, T.; Fujimoto, K.; Okazaki, S.; Yokoyama, H.; Ito, K. Molecular dynamics of polyrotaxane in solution investigated by quasi-elastic neutron scattering and molecular dynamics simulation: sliding motion of rings on polymer. *Journal of the American Chemical Society* **2019**, *141* (24), 9655-9663.
- (18) Arrighi, V.; Gagliardi, S.; Zhang, C.; Ganazzoli, F.; Higgins, J. S.; Ocone, R.; Telling, M. T. A unified picture of the local dynamics of poly (dimethylsiloxane) across the melting point. *Macromolecules* **2003**, *36* (23), 8738-8748.
- (19) Sharma, A.; Kruteva, M.; Zamponi, M.; Ehlert, S.; Richter, D.; Förster, S. Influence of molecular weight on the distribution of segmental relaxation in polymer grafted nanoparticles. *Physical Review Materials* **2022**, *6* (1), L012601.

- (20) Ling, G. H.; Wang, Y.; Weiss, R. Linear viscoelastic and uniaxial extensional rheology of alkali metal neutralized sulfonated oligostyrene ionomer melts. *Macromolecules* **2012**, *45*, 481-490.
- (21) Huang, C.; Chen, Q.; Weiss, R. Rheological behavior of partially neutralized oligomeric sulfonated polystyrene ionomers. *Macromolecules* **2017**, *50*, 424-431.
- (22) Weiss, R.; Zhao, H. Rheological behavior of oligomeric ionomers. *J. Rheol.* **2009**, *53*, 191-213.
- (23) Nallet, F.; Jannink, G.; Hayter, J.; Oberthür, R.; Picot, C. Observation of the dynamics of polyelectrolyte strong solutions by quasi-elastic neutron scattering. *J. Phys. Chem* **1983**, *44*, 87-99.
- (24) Middleton, L. R.; Tarver, J. D.; Cordaro, J.; Tyagi, M.; Soles, C. L.; Frischknecht, A. L.; Winey, K. I. Heterogeneous chain dynamics and aggregate lifetimes in precise acid-containing polyethylenes: Experiments and simulations. *Macromolecules* **2016**, *49*, 9176-9185.
- (25) Frischknecht, A. L.; Paren, B. A.; Middleton, L. R.; Koski, J. P.; Tarver, J. D.; Tyagi, M.; Soles, C. L.; Winey, K. I. Chain and ion dynamics in precise polyethylene ionomers. *Macromolecules* **2019**, *52*, 7939-7950.
- (26) Sinha, K.; Maranas, J. K. Segmental dynamics and ion association in PEO-based single ion conductors. *Macromolecules* **2011**, *44*, 5381-5391.
- (27) Raziell, A.; Eisenberg, H. Excluded Volume Study of Potassium Polystyrenesulfonate-Potassium Chloride Solutions. *Israel Journal of Chemistry* **1973**, (2-3), 183-199.

- (28) Kosgallana, C.; Wijesinghe, S.; Senanayake, M.; Mohottalalage, S.; He, L.; Perahia, D. Solvent Effects on the Structure of Sulfonated Polystyrene Networks (in preparation). **2022**.
- (29) Wei, Y.; Hore, M. J. Characterizing polymer structure with small-angle neutron scattering: A Tutorial. *Journal of Applied Physics* **2021**, *129* (17), 171101.
- (30) Nyström, B.; Roots, J.; Higgins, J.; Gabrys, B.; Peiffer, D.; Mezei, F.; Sarkissian, B. Dynamics of polystyrene sulfonate ionomers in solution. A neutron spin-echo study. *J. Polym. Sci., Part C: Polym. Lett.* **1986**, *24*, 273-281.
- (31) Arnold, O.; Bilheux, J.-C.; Borreguero, J.; Buts, A.; Campbell, S. I.; Chapon, L.; Doucet, M.; Draper, N.; Leal, R. F.; Gigg, M. Mantid—Data analysis and visualization package for neutron scattering and μ SR experiments. *Nucl. Instrum. Methods Phys. Res. A: Accel. Spectrom. Detect. Assoc. Equip.* **2014**, *764*, 156-166.
- (32) Azuah, R. T.; Kneller, L. R.; Qiu, Y.; Tregenna-Piggott, P. L.; Brown, C. M.; Copley, J. R.; Dimeo, R. M. DAVE: a comprehensive software suite for the reduction, visualization, and analysis of low energy neutron spectroscopic data. *J. Res. Natl. Inst. Stand. Tech.* **2009**, *114*, 341.
- (33) Chen, X. C.; Sacci, R. L.; Osti, N. C.; Tyagi, M.; Wang, Y.; Keum, J. K.; Dudney, N. J. Study of the segmental dynamics and ion transport of solid polymer electrolytes in the semi-crystalline state. *Frontiers in Chemistry* **2020**, *8*.
- (34) Williams, G.; Watts, D. C. Non-symmetrical dielectric relaxation behaviour arising from a simple empirical decay function. *Transactions of the Faraday society* **1970**, *66*, 80-85.

- (35) Mamontov, E.; Mahurin, S. M.; Dai, S. Comparative microscopic dynamics in a room-temperature ionic liquid confined in carbon pores characterized by reversible and irreversible ion immobilization. In *AIP Conference Proceedings*, 2018; AIP Publishing LLC: Vol. 1969, p 020001.
- (36) Osti, N. C.; Cote, A.; Mamontov, E.; Ramirez-Cuesta, A.; Wesolowski, D.; Diallo, S. Characteristic features of water dynamics in restricted geometries investigated with quasi-elastic neutron scattering. *Chem. Rev.* **2016**, *465*, 1-8.
- (37) Bée, M. Quasielastic neutron scattering. **1988**.
- (38) Kosgallana, C.; Grest, G.; Perahia, D. Effect of Solvent Dielectrics on the Structure and Dynamics of Ionomers (in preparation). **2022**.
- (39) Peiffer, D.; Weiss, R.; Lundberg, R. Microphase separation in sulfonated polystyrene ionomers. *J. Polym. Sci. : Polym. Phys.* **1982**, *20*, 1503-1509.
- (40) Kirkmeyer, B. P.; Weiss, R. A.; Winey, K. I. Spherical and vesicular ionic aggregates in Zn-neutralized sulfonated polystyrene ionomers. *J. Polym. Sci. B Polym. Phys.* **2001**, *39*, 477-483.
- (41) Mohottalalage, S. S.; Aryal, D.; Thurston, B. A.; Grest, G. S.; Perahia, D. Effects of Ionic Group Distribution on the Structure and Dynamics of Amorphous Polymer Melts. *Macromolecules* **2021**, *55*, 217–223.
- (42) Fitzgerald, J.; Kim, D.; Weiss, R. The effect of diluents on the ionic interactions in sulfonated polystyrene ionomers. *J. Polym. Sci., Part C: Polym. Lett.* **1986**, *24*, 263-268.

- (43) Wignall, G.; Ballard, D.; Schelten, J. Measurements of persistence length and temperature dependence of the radius of gyration in bulk atactic polystyrene. *European Polymer Journal* **1974**, *10* (9), 861-865.
- (44) Jorgensen, W. L.; Maxwell, D. S.; Tirado-Rives, J. Development and testing of the OPLS all-atom force field on conformational energetics and properties of organic liquids. *J. Am. Chem. Soc.* **1996**, *118*, 11225-11236.
- (45) Aryal, D.; Perahia, D.; Grest, G. S. *Conformation of Single Pentablock Ionomer Chains in Dilute Solutions*; Sandia National Lab.(SNL-NM), Albuquerque, NM (United States), 2015.

CHAPTER SEVEN

MULTI-CHAIN POLYMER NANOPARTICLES: MOLECULAR DYNAMICS SIMULATION STUDIES

7.1 Abstract

Conjugated polymers confined into nano dimensions form long lived, far-from equilibrium luminescent nanoparticles, often referred to as “polydots”. Polydots are emerging as a promising tool for intra cellular imaging. The photo-physics of polydots strongly depends on chain conformation and the size of the polydot. Using fully atomistic molecular dynamics (MD) simulations, polydots formed by multiple chains of dialkyl poly(para-phenylene ethynylene)s (PPEs) as the alkyl chain length was varied were studied. We find that the number of chains N , affects the size of the polydots, as expected. However, the overall conformation of the molecule is only slightly affected. For all N , the chain ends reside at the polydots’ interface. With increasing temperature, the polydots transform from a spherical NPs to elongated one, with a distinctive transition temperature that depends on the length of the alkyl chains. The autocorrelation function between the aromatic rings demonstrates that PPE backbones exhibits glass-like dynamics with relaxation times in a range of microseconds.

7.2 Introduction

Soft nanoparticles (NPs) are often formed by spontaneous assemblies of molecules. Examples include liposomes, micelles, dendrimers, and polymer-drug hybrids. Most NPs are potential for drug delivery,¹⁻⁵ imaging, as well as sensing probes⁶⁻¹² because of their adaptive nature. Merging the inherent luminescence of conjugated polymers and their elasticity, with the unique response of soft nanoparticles presents a highly tunable platform that could impact nanomedicine. Collapsing luminescent polymers into soft nanoparticles often referred to as conjugated nanoparticles (CPNS), or polydots, without additional chemical cross links offers further responsiveness to trigger functionality. These NPs however, form far from equilibrium nano structures whose properties depend on their preparation.¹³⁻¹⁷ The internal conformation of the polymer chains and their interactions with their immediate environment determines both their photo-physics and their mechanical behavior. Despite their potential, only limited understanding is currently accessible on the folding of macromolecules into long lasting NPs without chemical crosslinks, where the surface area to volume ratio is a critical factor. The energetics that hold together these polymeric NPs¹⁸⁻²⁴ remain an open question, critical to transform the lab concept to an actual usable marker.

The current study probes the effects of molecular parameters on the shape and stability of the polydots formed by dialkyl poly(para-phenylene ethynylene)s (PPE), and the chemical formula is shown in Figure 7.1, using molecular dynamics simulations (MD). Building on the knowledge available for a single polymer polydots this study provide

insight to the conformation of the PPE chain in a state that bare the characteristics of the actual NPs.

Experimentally polydots are made by nano precipitation. The polymer is dissolved in a good solvent such as THF where the polymer is fully soluble, below the critical micellar concentration, followed by dripping the solution into a poor solvent (water) under vigorous stirring (sonication).^{23, 24} As the good solvent evaporates, the polymer collapse into long lived assemblies on the nano dimensions. These particles are of ~10-100 nm in diameter depending on the polymer concentration in the parent solution. They remain stable as isolated particles in low concentrations with a shelve life of more than a year. These polydots consist of several polymers, and their size often depends on several preparation parameters.

The photo-physics of these NPs differs significantly from that of spontaneously formed aggregates of conjugated polymers.^{24, 25} The differences in the emissive characteristics is attributed to the distinctive conformation the polymer chains assumes in these NP, which differs from that in spontaneously assembled films.¹⁹⁻²¹ Direct measurements of chain conformation within a polydot in these low concentration-small dimensions in solutions presents a challenge. Molecular dynamics simulations are well suited to probe the conformation and dynamics of the polymers.

The first computational insight into the structure of polydots was obtained by Maskey et al.^{18, 26} for single chain PPE confined into nano dimensions, demonstrating the impact of molecular parameters on the overall conformation and stability of the polydots. Further, these studies have shown that the polymer backbone exhibits slow dynamics,

typical of a glassy behavior.^{18,26} Building on the knowledge previously obtained, we probe the factors that control the structure and stability of multiple chains polydots consisting of di-alkyl PPEs as the number of chains confined into the NPs, and their relative initial orientation are varied while the alkyl chain length is controlled.

Polydots that consist of multiple chains capture the interchain correlations and entropy that affect the properties of these NPs. The orientation of the di-alkyl PPEs in solutions has been probed since these polymers form lyotropic liquid crystals in relatively low concentrations,^{27, 28} where the degree of liquid crystallinity depends on the polymer chain length. Di-alkyl PPE assume extended conformation in solutions²⁹ where the backbone on its own is hardly soluble in most common solvents, and the side alkyl chains often control the interaction of the PPEs with neighboring molecules.³⁰⁻³² Thus the alkyl side chains length is expected to affect the internal interactions and dynamics of the NPs.

7.3 Model and Simulation Methods

The PPE chains were build using the polymer builder in Material Studio from BIOVIA™ with the Polymer Consistent Force Field (PCFF). An in-house conversion code is used to convert PCFF to Optimized potentials for liquid simulations-all atoms (OPLS-AA) and was used to model PPEs fully atomistic.^{30, 31} The PPE chains were equilibrated in an implicit good solvent.

All simulations were carried out using the large-scale atomic/molecular massively parallel simulator (LAMMPS)³² molecular dynamics code with a time step of 1 fs. Long range electrostatic interactions were calculated with particle-particle particle-mesh

algorithm (PPPM)³³ Ewald with a real space cutoff of 1.2 nm and a precision of 10^{-4} Kcal mol⁻¹ Å⁻¹. All simulations employed a Langevin thermostat^{34, 35} to regulate the temperature with a damping constant of 100 fs. The quality of implicit solvents was controlled by varying the strength of the attractive interactions between non-bonded atoms. To model a poor solvent for both the backbone and side chains,^{19, 20} all Lenard-Jones nonbonded interactions are truncated at $r_c = 1.2$ nm, while to model a good solvent, the potential was truncated so that they were purely repulsive.

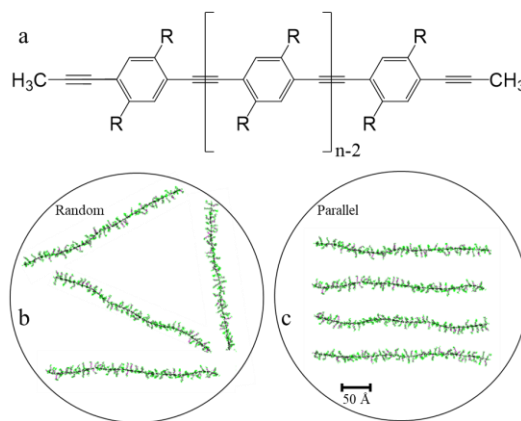


Figure 7.1: (a) the chemical structure of PPE where R corresponds for an alkyl side chain. Preparation of a polydot from (b) random and (c) parallel-chain orientation. Purple corresponding to carbon atoms on the side chains, black to all atoms on the backbone and green to hydrogen atoms.

Two starting states were studied, randomly orientated chains and parallel to each other as shown in Figure 7.1. Studies were carried out along two lines: changing the number of N with $N = 2, 4$ and 6 PPE chains were built with 240 total monomers or a total of 15880 atoms for dinonyl PPE polydots. The side chain length was then varied with the number of carbon atoms $l = 6, 9, 12$ and 18 in the dialkyl side chains for polydots made of 2 chains of length $n = 120$ with a random starting orientation. The number of atoms in each

polydot is 11540, 15880, 20180 and 28820 for $l = 6 - 18$, respectively. All side chains are methyl terminated.

Experimentally, polydots are prepared by using nano precipitation. The polymer dissolved in a good solvent, followed by dripping the solution into a poor solvent under sonication.²¹ The polymers confined into nanoparticles as the good solvent evaporates and remain suspended in the poor solvent, where the size of the droplets form practically a In simulations, a harmonic potential cavity is used (*fix indent* command) whose diameter is slowly reduced over 5 ns until the density of the polydot reaches its bulk value. The cavity is then removed and the compressed polydots are allowed to relax for 120 ns in an implicit poor solvent with dielectric constant of 77.3 which mimics water. The size of polydots were monitored as the simulation progressed. After approximately 25 ns, the average radius of gyration $\langle R_g^2 \rangle = \frac{\sum_{i=1}^n m_i (r_i - r_{com})^2}{\sum_{i=1}^n m_i}$ reached a steady state with $\langle R_g^2 \rangle^{1/2} \approx 3.3$ nm. All results are averaged over times from 25 to 120 ns.

7.4 Results

The temperature response of backbone for dinonyl PPE polydots with increasing number of chains is shown in Figure 7.2 for random and parallel initial orientation. At 300K all polydots are spherical independent of the number of chains or their initial orientation. No obvious internal correlations are observed. However, the chain ends reside at the interface. Segregation of chain end to the air interface is typical to thin polymeric films where the entropy drive segregation to the interface.^{36, 37} With increasing T , all the polydots expand but remain spherical for temperature up to ~ 500 K, above which the

polydots begin to unravel and become aspherical at 600 K as shown in Figure 7.2(c).

Throughout this process, the chain ends remain at the interface.

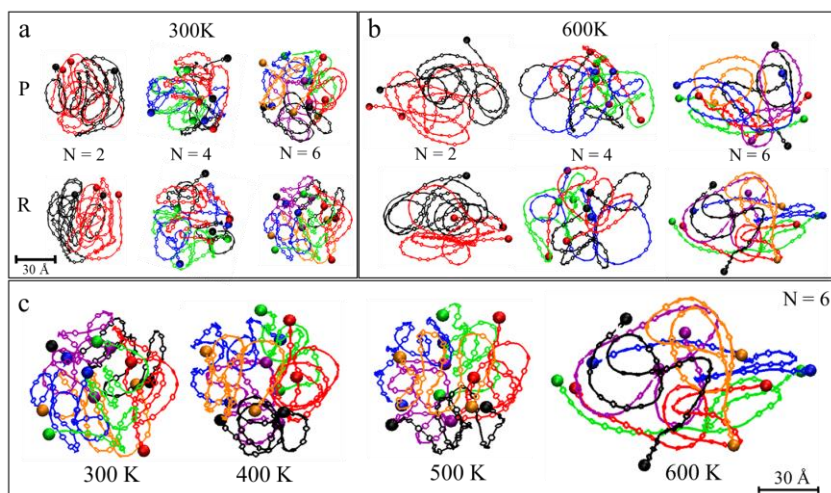


Figure 7.2: Visualization of backbones for dinonyl PPE polydots at the (a) 300K and (b) 600K with $N = 2, 4$ and 6-chains after 120 ns for initial parallel (P) and random (R) orientation. (c) at 300K, 400K, 500K and 600K for random $N = 6$ -chains. Confined 1st (red), 2nd (black), 3rd (green), 4th (blue), 5th (orange) and 6th (purple) chains are colored distinctly. The chain ends are represented by an enlarged sphere and colored accordingly.

Similar trends were observed by Maskey and coworkers¹⁸ for single chain diethylhexyl PPE polydots and persists for multichain PPEs. Here, three main factors play a role in unraveling of the polydots including the drive to achieve the elongated conformation of the backbone that is the inherent thermodynamic stable conformation²⁹, the enhanced entropy of the end groups at the surface and the interrelation between segments detected by the substituting side chains.

Table 7.1: Moment of inertia tensor eigenvalues ($\lambda_1, \lambda_2, \lambda_3$) and sphericity $A(a_1, a_2, a_3)$ for polydots with 2-, 4-, and 6-chains at indicated temperatures for parallel (P) and random (R) starting chain orientations.

2-chains P	300 K	400 K	500 K	600 K
λ_1	288.3±0.1	302.5±0.2	317.9±0.1	380.1±0.1
λ_2	317.1±0.1	332.75±0.2	381.48±0.1	760.2±0.2
λ_3	345.9±0.2	363.0±0.1	445.1±0.1	798.2±0.1
A	0.00069	0.00070	0.0023	0.012

2-chains R	300 K	400 K	500 K	600 K
λ_1	291.0±0.1	305.8±0.1	322.7±0.2	394.9±0.2
λ_2	349.2±0.2	366.9±0.1	419.5±0.2	829.3±0.2
λ_3	378.3±0.2	428.1±0.1	451.8±0.1	868.8±0.2
A	0.0014	0.0023	0.0024	0.014

4-chains P	300 K	400 K	500 K	600 K
λ_1	299.1±0.2	314.4±0.1	332.6±0.1	399.6±0.3
λ_2	329.0±0.1	408.7±0.2	432.4±0.2	799.2±0.1
λ_3	388.8±0.1	440.2±0.2	498.9±0.1	879.1±0.2
A	0.0014	0.0024	0.0034	0.013

4-chains R	300 K	400 K	500 K	600 K
λ_1	302.3±0.1	318.1±0.2	339.8±0.2	402.1±0.2
λ_2	362.8±0.2	413.5±0.3	509.7±0.2	844.4±0.3
λ_3	392.9±0.2	477.2±0.3	543.7±0.2	965.0±0.3
A	0.0014	0.0034	0.0050	0.016

6-chains P	300 K	400 K	500 K	600 K
λ_1	309.8±0.1	328.2±0.2	350.6±0.1	417.8±0.2
λ_2	402.7±0.2	525.1±0.1	560.9±0.1	960.9±0.2
λ_3	464.7±0.1	492.3±0.1	631.1±0.2	1044.5±0.2
A	0.0034	0.0050	0.0074	0.018

6-chains R	300 K	400 K	500 K	600 K
λ_1	314.8±0.2	331.3±0.2	357.1±0.1	426.5±0.2
λ_2	409.2±0.2	563.2±0.2	678.5±0.1	1023.6±0.2
λ_3	503.7±0.1	530.0±0.1	642.8±0.2	1151.5±0.2
A	0.0045	0.0064	0.0094	0.020

The changes in shape were quantified by calculating the degree of sphericity of the shape.

The degree of sphericity of the polydots is quantified by³⁸

$$A(a_1, a_2, a_3) = \frac{(a_1 - a_2)^2 + (a_1 - a_3)^2 + (a_2 - a_3)^2}{2(a_1 + a_2 + a_3)^2} \quad (7.1)$$

where λ_i are the 3 eigenvalues of moment of inertia tensor and $a_i = \sqrt{3\lambda_i}$. The sphericity parameter $A(a_1, a_2, a_3)$ is a number between zero for a spherical shape and 1 for a rod.³⁸

The 3 eigenvalues λ_i and $A(a_1, a_2, a_3)$ for different starting orientations and number of chains are presented in Table 7.1. The sphericity is presented in Figure 7.3(a) where a gradual divergence from sphericity is observed with increasing temperature with a discontinuity above 500K.

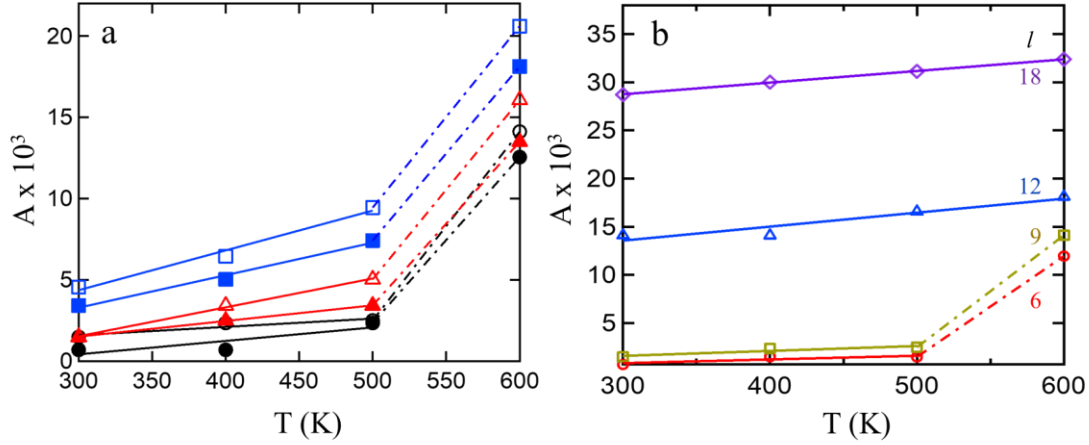


Figure 7.3: Sphericity parameter $A(a_1, a_2, a_3)$, of polydots as a function of temperature T (a) for polydots containing 2 (circles), 4 (triangles), and 6 (squares) chains for parallel (full) and random (open) initial state and (b) for 2-chain polydots with varying side chain length $l = 6, 9, 12$ and 18 .

Polydots of both random and parallel orientations show similar values for $A(a_1, a_2, a_3)$ for each value of N as a function of T . At 300 K, the sphericity $A(a_1, a_2, a_3)$ is ~ 0.001 for $N = 2$ system and increases only slightly to ~ 0.003 for $N = 6$. The sphericity for the 2-chain system is the same as that for a 1-chain polydot.¹⁹ $A(a_1, a_2, a_3)$ increases slowly with increasing temperature from 300 K to 500 K for all N . Above 500K, all systems become more aspherical as seen in Figure 7.3(a). This could be due to the thermal energy at 300 K is not enough to make the polymer chains move in order to affect the sphericity of the polydot however, as the temperature increases polymer chains within the polydot acquire enough thermal energy in return, they become more mobile and asphericity is increased. In addition, increasing number of chains expected to affect the entropy of the system and impacts the overall sphericity of the polydot as shown in Figure 7.3(a). We find that the

orientation of the polymers in the parent solution has no effects on either conformation, shape of stability, the number of chains confined.

To study the effect of side chain length on the stability of the polydots, 2-chain polydots were probed with increasing length of the side chains from $l = 6$ to 18. Visualization of the backbone of these polydots at 300 K, and 600K for $l = 9$, and 18 are shown in Figure 7.4.

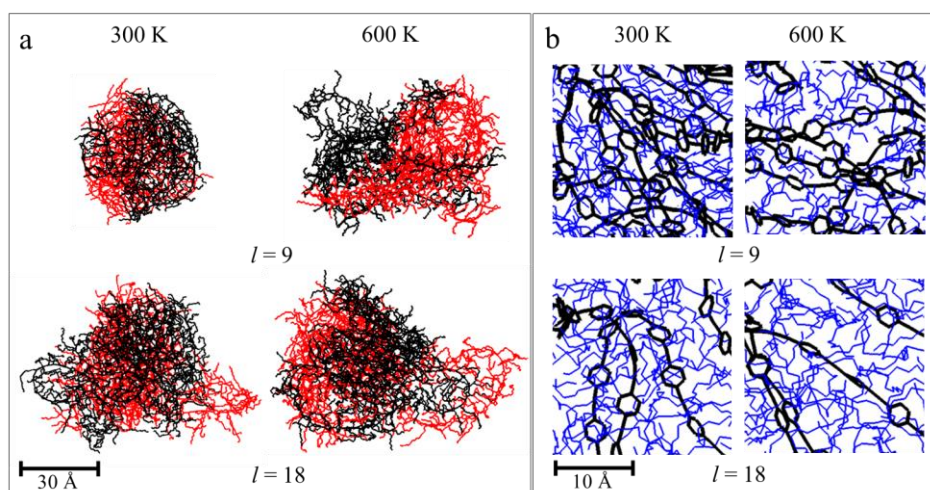


Figure 7.4: Visualization of backbones and side chains of 2-chain PPE polydots at 300 K, and 600 K for $l = 9$ and 18. (b) plots the corresponding zoomed images. For clarity, the polymer backbone and side chains are colored in black and blue, respectively.

At 300 K, the polydots with $l = 9$ are spherical and zoomed image shown that polymer backbones are tightly packed within the polydot, while those with $l = 18$ are aspherical. As seen in Figure 7.4, the polydots with $l = 9$ become aspherical at higher T . This observation is confirmed by the degree of sphericity and the values of $A(a_1, a_2, a_3)$ given in Table 7.2.

Table 7.2: Moment of inertia tensor eigenvalues ($\lambda_1, \lambda_2, \lambda_3$) and sphericity $A(a_1, a_2, a_3)$ for 2-chain polydots with $l = 6, 9, 12$ and 18 at indicated temperatures.

$l = 6$	300 K	400 K	500 K	600 K
λ_1	283.2±0.2	298.1±0.3	314.8±0.2	365.4±0.1
λ_2	311.5±0.1	327.9±0.2	377.8±0.2	694.3±0.1
λ_3	339.8±0.3	387.5±0.2	409.2±0.2	767.3±0.1
A	0.00069	0.0014	0.0014	0.011

$l = 9$	300 K	400 K	500 K	600 K
λ_1	291.0±0.1	305.8±0.1	322.7±0.2	394.9±0.2
λ_2	349.2±0.2	366.9±0.1	419.5±0.2	829.3±0.2
λ_3	378.3±0.2	428.1±0.1	451.8±0.1	868.8±0.2
A	0.0014	0.0023	0.0024	0.014

$l = 12$	300 K	400 K	500 K	600 K
λ_1	297.1±0.2	309.8±0.1	335.2±0.1	399.4±0.1
λ_2	623.9±0.1	650.5±0.2	737.4±0.2	918.6±0.1
λ_3	653.6±0.1	681.5±0.1	804.4±0.2	998.5±0.3
A	0.014	0.014	0.016	0.018

$l = 18$	300 K	400 K	500 K	600 K
λ_1	304.5±0.2	317.7±0.1	390.6±0.2	401.2±0.3
λ_2	791.7±0.1	857.7±0.2	1054.6±0.4	1123.3±0.2
λ_3	1035.3±0.2	1111.9±0.2	1406.1±0.3	1484.4±0.4
A	0.028	0.030	0.031	0.032

For the longer side chain lengths $l \geq 12$, $A(a_1, a_2, a_3)$ increases only slight as T increases as shown in Figure 7.3(b). At 300 K, the sphericity parameter indicated that polydots became more spherical as the length of side chains increased. Maskey et al.¹⁸ compared ethylhexyl-substituted PPE and bare PPE polydots and found that the side chains have a strong effect on the overall shape of the PPE polydots. The flexible side chains prevent the close packing of the polymer backbone within the polydot as the side chain length increases.

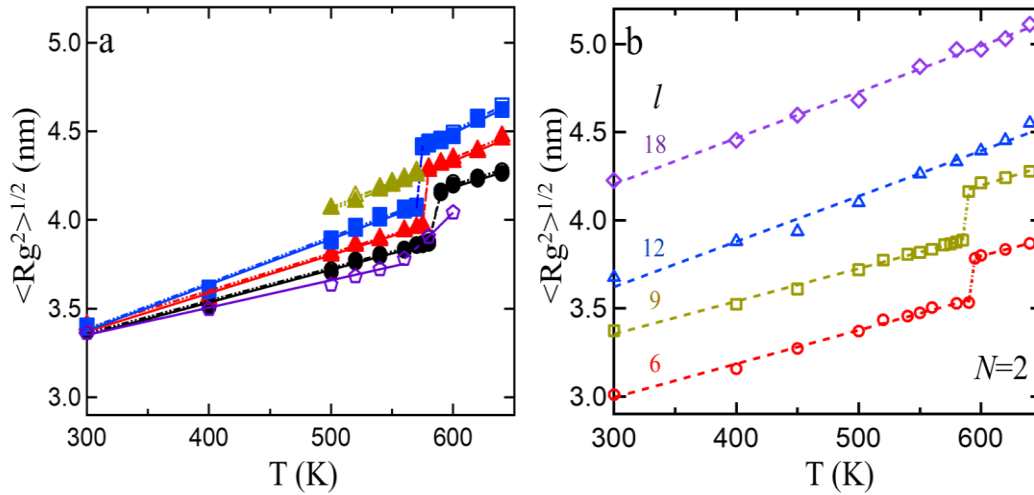


Figure 7.5: Root mean squared average radius of gyration $\langle R_g^2 \rangle^{1/2}$ of dinonyl PPE polydots as a function of temperature T (a) for polydots containing 1 (purple pentagons), 2 (black circles), 4 (red triangles), and 6 (blue squares) chains for parallel (filled) and random (open) initial state. Yellow triangle symbols represent the cooling curve of polydots containing 4 chains after jump temperature. (b) $\langle R_g^2 \rangle^{1/2}$ for 2-chain polydots with side chain length $l = 6, 9, 12$ and 18.

Average radius of gyration $\langle R_g^2 \rangle^{1/2}$ for dinonyl PPE polydots for different number of chains with same total molecular weight as a function of temperature shown in Figure 7.5(a). As seen from these results, the size of the polydot is independent of initial orientation of the chains. The 1- and 2-chain polydots have the same temperature dependence while for large number of chains the polydots increase faster with temperature with increasing number of chains. At high temperature there is a discontinuity in the size of the polydots, independent of the number of chains. This discontinuity occurs between 580 K and 590 K for $N = 1$ and 2, 575 K and 580 K for $N = 4$, and between 570 K and 575 K for $N=6$. This discontinuity in the size of the polydots could be attributed to glass transition. The differences in rate of increases of $\langle R_g^2 \rangle^{1/2}$ with T for different number of chains is largely due to the increase in the number of chain ends which are more mobile

than the internal chain segments. These polydots are not reversible at higher T as shown for the 4-chain polydot which was cooled from 580 K to 500 K, consistent with the fact that the low temperature polydots are kinetically trapped.

The effect of side chain length on the size of the polydots is shown in Figure 7.5(b) for 2-chain polydots for $6 \leq l \leq 18$ as a function of temperature. At 300 K, $\langle Rg^2 \rangle^{1/2}$ of polydots increase with increasing side chain length as expected. In all 4 cases, the size of the polydot increases linearly with increasing T . However, over the measured temperature range, only the polydots with shorter side chains have a discontinuous increase in $\langle Rg^2 \rangle^{1/2}$ at high T . The polydots with longer size chains are much less compact even at low temperature and simply swell as T increases, while those with shorter size chains are more compact and higher T are needed to release the kinetic constraints. These differences in the size and stability with length of the side chains could serve as a potential design tool for polydots with specific photo-physics.

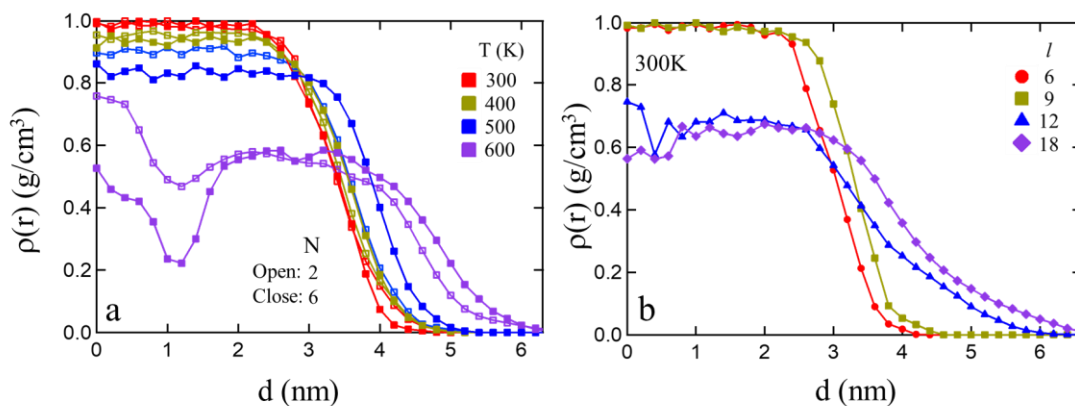


Figure 7.6: Radial mass density $\rho(r)$ as a function of distance d , from the center of mass of the polydot for (a) 2 (open symbols), and 6 (close symbols) chains for random starting orientation at 300 K (red), 400 K (yellow), 500 K (blue), 600 K (purple) and (b) $\rho(r)$ at 300K for 4 side chain lengths l .

To understand the internal packing of the polymer within the polydot, the radial density $\rho(r)$ from the center of mass of the polydot was measured. Results for $\rho(r)$ for 4 temperatures is presented in Figure 7.6(a) for 2-, 4- and 6-chain polydots. Polydots at 300 K to 500 K for all systems exhibits uniform densities away from the interface. However, at 600K, the interior density of the polydots is slightly reduced and $\rho(r)$ is non-uniform densities in all 3 cases. The radial density profile for polydots with different side chain lengths at 300K is shown in Figure 7.6(b). The radial density is uniform in all four cases, though the interior density of the polydots with short side chains ($l = 6$ and 9) is much higher than for polydots with longer side chains ($l = 12$ and 18). The longer side chain polydots also have a much broader interface compared to polydots with shorter side chains.

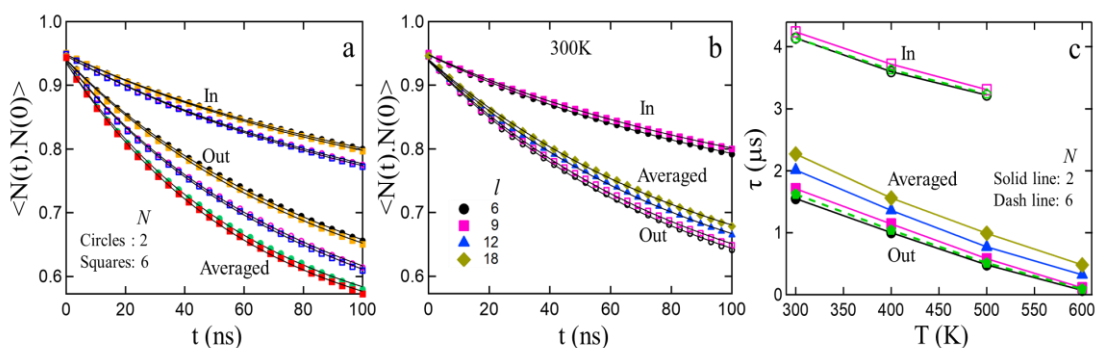


Figure 7.7: Autocorrelation function $\langle N(t) \cdot N(0) \rangle$, for aromatic rings in PPE backbone for internal aromatic rings (upper curves) and for aromatic rings at the interface (lower curves) for (a) $T = 300$ K (full) and 500 K (open) for random 2 (circles) and 6 (squares) chain polydots. Lower 2 curves with green and red symbols corresponding to an average over all aromatic rings at 600 K. (b) for $l = 6$ (full), and 9 (open) at 300 K. Two curves with blue and yellow symbols corresponding to an average over all aromatic rings for $l = 12$, and 18 respectively. The lines correspond to KWW fits. (b) Relaxation time τ as a function of temperature for internal aromatic rings (open) and for interfacial aromatic rings (full). The data at 600 K and $l = 12$, and 18 are average over all rings.

The structural changes of polydots at higher temperature are expected to affect the dynamics within the polydot. Therefore, probing the segmental dynamics is critical to control the photo-physics of the polydot.^{18,39} One measure of the local segmental dynamics is the autocorrelation function $\langle N(t) \cdot N(0) \rangle$, where $N(t)$ is normal to the plane of the aromatic rings which tethered to side chains is measured. Regardless of number of chains, side chain length or temperature, rings at the outer surface relax faster than inside rings as shown in Figure 7.7(a) and (b). The relaxation patterns do not fit with simple exponential but are well fit with the Kohlrausch-Williams-Watt (KWW),⁴⁰ $\langle N(t) \cdot N(0) \rangle = A \exp(-t/\tau)^\beta$ where A is pre-exponential factor, τ is the characteristic relaxation time and β is the stretched exponential. The best fit gives $\beta \sim 0.77$. Relaxation times τ for aromatic rings are in a range of μs for all the temperatures which is consistent with previous studies by Wijesinghe et al.^{19,20} and Maskey et al.¹⁸ As shown in Figure 7.8(c), the relaxation times τ decreases with increasing temperature for both inner and outer surface rings regardless of the number of chains confined. The relaxation times increase with decreasing number of chains which demonstrate the effect of multi chains on internal dynamics of the polydot. Increasing temperature results in decreasing the correlation times for the rings as expected due to thermal energy gained by the rings. Similar effects were observed for polydots with

different side chain lengths, however, as the side chain length increases, relaxation times τ for aromatic rings increases for respective systems. This indicates that the motion of the phenyl groups is hindered when associated with higher chain lengths. Above the transition temperature when the polydots become highly asymmetric in terms of polydot shape, the autocorrelation function is averaged over all aromatic rings. Results for τ at 600K are consistent with results for the outer rings at lower temperature.

7.5 Conclusions

This study has provided insight into effect of temperature on polydots with different numbers of chains and lengths of the side chain lengths. Independent of the number of chains and the length of the side chains, the polydots remain confined at all temperatures. At low temperature, the polydots are spherical, independent of the number of chains if the side chains are short. Increasing the length of the side chain results in aspherical polydots even at 300K. In all cases, the size of the polydots increase linearly with temperature until they reach a critical stability temperature, where the shape of the polydots discontinuously becomes aspherical. This transition could be attributed to the glass transition and not reversible as cooling the polydots from this high temperature state to low temperature results in the polydots remaining aspherical. This gives one of the first evidence that polydots can be tuned by introducing different lengths of side chains, and ultimately control the properties of the polydots.

The backbone of the PPE chains within the polydot is glassy, with relaxation times in a range of microseconds. Two types of dynamic regions are observed within the nano

confined system for internal and interfacial aromatic rings. Interfacial rings are much more dynamic compared to internal aromatic rings and number of chains confined effect on local dynamics of the polydot. This study further demonstrates that the conformation, stability, and dynamics of the polydots can be tuned by varying side chain length and number of confined chains. This understanding provides an insight into controlling properties of polydots and designing tools.

7.6 References

- (1) Zhang, Z.; Lu, Z.; Yuan, Q.; Zhang, C.; Tang, Y. ROS-Responsive and active targeted drug delivery based on conjugated polymer nanoparticles for synergistic chemo-/photodynamic therapy. *J. Mater. Chem. B* **2021**, *9*, 2240-2248.
- (2) Kovshova, T.; Osipova, N.; Alekseeva, A.; Malinovskaya, J.; Belov, A.; Budko, A.; Pavlova, G.; Maksimenko, O.; Nagpal, S.; Braner, S. Exploring the Interplay between Drug Release and Targeting of Lipid-Like Polymer Nanoparticles Loaded with Doxorubicin. *Molecules* **2021**, *26*, 831.
- (3) Liu, Y.; Yang, G.; Baby, T.; Chen, D.; Weitz, D. A.; Zhao, C. X. Stable polymer nanoparticles with exceptionally high drug loading by sequential nanoprecipitation. *Angewandte Chemie* **2020**, *132*, 4750-4758.
- (4) Liu, Y.; Yang, G.; Jin, S.; Zhang, R.; Chen, P.; Wang, L.; Chen, D.; Weitz, D. A.; Zhao, C. X. J-Aggregate-Based FRET Monitoring of Drug Release from Polymer Nanoparticles with High Drug Loading. *Angewandte Chemie International Edition* **2020**, *59*, 20065-20074.

- (5) Ashley, J.; Shukor, Y.; D'Aurelio, R.; Trinh, L.; Rodgers, T. L.; Temblay, J.; Pleasants, M.; Tohill, I. E. Synthesis of molecularly imprinted polymer nanoparticles for α -casein detection using surface plasmon resonance as a milk allergen sensor. *ACS Sens.* **2018**, *3*, 418-424.
- (6) Zhen, X.; Pu, K.; Jiang, X. Photoacoustic Imaging and Photothermal Therapy of Semiconducting Polymer Nanoparticles: Signal Amplification and Second Near-Infrared Construction. *Small* **2021**, *17*, 2004723.
- (7) Zhang, Q.; Li, D.; Zhong, J.; Wu, Y.; Shi, Y.; Yang, H.; Zhao, L.; Yang, K.; Lin, J. SPECT imaging and highly efficient therapy of rheumatoid arthritis based on hyperbranched semiconducting polymer nanoparticles. *Biomaterials Science* **2021**, *9*, 1845-1854.
- (8) Nagy-Simon, T.; Diaconu, O.; Focsan, M.; Vulpoi, A.; Botiz, I.; Craciun, A.-M. Pluronic stabilized conjugated polymer nanoparticles for NIR fluorescence imaging and dual phototherapy applications. *J. Mol. Struct.* **2021**, 130931.
- (9) Liu, S.; Ou, H.; Li, Y.; Zhang, H.; Liu, J.; Lu, X.; Kwok, R. T.; Lam, J. W.; Ding, D.; Tang, B. Z. Planar and twisted molecular structure leads to the high brightness of semiconducting polymer nanoparticles for NIR-IIa fluorescence imaging. *J. Am. Chem. Soc.* **2020**, *142*, 15146-15156.
- (10) Chen, J.; Qi, J.; Chen, C.; Chen, J.; Liu, L.; Gao, R.; Zhang, T.; Song, L.; Ding, D.; Zhang, P. Tocilizumab-Conjugated Polymer Nanoparticles for NIR-II Photoacoustic-Imaging-Guided Therapy of Rheumatoid Arthritis. *Adv.* **2020**, *32*, 2003399.

- (11) Yang, Y.; Fan, X.; Li, L.; Yang, Y.; Nuernisha, A.; Xue, D.; He, C.; Qian, J.; Hu, Q.; Chen, H. Semiconducting polymer nanoparticles as theranostic system for near-infrared-II fluorescence imaging and photothermal therapy under safe laser fluence. *Acs Nano* **2020**, *14*, 2509-2521.
- (12) Gao, D.; Hu, D.; Liu, X.; Zhang, X.; Yuan, Z.; Sheng, Z.; Zheng, H. Recent Advances in Conjugated Polymer Nanoparticles for NIR-II Imaging and Therapy. *ACS Appl. Polym. Mater.* **2020**, *2*, 4241-4257.
- (13) Mundra, M. K.; Ellison, C. J.; Behling, R. E.; Torkelson, J. M. Confinement, composition, and spin-coating effects on the glass transition and stress relaxation of thin films of polystyrene and styrene-containing random copolymers: Sensing by intrinsic fluorescence. *Polymer* **2006**, *47*, 7747-7759.
- (14) Ediger, M.; Forrest, J. Dynamics near free surfaces and the glass transition in thin polymer films: a view to the future. *Macromolecules* **2014**, *47*, 471-478.
- (15) Priestley, R. D.; Broadbelt, L. J.; Torkelson, J. M.; Fukao, K. Glass transition and α -relaxation dynamics of thin films of labeled polystyrene. *Phys. Rev. E* **2007**, *75*, 061806.
- (16) Ellison, C. J.; Torkelson, J. M. Sensing the glass transition in thin and ultrathin polymer films via fluorescence probes and labels. *J. Polym. Sci. B Polym. Phys.* **2002**, *40*, 2745-2758.
- (17) Ellison, C. J.; Torkelson, J. M. The distribution of glass-transition temperatures in nanoscopically confined glass formers. *Nature materials* **2003**, *2*, 695-700.
- (18) Maskey, S.; Osti, N. C.; Grest, G. S.; Perahia, D. Dynamics of polydots: Soft luminescent polymeric nanoparticles. *Macromolecules* **2016**, *49*, 2399-2407.

- (19) Wijesinghe, S.; Perahia, D.; Grest, G. S. Temperature response of soft ionizable polymer nanoparticles. *J. Chem. Phys.* **2018**, *149*, 084903.
- (20) Wijesinghe, S.; Maskey, S.; Perahia, D.; Grest, G. S. Luminescent tunable polydots: Charge effects in confined geometry. *J. Chem. Phys.* **2017**, *146*, 244907.
- (21) Jiang, Y.; McNeill, J. Light-harvesting and amplified energy transfer in conjugated polymer nanoparticles. *Chem. Rev.* **2017**, *117*, 838-859.
- (22) Wu, C.; Chiu, D. T. Highly fluorescent semiconducting polymer dots for biology and medicine. *Angewandte Chemie International Edition* **2013**, *52*, 3086-3109.
- (23) Wu, C.; Bull, B.; Szymanski, C.; Christensen, K.; McNeill, J. Multicolor conjugated polymer dots for biological fluorescence imaging. *ACS nano* **2008**, *2*, 2415-2423.
- (24) Tian, Z.; Yu, J.; Wu, C.; Szymanski, C.; McNeill, J. Amplified energy transfer in conjugated polymer nanoparticle tags and sensors. *Nanoscale* **2010**, *2*, 1999-2011.
- (25) Wu, C.; Szymanski, C.; Cain, Z.; McNeill, J. Conjugated polymer dots for multiphoton fluorescence imaging. *J. Am. Chem. Soc.* **2007**, *129*, 12904-12905.
- (26) Maskey, S.; Osti, N. C.; Perahia, D.; Grest, G. S. Internal correlations and stability of polydots, soft conjugated polymeric nanoparticles. *ACS Macro Lett.* **2013**, *2*, 700-704.
- (27) Steiger, D.; Smith, P.; Weder, C. Liquid crystalline, highly luminescent poly (2, 5-dialkoxy-p-phenyleneethynylene). *Macromol. Rapid Commun.* **1997**, *18*, 643-649.
- (28) Kloppenburg, L.; Jones, D.; Claridge, J. B.; Zur Loye, H.-C.; Bunz, U. F. Poly (p-phenyleneethynylene) s are thermotropic liquid crystalline. *Macromolecules* **1999**, *32*, 4460-4463.

- (29) Maskey, S.; Pierce, F.; Perahia, D.; Grest, G. S. Conformational study of a single molecule of poly para phenylene ethynyls in dilute solutions. *The Journal of chemical physics* **2011**, *134* (24), 244906.
- (30) Jorgensen, W. L.; Maxwell, D. S.; Tirado-Rives, J. Development and testing of the OPLS all-atom force field on conformational energetics and properties of organic liquids. *J. Am. Chem. Soc.* **1996**, *118*, 11225-11236.
- (31) Jorgensen, W. L.; Madura, J. D.; Swenson, C. J. Optimized intermolecular potential functions for liquid hydrocarbons. *J. Am. Chem. Soc.* **1984**, *106*, 6638-6646.
- (32) Plimpton, S. Fast parallel algorithms for short-range molecular dynamics. *J. Comput. Phys.* **1995**, *117*, 1-19.
- (33) Hockney, R.; Eastwood, J. *Computer Simulation Using Particles*. CRC Press. 1988.
- (34) Schneider, T.; Stoll, E. Molecular-dynamics study of a three-dimensional one-component model for distortive phase transitions. *Phys. Rev. B* **1978**, *17*, 1302.
- (35) Grest, G. S.; Kremer, K. Molecular dynamics simulation for polymers in the presence of a heat bath. *Phys. Rev. A* **1986**, *33*, 3628.
- (36) Stein, G. E.; Laws, T. S.; Verduzco, R. Tailoring the attraction of polymers toward surfaces. *Macromolecules* **2019**, *52* (13), 4787-4802.
- (37) Ginzburg, V. V. Modeling the Glass Transition of Free-Standing Polymer Thin Films Using the “SL-TS2” Mean-Field Approach. *Macromolecules* **2022**, *55* (3), 873-882.
- (38) Aryal, D.; Perahia, D.; Grest, G. S. Solvent controlled ion association in structured copolymers: Molecular dynamics simulations in dilute solutions. *The Journal of Chemical Physics* **2015**, *143* (12), 124905.

(39) Plazek, D. J.; Ngai, K. L. Correlation of polymer segmental chain dynamics with temperature-dependent time-scale shifts. *Macromolecules* **1991**, *24*, 1222-1224.

(40) Williams, G.; Watts, D. C. Non-symmetrical dielectric relaxation behaviour arising from a simple empirical decay function. *Transactions of the Faraday society* **1970**, *66*, 80-85.

CHAPTER EIGHT

SUMMARY

This research probed the structure and dynamics of ionomers in melts, and in solutions as well as polymer nanoparticles using molecular dynamics simulations (MD) and quasi-elastic neutron scattering techniques. The main goal of this work is to understand the impact confinement through ionic clustering and independently, via collapse into nanoparticles, on the structure and dynamics of the macromolecules. Further, atomistic and coarse-grained simulations were used to understand the rheological behavior of ionizable polymer melts.

1. Effects of ionic group distribution on the structure and dynamics of amorphous polymers melts

This study is focused on effects of distribution of ionizable groups along the polymer backbone on the structure and dynamics of ionomer melts using molecular dynamic simulations. We find that the distribution of sulfonated groups along the polymer chain backbone affects the shape, size, and packing of the ionizable groups within the cluster, and in turn affects the mesoscopic properties. Random polystyrene sulfonate melts consist of predominantly elongated clusters, whereas the clusters are more globular in precise polystyrene sulfonate melts. A mix of both elongated and globular clusters coexist in block melts. The cluster size distribution for all melts is relatively broad, with the block melts comprised of larger clusters compared to random and precise. Further, the internal

packing of the sulfonated groups within the ionic clusters as reflected in the pair correlation function is affected by the distribution of the ionic groups along the polymer backbone, such as controlling the cohesion of the clusters. These differences in the packing of the sulfonated groups within the ionic clusters appear to propagate to correlations in the nanometer dimensions reflected in $S(q)$. As expected for all melts, the polymer motion is constrained on multiple length scales. However, fast and slow dynamic processes are detected by $S(q,t)$ that are attributed directly to cluster-confined segments and those that reside further away. The local mobility of the block chains is higher than the random and precise, even though the ionic clusters are larger. It brings to light an intriguing insight regarding the dynamics of the polymers, where the number of unique chains associated with one cluster is directly correlated with the dynamics of the polymers. With fewer unique chains associated with a given cluster size for the block melts compared to other systems, results in faster dynamics. Finally, the Na^+ ions are condensed on the ionic groups as they move largely with ionic groups in all three systems, however, counter dynamics in the block melt is slightly higher than the random and precise melts.

2. Nonlinear elongation flows in associating polymer melts: from homogeneous to heterogeneous flow

In this study, we probed how associating groups alter the structure and dynamics of linear polymer melts in uniaxial elongation flows using molecular dynamics simulations. We study model polymers with randomly incorporated backbone associations with interaction strengths varying from 1-10 $k_B T$. We find that increasing the association

strength dramatically enhances both the extensional viscosity and strain hardening until systems eventually develop a yield-like overshoot and fail by cavitation. For intermediate interaction strengths $\sim 3 - 6 k_B T$ and low rates, systems flow with an additional dissipation due to the work of breaking associations. As rates increase, chains develop a bimodal, stretching dynamics due to the heterogeneous breakup of associating clusters that localizes elongation in a fraction of the chains. Elongated chains hinder cluster convection and rapidly pull out of larger clusters, which makes it easier for them to elongate further. In the limit of high strain rates, the viscous dissipation of all systems converges toward a common value independent of association strength α and strain rate. This appears to be due to the correlated dynamics of chain elongation and clusters fragmentation driving the cluster-size distribution $P(N_c)$ toward a system-independent distribution in strong flow.

3. Response of sulfonated polystyrene melts to nonlinear elongation flows

Here, we focused on the rheological behavior of polystyrene sulfonate in uniaxial elongation flows with sulfonation fractions varying from 0 to 0.55, encompassing both the ionomer and polyelectrolyte regimes. The sulfonated groups are randomly incorporated along the backbone of linear polystyrene polymer chains. After an initial elastic response, yielding and strain hardening is observed for all sulfonation fractions, indicative of solid-like behavior below the glass transition temperature. Strain-thinning is observed for polystyrene with a power law decay with strain rate with exponent $\beta = -0.6$, in agreement with experiments. As the sulfonation level increases the shear-thinning becomes stronger as β decreases.

4. Molecular insight into dynamics of sparse ionomer networks

The segmental dynamics of slightly sulfonated polystyrene networks formed in solutions using quasi elastic neutron scattering was studied. We find that sulfonated polystyrene chains below the entanglement length in cyclohexane with a very low fraction of ionizable groups, reduces the mobility of the polymer chains, at large length scales, but smaller than the length scale of the correlation between the ionic assemblies. In contrast, shorter segments remain dynamic, though their motion is affected by the presence of the ionic assemblies. We find that with some of the chains bridging between the ionic assemblies, very sparse network is formed affecting the motion of the polymer. Addition of ethanol enhances the dynamics on all the length scales captured in the QENS measurements. Ethanol affects the packing of the ionizable assemblies, introducing freedom by decreasing the chain constraints.

5. Multi-chain polymer nanoparticles: molecular dynamics simulation studies

This work provided an insight into the effects of temperature on polydots with different numbers of chains and lengths of the side chain lengths. Independent of the number of chains and the length of the side chains, the polydots remain confined at all temperatures. At low temperature, the polydots are spherical, independent of the number of chains if the side chains are short. Increasing the length of the side chain results in aspherical polydots even at 300K. In all cases, the size of the polydots increases linearly with temperature until they reach a critical stability temperature, where the shape of the

polydots discontinuously becomes aspherical. This transition is not reversible as cooling the polydots from this high temperature state to low temperature results in the polydots remaining aspherical. The backbone of the polymer chains within the polydot is glassy, with relaxation times in the range of microseconds. Two types of dynamic regions are observed within the nano confined system for internal and interfacial aromatic rings. Interfacial rings are much more dynamic compared to internal aromatic rings and number of chains confined effect on local dynamics of the polydot.

APPENDIX A



Copyright
Clearance
Center



RightsLink®

Home
Account Info
Help



APS
physics™

Title: Clustering effects in ionic polymers: Molecular dynamics simulations

Author: Anupriya Agrawal, Dvora Perahia, and Gary S. Grest

Publication: Physical Review E

Publisher: American Physical Society

Date: Aug 18, 2015

©2015 American Physical Society

Logged in as:
Dipak Aryal
Account #: 3001135508

LOGOUT

Review Order

Please review the order details and the associated [terms and conditions](#).

No royalties will be charged for this reuse request although you are required to obtain a license and comply with the license terms and conditions. To obtain the license, click the Accept button below.

Licensed Content Publisher	American Physical Society
Licensed Content Publication	Physical Review E
Licensed Content Title	Clustering effects in ionic polymers: Molecular dynamics simulations
Licensed Content Author	Anupriya Agrawal, Dvora Perahia, and Gary S. Grest
Licensed Content Date	Aug 18, 2015
Licensed Content Volume	92
Type of use	Thesis/Dissertation
Requestor type	Student
Format	Electronic
Portion	chart/graph/table/figure
Number of charts/graphs/tables/figures	1
Portion description	Figure 1
Rights for	Main product
Duration of use	Life of Current Edition
Creation of copies for the disabled	no
With minor editing privileges	no
For distribution to	Worldwide
In the following language(s)	Original language of publication
With incidental promotional use	no
Lifetime unit quantity of new product	0 to 499
The requesting person/organization	Dipak Aryal/ Clemson University
Order reference number	

Effects of Ionic Group Distribution on the Structure and Dynamics of Amorphous Polymer Melts



Author: Supun S. Mohottalalage, Dipak Aryal, Bryce A. Thurston, et al

Publication: Macromolecules

Publisher: American Chemical Society

Date: Jan 1, 2022

Copyright © 2022, American Chemical Society

PERMISSION/LICENSE IS GRANTED FOR YOUR ORDER AT NO CHARGE

This type of permission/license, instead of the standard Terms and Conditions, is sent to you because no fee is being charged for your order. Please note the following:

- Permission is granted for your request in both print and electronic formats, and translations.
- If figures and/or tables were requested, they may be adapted or used in part.
- Please print this page for your records and send a copy of it to your publisher/graduate school.
- Appropriate credit for the requested material should be given as follows: "Reprinted (adapted) with permission from {COMPLETE REFERENCE CITATION}. Copyright {YEAR} American Chemical Society." Insert appropriate information in place of the capitalized words.
- One-time permission is granted only for the use specified in your RightsLink request. No additional uses are granted (such as derivative works or other editions). For any uses, please submit a new request.

If credit is given to another source for the material you requested from RightsLink, permission must be obtained from that source.

BACK

CLOSE WINDOW

The copyright statement for American physical society (APS) journals (<https://journals.aps.org/copyrightFAQ.html>)
 As the author of an APS-published article, may I include my article or a portion of my article in my thesis or dissertation?

Yes, the author has the right to use the article or a portion of the article in a thesis or dissertation without requesting permission from APS, provided the bibliographic citation and the APS copyright credit line are given on the appropriate pages.